MARIA CURIE-SKŁODOWSKA UNIVERSITY IN LUBLIN
Faculty of Mathematics, Physics and Computer Science
Institute of Physics

DOCTORAL THESIS

Impurity band vs. valence band as the origin of itinerant holes in ferromagnetic (Ga,Mn)As

Pasmo domieszkowe a pasmo walencyjne jako źródło mobilnych dziur w ferromagnetycznym (Ga,Mn)As

Author: **ŁUKASZ GLUBA**

Supervisor: Dr hab. Jerzy Żuk, prof. MCSU
Adjunct Supervisor: Dr Oksana Yastrubchak

LUBLIN 2021

Abstract

(Ga,Mn)As, the dilute ferromagnetic semiconductor (DFS) has been a subject of excessive interest because of its controllable magnetic properties combined with the well known III-V semiconductor technology. Mn-doped GaAs became a prototype material for semiconductor spintronics. The Mn_{Ga} substitutional ions in GaAs act as acceptors and are a source of magnetic moments. Long-range ferromagnetic interactions mediate between the Mn^{2+} ions via the indirect interaction with the spin polarised holes. Nevertheless, there is an ongoing discussion whether the holes reside in the valence band or within the Mn impurity band, which also defines the dominating type of indirect magnetic interactions (double exchange or Ruderman-Kittel-Kasuya-Yosida/p-d Zener model). In this thesis, the band structure of (Ga,Mn)As epitaxial layers is studied by means of photoreflectance spectroscopy (PR) supported with the supplementary characterisation techniques: Raman spectroscopy, high-resolution X-ray diffraction (HR-XRD), superconducting quantum interference device (SQUID) magnetometry, spectroscopic ellipsometry (SE), and angle-resolved photoemission spectroscopy (ARPES). The results indicate the valence band source of holes in the ferromagnetic (Ga,Mn)As being consistent with the p-d Zener model of magnetism rather than the impurity band model.

Streszczenie

(Ga,Mn)As, rozcieńczony półprzewodnik ferromagnetyczny jest przedmiotem szerokiego zainteresowania z uwagi na jego sterowalne właściwości magnetyczne w połączeniu z dobrze znaną technologią półprzewodników z grupy III-V. GaAs domieszkowany Mn stał się prototypowym materiałem dla spintroniki półprzewodnikowej. Podstawieniowe jony Mn^{2+} w GaAs są domieszką akceptorową i źródłem momentów magnetycznych. Oddziaływania ferromagnetyczne dalekiego zasięgu pomiędzy jonami Mn^{2+} zachodzą poprzez pośrednie oddziaływanie z dziurami spolaryzowanymi spinowo. Niemniej jednak, toczy się dyskusja, czy dziury rezydują w paśmie walencyjnym czy w dodatkowym paśmie domieszkowym manganu, co również określa dominujący typ magnetycznych oddziaływań pośrednich (podwójna wymiana czy odziaływanie Ruderman-Kittel-Kasuya-Yosida/model p-d Zenera). W niniejszej pracy struktura pasmowa warstw epitaksjalnych (Ga,Mn)As jest badana za pomocą spektroskopii fotoodbicia (PR) wspomaganej dodatkowymi technikami charakteryzacyjnymi: spektroskopią ramanowską, wysokorozdzielczą dyfrakcją rentgenowską (HR-XRD), magnetometrią SQUID, elipsometrią spektroskopową (SE), oraz kątowo-rozdzielczą spektroskopią fotoelektronów (ARPES). Wyniki wskazują na pasmo walencyjne jako źródło dziur w ferromagnetycznym (Ga,Mn)As oraz są zgodne z modelem magnetyzmu p-d Zenera, a nie z modelem pasma domieszkowego Mn.

Acknowledgements

I would like to express my very great appreciation to Prof. Jerzy Żuk for his mentorship and valuable support. I am particularly grateful for the mentorship given by my adjunct supervisor Dr Oksana Yastrubchak, introducing me to the photoreflectance and Raman spectroscopy techniques, and engaging me in her project. I would like to offer my special thanks to Prof. Janusz Sadowski, for the great support in this project, growing (Ga,Mn)As layers, and support during the stays at the MAX-IV synchrotron facility. I wish to acknowledge the help provided by Prof. Tadeusz Wosiński for the mentorship and guidance. The X-ray diffraction measurements could not be possible without the vast expertise of Dr Jarosław Z. Domagała. I would like to extend my sincere thanks to Dr Tomasz Andrearczyk for the SQUID the measurements. I would also like to express my gratitude to Prof. Maciej Sawicki for the SQUID measurements and analysis, and more importantly, for taking over the mentorship at the end of the project. Special thanks are given to MSc Witold Rzodkiewicz for the spectroscopic ellipsometry measurements. Also many thanks for Prof. Grzegorz Sęk and Dr Wojciech Rudno-Rudziński for cooperation and support during my stay at the Wrocław University of Science and Technology. I appreciate very much the support in the ARPES measurements given by Dr Mats Leandersson and Dr Balasubramanian Thiagarajan at the MAX-IV facility. I am also grateful to Dr Mirosław Kulik for Rutherford Backscattering Spectrometry, Nuclear Reactions measurements and help with the spectroscopic ellipsometry method as well as to Dr Halina Krzyżanowska for introducing me to the analysis of Franz-Keldysh oscillations. I also had the great pleasure of working with the

colleagues from the Department of Ion Physics and Implantation: Dr Krzysztof Pyszniak, Dr Andrzej Droździel, DSc Marcin Turek, and MSc Janusz Filiks. I would like to acknowledge the effort made by Dr Michał Rawski connected with the TEM/SEM EDX measurements, and the support given by MSc Radosław Keller in the Raman microscopy measurements in the Analytical Laboratory of MCSU.

Last but not least, I am grateful to my wife, Monika, for every single piece of support during my prolonged research work.

The material presented in this thesis is based upon the research supported by the Foundation for Polish Science under Grant No. POMOST/2010-2/12 sponsored by the European Regional Development Fund, National Cohesion Strategy: Innovative Economy. The author expresses his gratitude for this support.

Contents

List of Abbreviations

ARPES	angle-resolved photoemission spectroscopy
CB	conduction band
CPLM	coupled plasmon- (longitudinal optical) phonon mode
DFS	dilute ferromagnetic semiconductor
DMFT	dynamical mean field theory
DMS	dilute magnetic semiconductor
FC	field-cooled
FKO	Franz-Keldysh oscillation
HH	heavy hole
HR-XRD	high resolution x-ray diffraction
KK	Kramers Kronig
LDA	local density approximation
LH	light hole
LO	longitudinal optical
LT	low temperature
LT-MBE	low-temperature molecular beam epitaxy
MBE	molecular beam epitaxy
MCD	magnetic circular dichroism
PR	photoreflectance
RHEED	reflection high energy electron diffraction
RT	room temperature
SE	spectroscopic ellipsometry
SIMS	secondary ion mass spectrometry

SQUID	superconducting quantum interference device
TDLS	third derivative line-shape
TEM	transmission electron microscopy
TO	transverse optical
TRM	thermoremnant magnetisation
VB	valence band
VBAC	valence band anticrossing
ZFC	zero-field cooled

List of Symbols

T_{C}	Curie temperature
T_{B}	blocking temperature
x	Mn concentration
m_{e}	electron mass
m_{opt}	optical hole mass
a_{rel}	relaxed lattice constant
c	perpendicular lattice constant
a_{sub}	substrate lattice constant
p	hole density
E_0	optical gap (complex Airy function)
E_G	optical gap (simplified method)
$\hbar\theta$	electro-optic energy

For my dearest Wife and

beloved Kids

Chapter 1

Introduction

1.1 Preface

Since introducing the first idea of the field-effect transistor by Julius Edgar Lilienfeld [1, 2], up to now, when the technology is pretty mature, semiconductors have revolutionised people's lives. After the improvement of a transistor in the 40s of the last century by the use of germanium and then in the 50s by applying silicon, the technology has been still developing for the next 50 years. Namely, miniaturisation led to doubling transistor amount on a chip every two years in agreement with Moore's Law formulated in 1965. This empirical law is also applied to the electronic memory capacity. The fast development pace of memories was possible due to the discovery of the giant magneto-resistance phenomenon published in 1988 [3]. This discovery was an entry point towards efficient control of electron spins in materials and is considered as the birth of spintronics. Miniaturisation results in the faster processors, larger capacities of disc drives, lower power consumption, and decreasing size of computers. However, this trend can not be infinite because of the physical limits of making smaller a silicon transistor or a single memory cell. Furthermore, the 5 nm technology node for transistors, which is considered as the boundary of Moore's law, is going to be supposedly fully released in 2020. Thus new technologies based on new materials and microarchitectures have to be developed.

Ideas based on spintronics can be potentially a remedy for common problems

of electronics. The reduction of electric power consumption and improved speed of devices can be obtained by exploiting the idea of spin logic. Development of this discipline would lead to creating a system that would take advantage of time gapless flow of information bits between memory and logic. One of possible approaches to achieve functional spin-logic devices that could be assimilated with spin-based memory, counts on connecting semiconducting and magnetic properties in one material. Such materials, called magnetic semiconductors (or dilute magnetic semiconductors - DMS), have been investigated since the '70s. Magnetic semiconductors can be prepared by doping conventional semiconductors with a small number of transition-metal atoms. Initially, the Mn-doped II-VI group semiconductors were investigated due to relatively high solubility limits of Mn [4]. Due to the isoelectronic character Mn^{2+} ions in such systems do not provide band carriers. Also it is not possible to introduce a large number of additional acceptor or donor atoms. Initially, the II-Mn-VI dilute semiconductors revealed only paramagnetic behaviour. Acceptor doping and carrier-density dependent transition to the ferromagnetic phase in DMSs have been accomplished in the heavily doped PbSnMnTe compound (IV-VI group) for the first time [5]. Later this effect was also observed in (Cd,Mn)Te (II-VI) with the ferromagnetic phase below 2 K [6]. Because of great technological importance of III-V group semiconductors, widely used in optoelectronics (lasers and detectors), communication devices (transistors operating at the microwave frequencies) and highly efficient solar cells, it was of significant importance to obtain III-Mn-V compound. However, due to very low solubility limits of Mn in the III-V semiconductors, it was a difficult task. It was overcome applying the epitaxial growth at a relatively low temperature to avoid the formation of precipitations like the ferromagnetic MnAs compound. Nevertheless, at the beginning the results were not impressive. The homogeneous n-type paramagnetic (In,Mn)As grown by the molecular beam epitaxy (MBE) was reported in 1989 [7] and the ferromagnetic p-type (In,Mn)As with $T_C = 7K$ in 1992 [8]. The

use of GaAs as a host for Mn^{2+} ions brought a significant increase in T_C up to 60 K [9]. At present, the maximum reported T_C for (Ga,Mn)As is 185 K for $x = 11\%$ [10]. It is an open question if it is possible to achieve T_C above room temperature (RT) in (Ga,Mn)As. The theory indicates the possibility of its achievement in Mn-doped GaN (and an oxide - ZnO) [11]. However, it is difficult to obtain it due to a limited achievable hole density.

Despite the demonstrated spintronic capabilities of materials with the coupled semiconducting and ferromagnetic properties [12], due to the obtained Curie temperatures below RT, the discussion shifted further from applications to fundamental aspects of magnetic interactions in a disordered system. Indeed, the mechanism of magnetic interactions in (Ga,Mn)As is not clear because of its complexity and despite numerous endeavours to describe this material. In particular, there is inconsistence over the character of holes in the carrier-mediated ferromagnetic interactions in (Ga,Mn)As. The fundamental question is whether they reside within the valence band or in the Mn-derived impurity band within the band gap. In fact, the band structure source of holes is an indicator of the nature of ferromagnetic interactions in (Ga,Mn)As.

Better insight into the nature of ferromagnetism in the prototypical DMS (Ga,Mn)As can bring new prospects for the increase in the Curie temperature in the magnetically doped semiconductors.

Thesis

(Ga,Mn)As as the topic of this thesis was an attractive at the time because of two reasons. Firstly, (Ga,Mn)As showed that magnetism can be controlled in the GaAs-based semiconductor devices. That unlocked a new potential in spin manipulation in electronics that could be widely applied. The relatively high Curie temperature obtained in the layers was promising to achieve the room temperature functionalities. Nevertheless, the primary motive to carry

on those studies were contradicting explanations and vigorous scientific discussion on the theoretical and experimental results related to the band structure of (Ga,Mn)As. The overview of the discussion on the magnetic interactions in (Ga,Mn)As is presented later in chapters 1.3 and 1.4. No consensus on the band structure character and the nature of ferromagnetic interactions in (Ga,Mn)As created a need for more studies. The central point upon this work is based on application of the photoreflectance spectroscopy method. This technique was supposed to help in drawing some conclusion on the band structure in (Ga,Mn)As by analysing the interband optical transitions energies. Despite modulation spectroscopy was earlier used for the low temperature grown GaAs and Ga(Bi,As) heterostructures it was rarely used for (Ga,Mn)As characterisation. As a matter of fact the optical transitions are one of the fundamental ways to characterise the band structure of semiconductor materials. Nevertheless, some standard methods like for example photoluminescence failed due to a large concentration of point defects introduced by the low temperature growth conditions. The measurements of the fundamental absorption edge are influenced by the defect and hole plasma related tailing effects. Magnetic circular dichroism experiment in the vicinity of the optical gap transition gives the broad features making the analysis difficult in (Ga,Mn)As. Also, over the time the technology of epitaxial growth improved and some relatively old results could be outdated. That suggested a potential knowledge gap that can be filled by the photoreflectance results.

This work contributes to the discussion by applying the photoreflectance (PR) spectroscopy method to study the interband optical transitions in the Mn-modified GaAs band structure. The analysis of the photoreflectance optical spectra is supported by several magnetic, structural and electronic characterisation methods. The thesis is organised as follows. Chapter 1 gives a fundamental introduction to the (Ga,Mn)As material and the summary of results concerning the band structure of (Ga,Mn)As. The main experimental techniques used to

characterise the (Ga,Mn)As layers are presented in Chapter 2. In Chapter 3, the experimental results are given, and the content is divided into four subsections related to the published items. Subsection 3.1 covers the band structure studies at the onset of ferromagnetic phase in (Ga,Mn)As. In subsection 3.2 the effects of annealing on the optical gap in (Ga,Mn)As are presented. Subsection 3.3 gives the insight into Bi co-doping on (Ga,Mn)As. The optical transitions occurring far from the centre of the Brillouin zone for the (Ga,Mn)As layers are analysed in subsection 3.4. Chapter 4 contains a discussion and conclusion.

The results included in Chapter 3 are published in the items listed below:

- L. Gluba, O. Yastrubchak, J. Z. Domagala, R. Jakiela, T. Andrearczyk, J. Żuk, T. Wosinski, J. Sadowski, and M. Sawicki, "Band structure evolution and the origin of magnetism in (Ga,Mn)As: from paramagnetic through superparamagnetic to ferromagnetic phase", Phys. Rev. B **97**, 115201 (2018)

- O. Yastrubchak, J. Sadowski, H. Krzyżanowska, L. Gluba, J. Żuk, J. Z. Domagala, T. Andrearczyk, and T. Wosinski, "Electronic- and band-structure evolution in low-doped (Ga,Mn)As", J. Appl. Phys. **114**, 053710 (2013)

- O. Yastrubchak, T. Wosinski, L. Gluba, T. Andrearczyk, J. Z. Domagala, J. Żuk, and J. Sadowski, "Effect of low-temperature annealing on the electronic- and band-structures of (Ga,Mn)As epitaxial layers", J. Appl. Phys. **115**, 012009 (2014)

- O. Yastrubchak, J. Sadowski, L. Gluba, J. Z. Domagala, M. Rawski, J. Żuk, M. Kulik, T. Andrearczyk, and T. Wosinski, "Ferromagnetism and the electronic band structure in (Ga,Mn)(Bi,As) epitaxial layers", Appl. Phys. Lett. **105**, 072402 (2014)

- L. Gluba, O. Yastrubchak, G. Sęk, W. Rudno-Rudziński, J. Sadowski, M. Kulik, W. Rzodkiewicz, M. Rawski, T. Andrearczyk, J. Misiewicz, T. Wosinski, and J. Żuk, "On the nature of the Mn-related states in the band structure of (Ga,Mn)As alloys via probing the E_1 and $E_1+\Delta_1$ optical transitions", Appl. Phys. Lett. **105**, 032408 (2014)

The statement of contribution for each subchapter in Results is included in Appendix A.

1.2 (Ga,Mn)As - dilute magnetic semiconductor

Gallium manganese arsenide, (Ga,Mn)As, is a prototypic DMS, also called ferromagnetic semiconductor (FMS). In this system, Mn atoms substitute Ga atoms in the zinc-blende structure of GaAs. Due to the electronic configuration of neutral Mn ([Ar] $3d^5 4s^2$) two electrons take part in the bonding with As [Ar] $3d^{10}4s^2 4p^3$) and Ga [Ar] $3d^{10}4s^2 4p^1$) resulting in the Mn^{2+} ion formation. Mn in such a configuration is a single acceptor and makes (Ga,Mn)As p-type. Therefore, Mn^{2+} with exposed d subshell gives a localised spin angular momentum equal to 5/2. Approximately 1% of Mn has to be provided to the GaAs matrix to obtain a ferromagnetic phase. Large distances between the localised Mn^{2+} moments in the ferromagnetic state are possible because the holes mediate magnetic exchange interactions resulting in a strong correlation between the Curie temperature and the holes density [18]. The highest T_C reported in (Ga,Mn)As is 180 K [19].

This material is grown with MBE at relatively low temperatures ($\leqslant 300$°C), so-called LT-MBE. Generally, the epitaxial growth of III-V based epitaxial structures is performed at about 600°C [21]. Then the migration of deposited atoms on the surface is the most effective in preventing from producing crystalline lattice defects. The obtained structures are characterized by a very high crystalline quality. The reason for growing (Ga,Mn)As by LT-MBE is the low

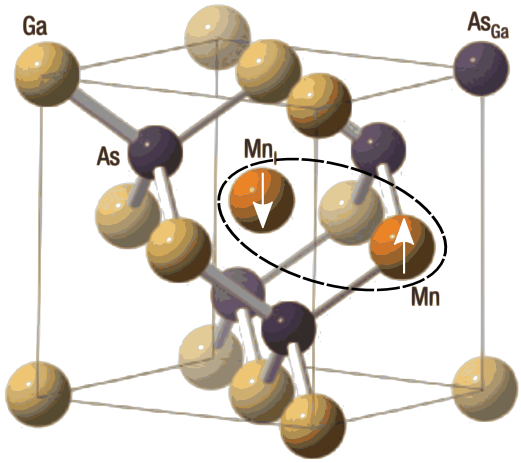

FIGURE 1.1: A unit cell of zinc-blende GaAs doped with manganese atoms at the substitutional site. The structure also contains common double-donor defects like arsenic anti-site, and interstitial Mn, Mn_I. The arrows in Mn_I and Mn_{sub} indicate the short-range antiferromagnetic spin-spin coupling. The picture adapted from Ref. [20].

solubility limit of Mn in GaAs under the equilibrium conditions. At higher temperatures, Mn atoms tend to segregate into metallic MnAs precipitates inhibiting obtention of a uniform (Ga,Mn)As structure instead of GaAs:MnAs compound. The low temperature non-equilibrium epitaxial growth conditions enable substitutional Mn atoms building into the GaAs matrix. However, this generates defects such as interstitial Mn (Mn_I), and arsenic anti-sites (As_{Ga}), (Fig. 1.1). These two defect types are double donors and therefore compensate holes [22, 23]. Mn_I [24] defects have a meta-stable (weakly bound) character and can out-diffuse due to the annealing treatment [25]. The annealing should be done below the growth temperature to prevent secondary phase separation of the ferromagnetic MnAs (more detailed information on the spinodal decomposition in DMS can be found in the review article [26]). Apart from the electronic compensation effects Mn_I can also suppress magnetic moment of the layer by the short-range interactions with Mn_{Ga} (Fig. 1.1). Namely, Mn_{sub} interacts antiferromagnetically with the nearby Mn_I defect and thus rules out the Mn^{2+}

ion spin from the long-range interactions [27]. Contrary to Mn_I, the As_{Ga} defects can be annealed at $\approx 500°C$ and they cannot be out-diffused by the LT annealing [28]. Some improvement has been made in the quality of the grown layers using the As cracker cell in MBE providing the As_2 dimer molecular beam instead of As_4 which allows to decrease the number of As_{Ga} defects [29]. They arise from the low-temperature growth and the nonstoichiometric As_2/Ga flux ratio, typically the As-rich region. However, the best quality samples can be obtained under the close-to-stoichiometric conditions by calibration of (Mn + Ga) vs As flux ratios and tailoring the substrate temperature to minimise As_{Ga} (and Mn_I) and maximise Mn_{Ga} concentration in order to perform the growth just below the MnAs segregation line as can be seen in Fig. 1.2.

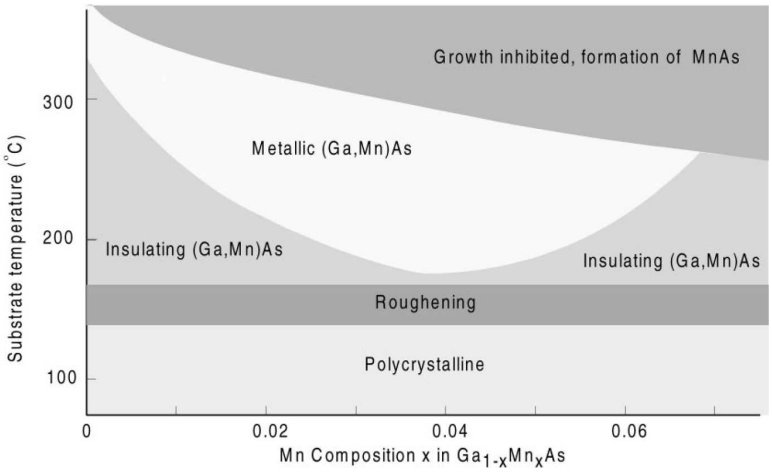

FIGURE 1.2: The schematic phase diagram showing the relation between the substrate temperature, Mn concentration and the electronic and structural properties of (Ga,Mn)As (after [30]).

These steps (together with the low temperature annealing treatment and etching) made it possible to grow the (Ga,Mn)As layer with $T_C = 180$ K for $x = 11\%$ [19]. Growing samples with higher T_C is difficult because the number of defects builds-up with x and therefore leads to compensation of Mn_{Ga}, which can be seen in Fig. 1.2 - despite a further increase in x the phase diagram steps into the insulating region.

The mentioned defects have also a significant efect on strain in (Ga,Mn)As leading to a tetragonal deformation of the cubic GaAs elemental cell by a compressive strain. The layers are grown pseudomorphically, and there is no strain relaxation mechanism. The strain can be regulated by application of buffer layers with a tailored lattice constant, for example (In,Ga)As or (Al,Ga)As.

1.3 Magnetism theories of (Ga,Mn)As

The explanation of magnetic interactions in (Ga,Mn)As has become the matter of controversy over the years. This issue remains unresolved due to the lack of consensus in the interpretation of experimental results, as well as calculations. However, there is no doubt that ferromagnetic interactions between the manganese ions in (Ga,Mn)As are mediated by the spin-polarised holes. This is confirmed by the correlation between T_C and the hole density for the samples with different Mn contents [31]. Because of the relatively large distances between the magnetic ions, that can build into the GaAs lattice, the magnetic interactions are mediated by the indirect exchange interactions, contrary to the direct exchange interactions between the localised spins of atoms with the overlapping orbitals in typical metallic ferromagnetic compounds like iron. Regarding (Ga,Mn)As two main pictures of magnetism, the mechanisms under the discussion attempt to explain its long-range ferromagnetic ordering. First, the mean-field approach to the Zener model assumes the occurrence of weakly bound carriers due to the Mn acceptor doping [11, 32]. The long-range ferromagnetic phase is a result of the p-d antiferromagnetic exchange interactions between the itinerant holes and the Mn^{2+} localised spins. Delocalisation or weak localisation of the carriers enables to involve a few localised spins by a single hole [33]. In this model, the real system with randomly distributed Mn^{2+} ions is reduced to an average periodic distribution by the virtual crystal approximation. The problem of the many-body exchange interactions between

the multiple Mn^{2+} moments is simplified considering a single localised spin interacting with the averaged effect from the surrounding Mn^{2+} moments in the system. The core of this model is 6×6 Kohn–Luttinger $k \cdot p$ matrix describing the valence band structure. It consists of matrix elements regarding the p-like valence band states. The spin-orbit interactions split the valence band into light (LH) and heavy holes (HH) subbands and the lack of inversion symmetry in the lattice introduces further spin-splitting of all the bands. Finally, the $k \cdot p$ hamiltonian, $\mathcal{H}_{k \cdot p}$, consists of four subbands at Γ_{8v} (spin-orbit split LH and HH bands) and two at Γ_{7v} (split SO band) of the wurtzite or zinc-blende semiconductors. In this formalism, the p-d exchange interactions between the d shells of Mn^{2+} ions and the valence p-orbitals are introduced by the p-d hamiltonian, $\mathcal{H}_{p-d}$. The biaxial strain hamiltonian (Bir-Pikus), $\mathcal{H}_{strain}$, enables modelling the influence of tensile or compressive strain in the layers [34]. The complete hamiltonian of the valence band in the p-type zinc-blende DMS can be written as follows [35]:

$$\mathcal{H} = \mathcal{H}_{k \cdot p} + \mathcal{H}_{p-d} + \mathcal{H}_{strain}, \tag{1.1}$$

The magnetisation vs magnetic field dependence, $M(H)$ can be expressed by the Brillouin function:

$$M = g\mu_b x_{eff} N_0 S B_S \left[\frac{g\mu_b H}{k_B (T + T_{AF})} \right], \tag{1.2}$$

where, g is the gyromagnetic coefficient ($g = 2$), μ_B is the Bohr's magneton, x_{eff} is the effective Mn content including compensation effects, N_0 is the number of magnetic ions per unit cell, S is the spin of the magnetic ion (5/2 for Mn^{2+}), B_S is the Brillouin function, k_B is the Boltzmann constant, and finally T_{AF} represents the contribution of antiferromagnetic short-range superexchange between the Mn^{2+} ions to the Curie temperature value. This model can also be

used to derive the expression for T_C, which reads [35]:

$$T_C = \frac{x_{eff} N_0 S(S+1)\beta^2 A_F \rho_{(S,T_C)}}{12 k_B} - T_{AF}, \tag{1.3}$$

where, β is the p-d exchange integral, A_F is the Fermi liquid-like parameter which accounts for the carrier-carrier interactions [6, 36, 37], $\rho_{(S,T_C)}$ is the total density of states at T_C that can be numerically derived for a given band structure and degeneracy of the hole gas. For high Mn doping levels, in the case of the metallic character of a layer, the p-d Zener model is equivalent to the long-range RKKY (Ruderman-Kittel-Kasuya-Yosida) carrier-mediated spin-spin interactions [36]. In this model due to the itinerant character of the carriers, the Fermi level is located below the top of the valence band. Its position is determined by the density of holes as pictured in Fi.g 1.3. This picture of ferromagnetism explains a number of effects occurring in (Ga,Mn)As, among others:

- Curie temperature [38, 39], its dependence on: hole density [40], gate voltage in the metal-insulator- semiconductor structures [41, 42], and hydrostatic pressure [43].
- Magnetocrystalline anisotropies - in/out of plane reorientation as a function of Mn concentration, hole density and temperature [44, 45].
- Magnetic domain structure [46, 47].

Because of contradicting results concerning band structure properties of (Ga,Mn)As the alternative explanation has been proposed [48, 49]. Although the p-d Zener model can explain magnetic properties of (Ga,Mn)As, the reports on impurity band pushed the scientific community to establish impurity band theory for the experimental results that cannot be explained in the frames of the band filling effect [50, 51]. The double exchange mechanism assumes ferromagnetic exchange interactions between the localised magnetic moments and the

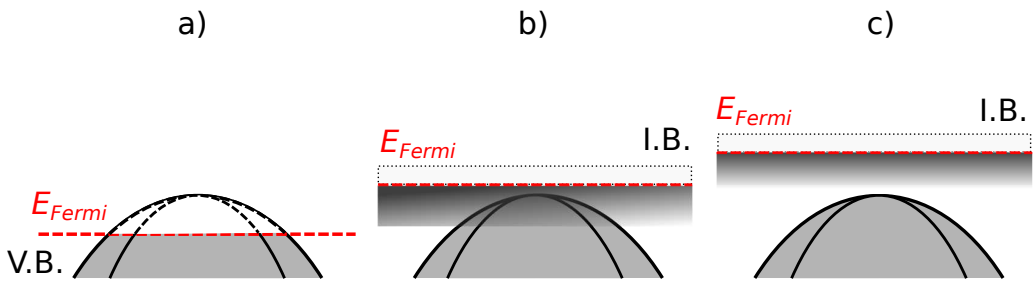

FIGURE 1.3: The graph illustrates the valence band (V.B.) in the p-type ferromagnetic (Ga,Mn)As for three cases: band filling effect a) and with Mn-derived impurity band b), and c), merged and detached impurity states.

bound holes. In this picture, the spin polarisation of holes occurs via hopping conduction of holes [52–57]. It is believed that if the Mn content is close to the critical Mott concentration, the Mn impurity band is formed, and the holes can hop between the d shells of manganese ions. This process can be illustrated as shown in Fig. 1.4. The transition of an electron with the antiparallel spin from Mn^{2+} to Mn^{3+} is prohibited by the Hundt's law. Therefore the double exchange mechanism is, by its nature, ferromagnetic. However, this approach can be used to explain magnetism in the samples of low hole densities [52]. It is referred to the importance of defect-related compensation effects because for the impurity band fully filled with holes, there is a smaller probability for the electron to hop between the overlapping Mn ion orbitals [52, 53]. On the other hand, it was proved that donor defects destroy ferromagnetism in (Ga,Mn)As and the low-temperature annealing treatment increases T_C by out-diffusion of Mn interstitials [18, 58]. For x higher than 1%, in the metallic samples the Mn states can merge with the valence band [59]. Some reports show that the impurity band can remain detached from the valence band even for the metallic ferromagnetic (Ga,Mn)As layers [60].

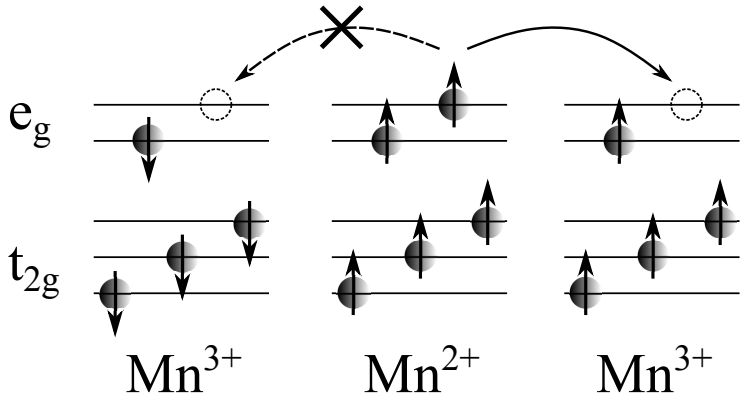

FIGURE 1.4: The double-exchange mechanism between Mn^{2+} and Mn^{3+} ions through hopping of spin polarised hole in the e_g orbital.

1.4 Battle of the bands

Having these two pictures of magnetism much attention was paid to study the band structure, and position of the Fermi level and then deduce the nature of the ferromagnetic phase in (Ga,Mn)As. Indeed, the experimental findings and their interpretation are often ambiguous.

The primary example of the puzzling results is given by the magnetic circular dichroism technique (MCD). This spectroscopic technique allows determining the nature and strength of interactions between the magnetic moments considering the sign and value of the p-d exchange integral $N_0\beta$, where N_0 is the number of Mn_{sub}. Obviously, MCD measurements have been employed to study the nature of magnetism in (Ga,Mn)As. The very first results revealed a positive MCD signal in the vicinity of the optical gap suggesting that the ferromagnetic p-d exchange interactions between the holes and localised spins are a dominant mechanism in the ferromagnetic (Ga,Mn)As layers [61, 62]. It was surprising as it was believed that indirect RKKY exchange, where the Mn ion and hole have opposite spins, is responsible for the ferromagnetic phase. Though the measurements revealed a positive sign of MCD signal near the Γ critical point, there were attempts to explain them based on the p-d Zener model [35, 62–64], namely, the carrier-related many-body interactions [35] or disorder effects [64]

causing a decrease in the band gap energy with the increasing carrier concentration or Mn doping. Nevertheless, the positive sign of the MCD signal in the ferromagnetic (Ga,Mn)As leads to the reconsideration of the nature of magnetism in (Ga,Mn)As assuming ferromagnetic exchange between the hole and the localised spin as the main mechanism which confirms the impurity band model. It was speculated that the broad positive MCD signal arises from optical transitions involving Mn impurity states and covering the negative MCD contributions from the E_0 and $E_0 + \Delta_0$ optical transitions, in the way shown in Fig. 1.5 [65, 66].

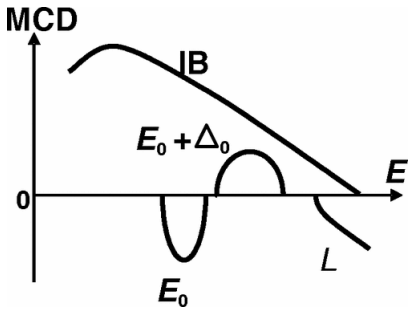

FIGURE 1.5: The picture shows the components of the MCD spectra explaining an anomalous positive MCD signal around the absorption edge of $Ga_{1-x}Mn_xAs$ by Ando et al.[65]. The negative E_0 peak, positive $E_0 + \Delta_0$ peak, and negative L signal are due to transitions between the valence band and the conduction band. The broad and positive MCD background signal is due to transitions to the impurity bands (IBs). Figure adapted from ref. [65].

Interestingly, Turek et al. [67] have shown that a positive MCD signal at the centre of the Brillouin zone may arise from the valence band model and the impurity band, as well. It was found comparing the MCD spectra related to band structures calculated using tight-binding hamiltonians with the parameters considering the presence or absence of the Mn impurity band [68, 69]. The MCD results have also been used to confirm the detached nature of the Mn impurity states. As opposed to Ando et al. [65, 70], Chakarvorty et al. [71, 72] and Berciu et al. [73] suggested that a positive MCD signal can arise from emergence of Mn related to the intermediate impurity band lying within the

band gap and detached from the valence band edge. More recently, Terada et al. [74] compared the experimental MCD spectra of (Ga,Mn)As layers with those calculated assuming an experimental imaginary part of the dielectric function of (Ga,Mn)As [75]. The broad feature in the MCD spectra considered earlier as a result of contribution from optical transitions involving Mn-related impurity states [65, 70] was explained by the thickness-dependent optical interference effect (in the case of reflection geometry). The Authors confirm existence of the intermediate Mn impurity band within the band gap due to the demonstrated good agreement between the calculated and experimental MCD spectra and the lack of the E_0 energy increase resulting from the Burstein-Moss shift due to the band filling effect.

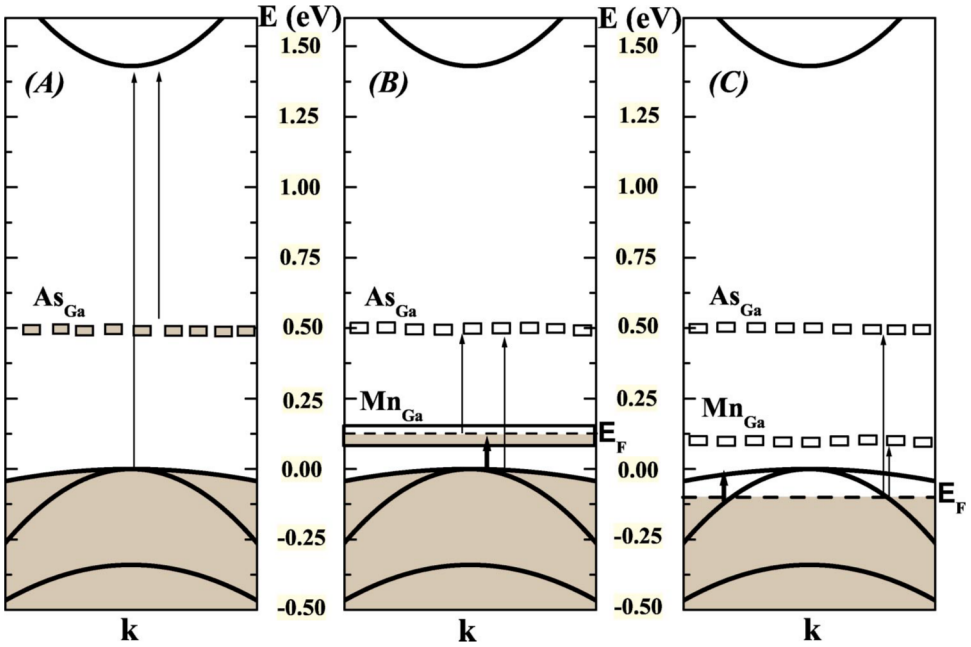

FIGURE 1.6: The picture showing band structure scenarios in the case of Mn-doped GaAs adapted from ref. [60]. Panel A shows the band structure of LT-GaAs with outlined As_{Ga} localised defect level. Panels B and C show two possible scenarios for the ferromagnetic (Ga,Mn)As corresponding to the Mn impurity band formation and the band filling effect, respectively.

The other technique revealing an impurity band in the band structure of (Ga,Mn)As is optical conductivity measured in the mid-infrared region to probe

valence intra-band transitions in Mn-doped GaAs [60, 76, 77]. Resonances occurring in this spectral region in the real part of conductivity function are interpreted as a valence band to impurity band transitions (Fig. 1.6 B) rather than intra-valence band transitions between the HH and LH subbands (Fig. 1.6 C). The mentioned resonance peak shifts to a lower energy with the increasing Mn content or due to the annealing treatment. As the Authors stated [60, 76, 77], this result is opposed to similar studies of mid-infrared feature carried out for the non-magnetic p-type GaAs [78] and calculations for the (Ga,Mn)As band structure considering the Fermi energy located within the valence band [79] but overlapping of the impurity band and valence band is not excluded. On the other hand, Jungwirth et al. [80] have shown that the red shift can be a consequence of impurity screening due to the increasing metallicity with the increasing Mn content. Dietl and Ohno [81] point out that analysis of the energy shift of the mid-infrared resonance with temperature or Mn content is not conclusive because there is no theory of optical conductivity taking into account the complex structure of (Ga,Mn)As valence band in the presence of spin-disorder scattering. Nevertheless, further studies on optical conductivity were carried out to observe Mn-induced modification in (Ga,Mn)As at the metal-insulator transition [82]. The results for (Ga,Mn)As were compared with the non-magnetic p-type GaAs:Be spectra for different Mn and Be contents. Metallic (Ga,Mn)As layers revealed spectral characteristics at the mid-infrared spectral range similar to GaAs:Be for the Be acceptor doping below the critical Mott concentration at which the Be electronic states form an impurity band that is not yet merged with the valence band. A similar conclusion was drawn based on optical conductivities measured using the (Ga,Mn)As and GaAs:Be field-effect devices [83]. The gate voltage was tuned for controlling carrier densities in depletion or accumulation layers. Electric-field induced changes in the hole densities modified the energies of Drude peak and the inter-valence band-related transitions in the optical conductivity spectra suggesting the impurity

band picture. Dietl and Śliwa [84] concluded that unusual transport and optical properties of (Ga,Mn)As observed using the mid-infrared spectral range and comparing to the non-magnetic degenerated semiconductors, may arise from the Anderson-Mott localisation rather than from the impurity band conduction character of holes.

Optical conductivity studies have also shown a relatively high optical mass of holes (reduced mass for intra-valence band transitions involving impurity band states) compared to the non-magnetic p-type GaAs [60, 76, 77]. Therefore, the Mn impurity band, with non-dispersive character, was inferred. The Authors point out that the valence band scenario in (Ga,Mn)As provides for $0.25m_e \leqslant m_{opt} \leqslant 0.29m_e$ [79] compared to measured $0.7m_e \leqslant m_{opt} \leqslant 1.4m_e$ for 5.2% and 7.3% ferromagnetic films [77] indicating that holes can not reside in the valence band. However, Chapler et al. [83] showed that optical masses in (Ga,Mn)As and GaAs:Be calculated from the optical conductivity spectra are in accord despite the different character of holes residence and the values drop below $0.42m_e$. Dietl and Ohno [81] identified this range as very close to those calculated by Sinova et al. [79] for the valence band model. From the analysis of thermoelectric and thermodynamic properties of (Ga,Mn)As based on the p-d Zener model Dietl and Śliwa [84] argued that (on) an increase in the effective mass values with the increasing hole density originates from the quantum localisation effects. Nevertheless, the increase in band effective masses due to Mn doping became an argument for the impurity band picture. The large effective mass of holes and their low mobilities in the ferromagnetic (Ga,Mn)As were addressed in the valence band anticrossing model (VBAC). It describes interactions of the Mn impurity band and the GaAs valence band as anticrossing-like [85, 86]. It predicts a decrease in the carrier mobility and an increase in effective masses of the carriers with the increasing Mn content. The anti-crossing theory was supported by studies of the optical gap using the PR technique [86]. However, this mechanism of interactions was questioned by Yastrubchak et al. [87].

The PR measurements of optical gap energy in (Ga,Mn)As with the increasing Mn content do not follow the valence band anti-crossing theory.

As the Fermi level should modify significantly the top of the valence band in the centre of the Brillouin zone of (Ga,Mn)As the optical gap energy was investigated. The primary optical absorption measurements on (Ga,Mn)As did not confirm the band filling effect expected for the p-d Zener model through observations of Burstein-Moss shift [62] (but instead it was inferred from splitting energies obtained in the magnetoabsorption experiment). Due to disorder, a conclusive result could not be obtained at the optical gap using spectroscopic ellipsometry (SE) [75]. Nevertheless, some results concerning the band gap energy were obtained with time-resolved differential reflectivity by de Boer et al. [88]. They reported blue shift of the absorption edge in the large x amount samples (10% and 12%) due to Mn doping which was explained as the competitive actions of tailing due to defects, band gap renormalisation, and band filling effect. Conversely, Yildrim et al. [89] reported the four-wave mixing spectroscopy on (Ga,Mn)As layers with x up to 10%. The resulting increase in intensity of low energy shoulder in the spectral feature of optical gap was recognised as an increase in density of states at the top of the valence band due to the additional Mn impurity states.

The valence band origin of holes was also questioned by the analysis of optical transition energies from a critical point far from the centre of the Brillouin zone where the Fermi level does not influence the transition energies. E_1 and $E_1 + \Delta_1$ - optical transitions along L direction ([111]) of the Brillouin zone were studied by SE. Burch et al. [75] showed that, as a result of Mn doping, the complex pseudodielectric function of (Ga,Mn)As revealed a broadened single feature assigned to the E_1 transition together with its blue shift with the increasing Mn content (Fig. 1.7 left panel). This energy shift was interpreted as a result of hybridisation between the valence band states and the Mn impurity band. It is worth mentioning that the magnitude of the shift is strengthened

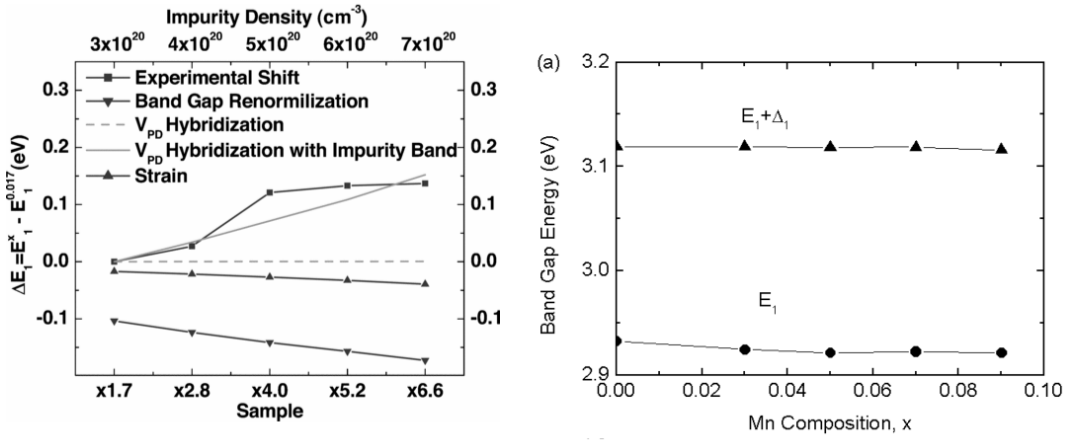

FIGURE 1.7: The left figure adapted from ref. [75] shows blue shift of E_1 optical transition energy with the increasing Mn content. Additionally, the possible effects are included: strain and band-gap renormalisation. The results are in agreement with the model of the valence band hybridised with the Mn impurity band. On the other hand, the figure on the right reproduced from ref. [90], shows no blue shift of E_1, as well as $E_1 + \Delta_1$, in (Ga,Mn)As in a wide range of x.

by the fact that considering the zinc blende of elemental cell of (Ga,Mn)As the Mn-As bonds lie in L-direction. Those conclusions were confirmed by the temperature-dependent ellipsometric studies of (Ga,Mn)As performed by Peiris et al. [91]. Nevertheless, almost simultaneously with Burch et al. [75] Kang et al. [90] reported the ellipsometric studies where the Authors proved a small red shift of well distinguishable E_1 and $E_1 + \Delta_1$ peaks for the similar Mn content range (Fig. 1.7 right panel). More recently Tanaka et al. [92] measured the MCD spectra of (Ga,Mn)As grown on InP for the samples up to 3% of Mn. The Authors measured E_1 and $E_1 + \Delta_1$ optical transitions and found a small red shift of those transitions with the increasing Mn content, being contrary to the results obtained by Burch et al. [75]. However, the impurity band model was inferred because of primary conclusions on the Zeeman splitting in the ferromagnetic layer. Interestingly, Prucnal et al. [93] showed no blue shift of the E_1 and $E_1 + \Delta_1$ optical transitions for the paramagnetic low Mn-doped samples (up to 0.6%, p-type) prepared by the Mn^+ ion implantation and millisecond annealing. The dielectric function spectra revealed an additional feature above

the energy of $E_1 + \Delta_1$ explained as interband excitation from the resonant Mn acceptor level.

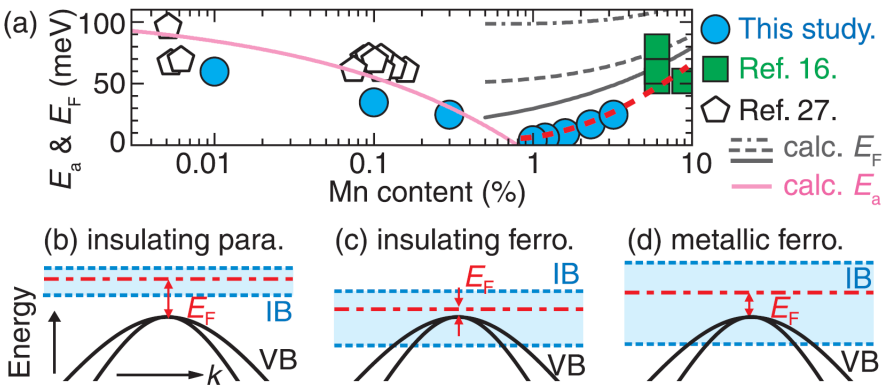

FIGURE 1.8: Fig. a) shows the Fermi level position as a function of x obtained by the resonant tunnelling spectroscopy (blue circles). (b)-(d) are the diagrams presenting (Ga,Mn)As valence band for three cases, depending on x value, as the interpretation of the results in (a). E_a is the Mn acceptor energy. The figure is reproduced from ref. [94].

The nature of the valence band states in (Ga,Mn)As was studied by resonant tunnelling spectroscopy. The studies of double barrier structures (Ga,Mn)As / AlAs / GaAs / AlAs / p-GaAs:Be proved that the Fermi level is approximately 100 meV above the GaAs valence band edge supported by the observation of the ground state subbands of the GaAs quantum well [95]. The anisotropy of the tunnelling magnetoresistance was explained quantitatively by means of the p-d Zener model suggesting valence band origin of holes in (Ga,Mn)As. On the other hand, Ohya et al. studied Au/(Ga,Mn)As/AlAs/p-GaAs:Be structures [96] and similar structure with (In,Ga,Mn)As [97] suggesting that the Fermi level lies in the band gap within the narrow and separated from the valence states Mn impurity band, even for the 10^{21}cm^{-3} hole density and high T_C samples. The measurements were performed for the ferromagnetic films with various thicknesses to control the separation of the quantised valence band subbands. However, the Mn impurity states near the Fermi level were not observed directly, but the existence of the impurity band was deduced from the occurrence of the

offset between the ground state HH1 resonance and the zero bias accounting for the Fermi level. A similar picture is provided in ref. [94] for the samples for which the Mn contents cover the range at the onset of ferromagnetism. The Authors reported anomalous Fermi level behaviour in (Ga,Mn)As for x ranging from 0.01% to 3.2%. As x increases up to 1%, the Fermi level lowers its position and becomes close to the valence band maximum. Nonetheless, the samples with $x \geqslant 1\%$ turn to the ferromagnetic phase and the Fermi level diverges from the valence band maximum as shown in Fig. 1.8. For $x = 3.2\%$ sample the offset between the valence band edge and the Fermi level was 25 meV. The onset of the ferromagnetic state in (Ga,Mn)As was also investigated by Muneta et al. [98]. The Authors proved that the resonances in the current-voltage characteristics assigned to the electronic valence levels in (Ga,Mn)As decrease their magnitude gradually with the increasing x only for the paramagnetic layers. A further increase in the Mn content causes paramagnetic-to-ferromagnetic phase transition and observation of restoration of the magnitude of the resonant tunnelling resonances. In the case of the paramagnetic region with the increasing x the Mn states form an impurity band becoming shallower due to screening of Mn impurities by the Coulomb potential, therefore they merge with the valence band and distort its original structure. For ferromagnetic phase the electronic states become restored because the Mn impurity band is detached and then do not interact with the quantised valence subbands. Nevertheless, recently the picture of merged impurity band and valence band has been proposed for interpretation of resonant tunnelling experiment [99]. Dietl and Sztenkiel [100] argue that the features in the current-voltage characteristics obtained in the experiments originate from quantized hole subbands of GaAs:Be ((In,Ga)As:Be) accumulation layer and the valence band subbands of (Ga,Mn)As ((In,Ga,Mn)As) are blurred due to disorder. They recall the paper by Mattena et al. [101] showing the absence of resonant tunnelling in the case of LT-GaAs quantum well. Furthermore, despite the tunnelling magnetoresistance-like behaviour Dietl and

Ohno [81] point out to the lack of the spin splitting of the quantised electronic states in current-voltage characteristics.

The electronic states of materials can be studied by photoemission spectroscopy experiments. In particular, the vicinity of the Fermi level was studied to reveal the nature of holes in (Ga,Mn)As. To this end, the angle-resolved (k-dependent) and integrated photoemission spectra were investigated. Okabayashi et al. [102] studied the resonance photoemission to investigate the Mn 3d electronic state energy in (Ga,Mn)As. It was shown that density of states at the Fermi level is very small and without clear Fermi edge, despite the metallic character of the samples. However, strong hybridisation of GaAs valence states and Mn states as well as dominant 3d-3d interactions due to a large partial density of states in the differential spectra (on-off resonance) were concluded. This paper points out that proper interpretation of (Ga,Mn)As photoemission spectra should take into account disorder and correlation effects.

No detached impurity band was demonstrated by Di Maco et al. [103] in the integrated photoemission spectra supported by the density of states calculations with LDA + DMFT taking into account the electron correlation effects. The studies of hard X-ray photoelectron spectroscopy in ref. [104] prove that the Mn states introduced to the valence band are centred 250 meV below the Fermi level revealing a small density of states at the Fermi energy extending GaAs states by approximately 50 meV upward. Therefore, impurity band conduction of holes is inferred due to the Fermi level localised within the tail of Mn-related extended states. A similar feature at the Fermi level is shown by Gray et al. [105]. Correspondingly to ref. [104], the angle-resolved data revealed additional Mn-related density of states centred 0.4 eV below the Fermi level and weakly overlapping the Fermi level. However, the coexistence of double-exchange and p-d exchange interactions responsible for the spin-spin coupling in (Ga,Mn)As was concluded.

Angle-resolved photoelectron spectroscopy (ARPES) giving k-dependent photoelectron energies revealed a weakly dispersive band related to the Mn states at approximately 0.4 eV below the Fermi level [102]. A similar feature was revealed in the ARPES measurements by Kobayashi et al. [106] identified earlier as a contribution from the Mn interstitial defects [108]. More recently, the angle-resolved measurements have been reported by Kanski et al. [107] for x at the onset of ferromagnetism (bottom of Fig. 1.9). The photoemission experiment revealed modification of density of states of GaAs due to Mn doping. Notably, the highly dispersive band was found. It reaches the Fermi level for 1% of Mn content giving a host for the delocalized holes for higher x. On the other hand, Souma et al. [109] found that the Fermi level lies 0.3 eV below the top of the valence band in the ferromagnetic (Ga,Mn)As with $T_C = 101$ K. Furthermore, the Authors identified depletion of the density of states near the Fermi level revealed in the photoemission spectra which was explained as correlation effects in the presence of disorder, as it was proposed by Richardella et al. [110] in their scanning tunnelling microscopy studies of (Ga,Mn)As films. Furthermore, those results are opposed to those from the ARPES measurements by Kobayashi et al. [106] where a weakly dispersive Mn-impurity band overlaps the top of the valence band states (top of Fig. 1.9).

The multi-dimensional discussion on the character of the valence band states in (Ga,Mn)As outlined above is not fully exhaustive. More information on the properties of (Ga,Mn)As and character of its valence band states in (Ga,Mn)As can be found in several review papers in refs. [12, 81, 111–113].

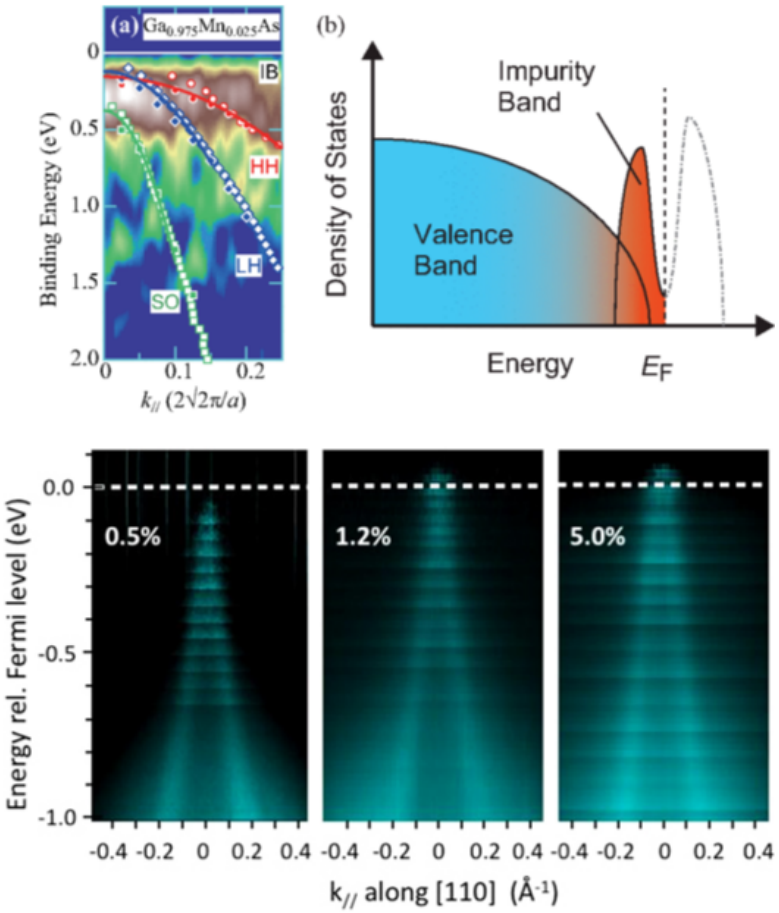

FIGURE 1.9: Two examples of the contradicting ARPES results. The topline figures (a) and (b) adopted from ref. [106] indicating Mn non-dispersive impurity band states merged with the valence band with the Fermi level above of the top of the valence band and within the impurity band. On the other hand, bottom line figure adopted from Kanski et al. [107] show the lack of similar impurity band states at the top of the valence band measured with *in-situ* ARPES for the paramagnetic (0.5%) and ferromagnetic (1.2% and 5%) layers.

Chapter 2

Experimental methods

2.1 Molecular beam epitaxy

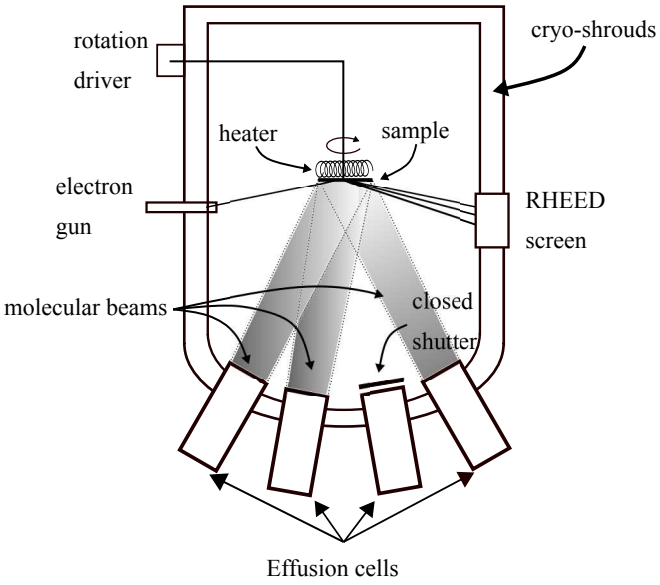

FIGURE 2.1: The schematic view of an MBE chamber. Molecular beams are emitted under the ultra-high vacuum by effusion cells containing pure elements. The beams are directed onto the crystalline sample substrate, which is heated and also rotated for homogeneous deposition. Reflection high energy electron diffraction (RHEED) is a standard tool for controlling deposition process.

MBE is a deposition method of crystalline materials. It is possible to grow layers of metals, semiconductors, insulators, or even organic films, which makes this technique one of the most functional. The studies on MBE started at the

end of the '60s [114]. IBM and Bell laboratories improved a method to grow semiconductor structures, like for example heterostructures, obtained earlier using Liquid Phase Epitaxy. The illustration of the typical MBE chamber is depicted in Fig. 2.1. The main chamber of the system contains ultra-high vacuum obtained by an ion pump, a sorption pump, a cryogenic pump cooled with liquid helium, and cryo-shrouds cooled with liquid nitrogen.

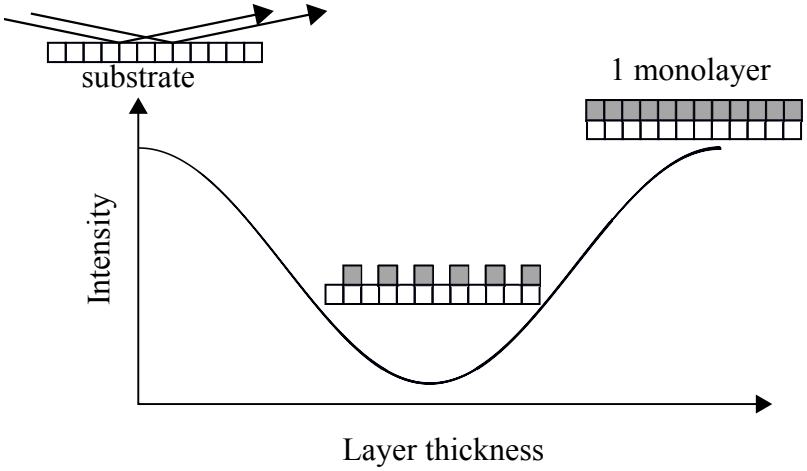

FIGURE 2.2: The reflection high energy electron diffraction intensity oscillation.

In this technique, molecular beams are usually produced by effusion (Knudsen or cracker) cells containing ultra-pure materials that are heated to a temperature enabling the material to evaporate. These beams of compounds flow through the vacuum onto a crystalline substrate surface where the molecules react, and the growth process proceeds. The lateral uniformity of the layers is kept by rotation of the wafer during the growth. The flux of the molecular beams is controlled by the cell temperatures and their shutters opening. The higher the temperature, the more material is deposited on the substrate surface. Some MBE reactors can support even ten ports for molecular beam sources containing different compounds. The mechanical shutters allow using some of them independently. The substrate in the MBE chamber is heated. The temperature has to be high enough to bring on the migration of the deposited molecules over the

surface and their occupation of lattice sites reproducing a substrate crystallographic structure. The temperature can be controlled by a thermocouple placed close to the substrate heater or a pyrometer. A slow rate of the growth (approximately one monolayer per second) allows ensuring two-dimensional deposition and precise control of the layer thickness. The monolayer thickness precision is controlled by the reflection high-energy electron diffraction (RHEED). RHEED is one of the most frequently applied techniques for the *in-situ* and real-time observation of the surface smoothness and crystalline quality of the grown layer during the epitaxial growth. In this technique, the several-keV electron beam is emitted by the gun and directed onto the sample at a glancing angle, as presented in Fig. 2.1. The beam is being reflected from the atomically structured surface and creates a diffraction pattern on the phosphorous RHEED screen and recorded by a CCD camera. The RHEED signal intensity changes during the growth. The maximum intensity is when the surface is atomically flat, and the electron beam is little scattered. On the other hand, the electron beam is scattered by atomic islands, which affect the intensity of RHEED pattern on the screen as it can be seen in Fig. 2.2. The samples were grown using the III-V MBE system located in the MAX-Lab, Lund, Sweden. This growth chamber is vacuum-connected with the I3 ARPES beamline of the synchrotron for the *in-situ* photoemission studies.

2.2 Photoreflectance spectroscopy

Modulation spectroscopy is one of the most precise types of methods for determining energies of optical transitions in the semiconductor structures [117]. It allows measuring sharp derivative-like spectral features related to the critical point energies, even at RT. The key issue that differs the modulation spectroscopy from other optical techniques like reflectance or transmission is that the sample is subjected to a factor influencing dielectric properties of a material

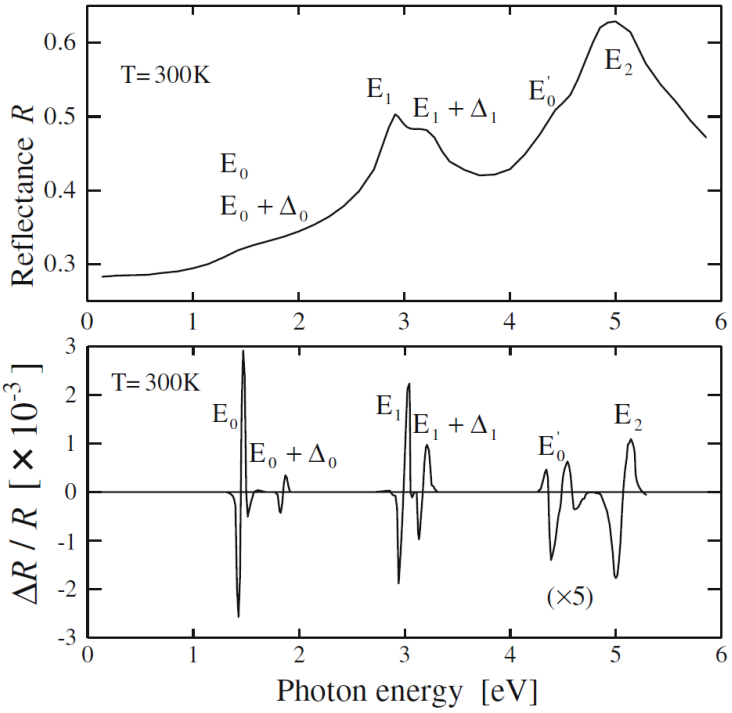

FIGURE 2.3: Comparison of the reflectance (upper) and electroreflectance (bottom) spectra of bulk GaAs measured at 300 K [115]. Some characteristic features in the spectra related to the critical point energies of GaAs band structure can be seen. The derivative-like character of modulated technique gives significantly more accurate results in comparison to the reflectance spectra [115].

which are related to its band structure. With the help of a lock-in amplifier, it is possible to detect a difference of optical responses between the unperturbed and perturbed spectra giving differential experimental results, similarly to that shown in the bottom part of Fig. 2.3.

The mentioned perturbation factor modulating the spectra can be introduced by pulses of heat (thermomodulation), strain (piezomodulation), or AC electric field (electromodulation). The photoreflectance (PR) technique (also called photomodulation spectroscopy or photomodulated reflectivity) is a contactless variation of electromodulated reflectance where the laser beam provides the electric field vector. Generally in this case, the modulation mechanism is a result of modification of built-in electric field inside a sample due to recurrent laser beam exposition on the sample with the photon energy higher than the

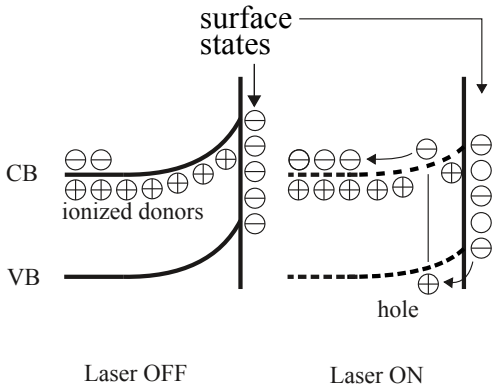

FIGURE 2.4: The subsurface built-in electric field modulation mechanism through excitation of electron from the valence band (VB) to the conduction band (CB) in PR for the n-type semiconductor.

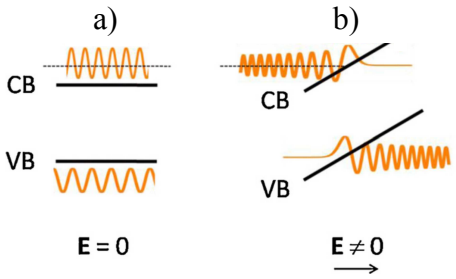

FIGURE 2.5: Band diagrams of semiconductor in the case of $E = 0$ (a) and $E \neq 0$ (b) [116]. For the case (a) electrons can be described by the Bloch wavefunctions. In the presence of electric fields the valence band (VB) and conduction bands (CB) become tilted and the wavefunctions of carriers show Airy function-like character rather than the Bloch function. It allows below band gap absorption and oscillatory character of the spectra above the energy gap.

band gap. It allows generating electron-hole pairs, which change the valence and conduction bands bending near the surface, as presented in Fig. 2.4, or near the heterostructure interface.

Basically, the measurement of PR spectra comes down to measure $\Delta R/R = (R_{ON} - R_{OFF})/R_{OFF}$ for different wavelengths (ON means: the reflectance with the laser illumination, and OFF without it). The changes of reflectivity can be expressed by those of a dielectric function:

$$\Delta R/R = \alpha(\epsilon_1, \epsilon_2)\Delta\epsilon_1 + \beta(\epsilon_1, \epsilon_2)\Delta\epsilon_2 \tag{2.1}$$

where α and β are the Seraphin coefficients dependent on the unperturbed dielectric function of the material. ϵ_1, ϵ_2 are the real and imaginary parts of the complex dielectric function, respectively. In the spectral region near the fundamental absorption edge, the β coefficient is close to 0 which simplifies expression 2.1. However, this assumption is valid only for bulk materials. In the PR technique, the laser illumination of material causes the acceleration of carriers, and it brakes periodicity of a crystal in the direction of the electric field. As a result, as it was propounded by Aspnes [118], the optical response would be third-derivative-like (in the case of thermo-modulation or piezo-modulation when the periodicity of a crystal is not broken and the response is first-derivative-like). The Aspnes's third-derivative line-shape (TDLS) equation reads as:

$$\Delta R/R = (\hbar\Omega)^3 Re(Ae^{i\phi}(\hbar\omega - E_{CP} - i\Gamma)^{-m}), \tag{2.2}$$

where A – the amplitude, ϕ – the phase of the Lorentzian line shape, E_{CP} – the critical point energy and Γ – the broadening. The value of m depends on the critical point dimension. For the three dimensional M_0 critical point of GaAs band gap it is 2.5. The electro-optic energy $\hbar\Omega$ can be expressed as:

$$\hbar\Omega = \left(\frac{q^2\hbar^2E^2}{8\mu}\right)^{1/3}, \tag{2.3}$$

where q is the elementary charge, E – the electric field, μ – the joint density of states effective mass in the direction of the applied electric field.

The above described above third derivative form of PR spectrum can be obtained in the so-called low field regime when the electro-optic energy $\hbar\Omega$ is much smaller than the broadening Γ. Another important case is the medium field regime, where $\hbar\Omega \geq \gamma$. Then, due to the electric field, the energy band diagram is tilted, as presented in Fig. 2.5 b.

As a result, the wave function of band carriers encounters a triangular potential barrier. The shape of the wave functions near the band edges becomes

Airy functions. Due to band tilting, the probability of excitation of valence band electron to the conduction band by a photon with energies smaller than band gap increases. In the PR spectra, it appears as above-band gap oscillatory feature (Franz-Keldysh oscillations - FKO) and below-band gap decay-type characteristics. Since $\beta(\epsilon_1, \epsilon_2)$ in equation 2.1 is very close to 0 near the energy gap, the change of real part of dielectric function can be expressed by:

$$\Delta\epsilon_1 = B\Omega^{0.5} Im\left(\frac{H(z)}{(E - i\gamma_0)^2}\right), \tag{2.4}$$

where $H(z)$ function is expressed by the Airy functions and it reads:

$$H(z) = \frac{1}{\pi} e^{-\frac{\pi i}{3}} \left[Ai'(z)Ai'(w) + wAi(z)Ai(w)\right] - \left(\frac{-\eta + (\eta^2 + \gamma^2)^{0.5}}{3}\right)^{0.5} + i\left(\frac{\eta + (\eta^2 + \gamma^2)^{0.5}}{3}\right)^{0.5}, \tag{2.5}$$

where $\gamma = \frac{\gamma_0}{\hbar\Omega}$, $z = \eta + i\gamma$ and $w = z\exp(-\frac{2\pi i}{3})$. $Ai(x)$ and $Ai'(x)$ denote the Airy function of the argument x and the first derivative of this function, respectively. To fit the PR spectra of (Ga,Mn)As I used two formulae 2.1 and 2.4 considering different contributions from the LH and HH subbands as it was done in Ref. [119] and Ref. [120]. In some cases the PR spectra revealed an additional below band gap feature related to the signal of heterostructure interface. For this purpose I used the Aspnes formula from equation 2.2. The fittings were done using the nonlinear model fitting package for Matlab. An alternative way to obtain the critical point energies from FKO is application of a simplified method. The approach presented below neglects the degeneration of the valence band [121]. This method is based on the analysis of the energetic positions of the extrema in the PR spectrum with FKOs. The energy of each extremum E_m of the oscillation versus the "effective index" F_m connected with the number of extrema can be expressed by the linear equation:

$$E_m = E_g + \hbar\Omega F_m \tag{2.6}$$

where $F_m = \left(\frac{3\pi(m-1/2)}{4}\right)^{2/3}$, m - the number of extrema, E_g - the critical point energy and $\hbar\Omega$ - the electrooptic energy. The value of the optical gap E_g can be found at the intersection of energy axis and the extrapolation of the linear fit of the E_m vs F_m dependence using equation 2.6.

The third method of critical points analysis of PR spectra is based on the Kramers-Kronig (KK) relations [122]. The Kramers- Kronig relation for the PR spectrum can be written as follows:

$$\Delta\rho_I(E_g) = \frac{2E_g}{\pi}\int_{E_a}^{E_b}\frac{\Delta R}{R}\frac{1}{E_g^2 + E^2}dE \tag{2.7}$$

where E_a and E_b are the boundaries of $\Delta R/R$ spectra and $\Delta R/R(E_a) = R/R(E_b) = 0$. Finally, the KK modulus can be calculated from the formula:

$$\Delta\rho = \sqrt{(\Delta R/R)^2 + (\Delta\rho_I)^2} \tag{2.8}$$

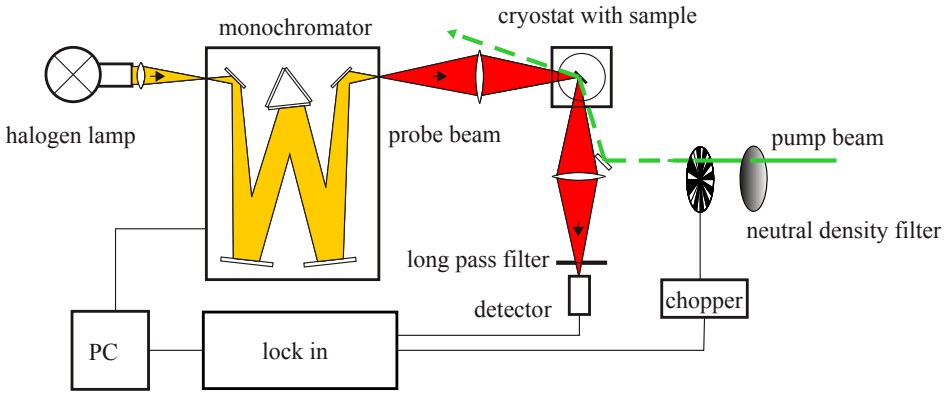

FIGURE 2.6: The schema of the photorefletance setup in the so called "dark" configuration where the broadband halogen lamp emits the probe beam to be limited to a narrow spectral line by the monochromator.

The PR set up assembled for the purpose of this thesis is shown in Fig. 2.6. The system is composed of pump and probe beams. The light beam of a tungsten halogen lamp is focused on the input slit of the 0.303 m Czerny-Turner type monochromator (Andor). At a certain wavelength the probe beam is focused and directed onto a sample at 45°angle related to its surface. The probe beam reflected from the sample beam is collected by a quartz lens and focused on the active region of a detector (Si or (In,Ga)As). In front of the detector, a long-pass filter is placed. Its cut-off wavelength is greater than a pumping laser wavelength to prevent from the scattered light collecting. The source of the pump beam is a laser. The pump and probe beams superimpose on a sample in this experiment. The intensity of the pump beam is controlled by the neutral density filter and chopped with a frequency of about 70 Hz. The signals from the detector and the chopper enter a Stanford Research SR830 lock-in amplifier and then transfer to a PC. The sample is placed in a helium close-cycled optical cryostat enabling measurement of the spectra in the temperature range from 10 K to 400 K. Besides, the so-called "bright" configuration was used. In this setup, white light as a probe beam is reflected from a sample and then collected by a monochromator coupled with a detector [123].

2.3 Raman scattering spectroscopy

As it was pointed out in the introductory chapter devoted to (Ga,Mn)As (1), the Curie temperature, T_C, of this material is very strongly correlated with the density of the holes because magnetic exchange between Mn^{2+} ions is indirectly mediated by the hole plasma. However, the exact determination of the hole concentration in this DMS is problematic. The measurements commonly applied for the non-magnetic semiconductors Hall effect are dominantly affected by the anomalous Hall effect[38, 124] proportional to the sample magnetisation. Therefore, the measurements have to be performed at very low temperatures

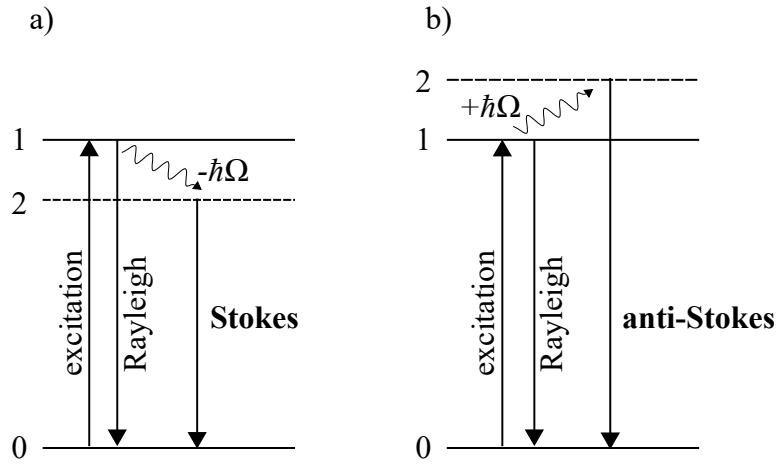

FIGURE 2.7: The schematic picture of Raman scattering mechanism involving the excitation from the initial state (0) to the virtual state (1) and Rayleigh emission. A small number of excitation photons can be scattered on phonons with the change of their energy by $\pm\hbar\Omega$. Stokes-like scattering (a) occurs with the absorption of the phonon energy by the crystal lattice. The anti-stokes process involves $\hbar\Omega$ energy transfer from the lattice.

and at very high magnetic fields when magnetisation is saturated. One of the alternative methods for the investigations of hole densities in III-V semiconductors is Raman scattering spectroscopy [125]. This simple fast and non-contact technique is based on excitation of the sample with a laser beam and measurement of the energy spectra of scattered light. The photons can be scattered without changing the energy in elastic or Rayleigh scattering. A small amount of light can interact with optical phonons engaging the energy shift of scattered photons. Stokes-like scattering involves absorption of the phonon energy (Fig. 2.7). Then, inelastically scattered light has lower energy than the incident excitation source. On the other hand, crystal lattice can lose the energy at the expense of an increase in the scattered photon energy, and one calls it anti-Stokes scattering. Raman scattering involves the interactions of light with the optical phonons and can be used to determine phonon mode spectral features in the centre of the Brillouin zone. Crystalline solids without the centre of inversion symmetry exhibit Raman-active longitudinal optical (LO) and transverse optical (TO) phonons. In the case of p-type doping, the carrier collective

modes (plasmons) interact with the longitudinal optical phonons creating the so-called coupled plasmon- LO phonon mode (CPLM). With the increasing hole concentration, the CPLM moves from the LO to TO phonon mode frequency. The Raman scattering cross-section of CPLM can be expressed as:

$$I = A(\omega) Im \left[-\frac{1}{\epsilon(\omega)} \right]. \tag{2.9}$$

The full formulation of $A(\omega)$ can be found in ref. [126] for electrons. However, it can be generalised to the case of multiple types of carriers existing in the p-type GaAs [125]. The dielectric function $\epsilon(\omega)$ is given by the sum of the phonon, the intraband and the interband contributions:

$$\epsilon = \epsilon_{\infty}(1 + \epsilon_{phonon} + \epsilon_{intra} + \epsilon_{inter}). \tag{2.10}$$

In particular, the phonon part of the dielectric function, ϵ_{phonon}, reads:

$$\epsilon_{phonon} = \frac{\omega_{LO}^2 - \omega_{TO}^2}{\omega_{TO}^2 - \omega^2 - i\omega\gamma} \tag{2.11}$$

where ω_{LO}, ω_{TO} and γ are the LO, TO frequencies and the phonon damping, respectively. Assuming small wavevector transfer due to the phonon excitation ϵ_{intra} can be expressed by the Drude term giving:

$$\epsilon_{intra} = -\frac{\epsilon_{\infty}\omega_p^2}{\omega(\omega + i\Gamma)} \tag{2.12}$$

with $\omega_p^2 = \frac{4\pi p e^2}{m_{\mu}^* \epsilon_{\infty}}$ and $\Gamma = \frac{e}{m_{\mu}^* \mu}$. In the case of equation 2.12 the intraband contribution of dielectric function to the Raman spectra takes into account valence band splitting into HH and LH subbands. It is reflected in the equation for the total plasmon frequency ω_p dependent on the total hole density p and the average valence band effective mass m^*. The total hole mobility μ, dependent effective mass m_{μ}^* in the formula for plasmon damping, Γ, can be assumed to

be equal to m^* expressed by the effective masses of heavy and light holes only. LO and TO phonon modes can be expressed by the Lorentzian line-shape.

CPLM in (Ga,Mn)As can be also investigated using the simplified method introduced by Seong et al. [127]. Generally, it is based on the analysis of relative intensities of unscreened LO (ULO) phonon mode and CPLM. The final formula for the hole density is given by:

$$p = \frac{8\varepsilon_0\varepsilon_s\alpha^2\phi_B}{e\left[\ln\left(1+\frac{\xi_A}{\xi_S}\right)\right]^2} \tag{2.13}$$

where ε_0 is the dielectric constant of vacuum, ε_S is the static dielectric constant, α is the absorption coefficient for the excitation energy for GaAs, ϕ_B is the surface potential barrier for GaAs, $\xi_A = A_L/A_P$ is the ratio of the integrated intensity of the ULO (A_L) and CPLM (A_P) in the Raman spectrum and $\xi_S = I_L/I_P$ are the relative Raman scattering efficiencies of the ULO (I_L) and CPLM (I_P).

All the presented results were obtained using an "inVia Reflex" Raman microscope (Renishaw) at RT with the 514.5 nm argon-ion laser line as an excitation source in backscattering geometry from (001) plane.

2.4 X-ray diffraction

High-resolution X-ray diffraction (HR-XRD) was used to determine structural parameters of most of the investigated (Ga,Mn)As epitaxial layers. This method enables characterisation of the crystallographic structure of a material and elemental cell dimensions. The value of interatomic distances can be used to obtain misfit strain, composition, thicknesses of the layers. It also enables quality assessment. It allows verification of initially assumed heterostructures parameters set before the epitaxial growth. The method is based on the elastic scattering of X-rays on the atoms. When X-rays interact with an atom (more precisely

its electrons), it becomes a source of a secondary electromagnetic wave within the Huygens's rule. The crystal lattice serves as periodically aligned secondary-sources causing interference of leaving X-rays. Constructive interference occurs when the Bragg condition is fulfilled for certain crystallographic directions labelled by the Miller indices (h, k, l).

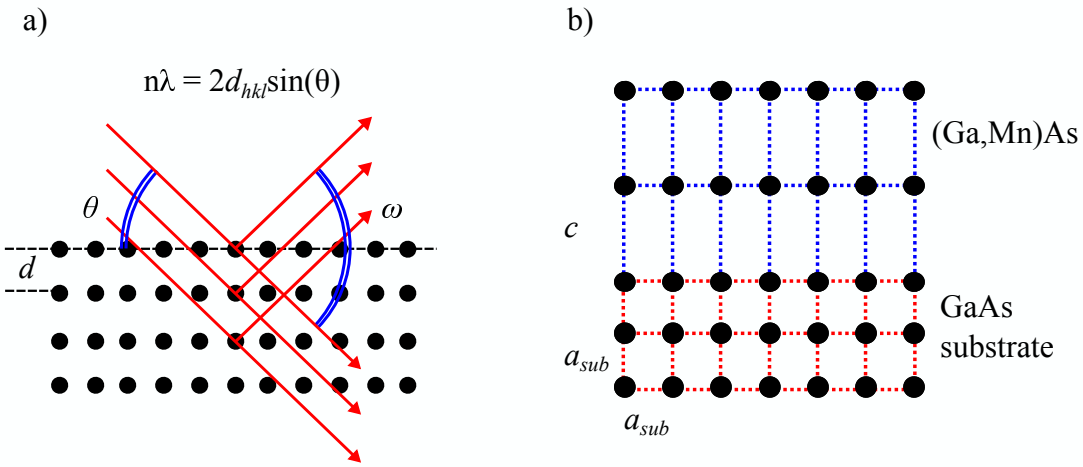

FIGURE 2.8: The reflection of X-rays from parallel crystallographic planes in the $\omega - 2\theta$ configuration a). Constructive interference occurs for θ angles satisfying the Bragg criterion. b) Due to Mn doping and pseudomorphic epitaxial growth of (Ga,Mn)As a cubic cell of GaAs becomes tetragonal with the perpendicular lattice parameter c and the parallel lattice constant a_{sub}

The (Ga,Mn)As/GaAs epitaxial heterostructures were investigated using coupled $2\theta - \omega$ scans for the symmetric (004) reflections to have an insight into vertical lattice parameters which are strongly dependent on the Mn content in (Ga,Mn)As grown on GaAs. Then, the perpendicular lattice constant of (Ga,Mn)As is usually assumed to be the same as for the GaAs substrate. This takes place because the layers are grown pseudomorpically on GaAs at a compressive strain, even for large Mn contents, due to the lack of strain relaxation mechanisms. The investigations of perpendicular lattice parameters are applicable in the case of (Ga,Mn)As grown on the buffer layer whose horizontal lattice constant differs from that of GaAs (e.g. (In,Ga)As, InP). The asymmetric (224) reflections are analysed by the reciprocal space mapping technique to

show relaxation of the lattice constant of the buffer along the epitaxial growth direction (to investigate lateral structural properties of a layer). This particular case is beyond the scope of this thesis. Angular positions of the peaks in 2θ scans arise from contribution of specific layers with different inter-atomic distances. Considering a layer/substrate structure, the perpendicular lattice parameter c of the strained layer can be calculated from the transformed Bragg criterion:

$$c = d_{(001)} = 4d_{(004)} = \frac{4\lambda}{2\sin(\theta_{layer})} \tag{2.14}$$

The lattice constant of the relaxed layer can be calculated considering its elasticity constants (C_{11}, C_{12}) from the Poisson ratio, ν:

$$a_{rel} = \frac{1-\nu}{1+\nu}(c - a_{sub}) + a_{sub}, \tag{2.15}$$

where $\nu = \frac{C_{12}}{C_{12}+C_{11}}$. Then, one can calculate the resulting out-of-plane strain using the $(c - a_{rel})/a_{rel}$ formula. The perpendicular lattice constant c can be used to obtain Mn content in the (Ga,Mn)As layer comparing the obtained value with the calibrated c vs Mn content plot [128]. This method usually works for more than 1% of Mn content. HR-XRD can be a tool for investigations of the layer thickness. It can be obtained from the analysis of angular positions interference fringes in the 2θ scan. They arise from different electron densities of the layers and depend on the interface quality. The measurements were conducted using the Philips X'Pert MPD Pro Alpha1 diffractometer with the copper anode as an X-ray source and $\lambda = 1.540598$ Å of Cu Kα_1 line. This diffractometer is equipped with a parabolic mirror, a four-bounce Ge (220) monochromator at the incident beam, and a three-bounce Ge analyser at the diffracted beam (triple-axis optics).

2.5 Superconducting quantum interference device

The superconducting quantum interference device (SQUID) was used to investigate magnetisation in the studied DMS layers. A sample is located in the centre of a superconducting magnet, the source of the homogeneous magnetic field. On the other hand, it is also put in the centre of detecting coils. A vertical movement of the magnetic sample through these coils induces electric current inside their wire. Detection coils are arranged into the so-called differential second-order gradiometer which enable to measure the signal from the sample suppressing that from the external homogeneous magnetic field (from the magnet, Earth's magnetic field). Then, the signal is delivered to a coil near the SQUID detector plunged into liquid helium. Generally, the SQUID detector is one of the most sensitive among known measurement devices. It is composed of two Josephson junctions closed in a loop. The electric current is conducted through this superconducting circuit. This configuration is susceptible to changes of magnetic flux running across the loop. Even a variation of a single quantum of magnetic flux can give a change in the voltage value measured on the loop. Thus, the SQUID detector acts as a magnetic flux-to-voltage transducer. Next, the SQUID voltage is processed by conventional electronics in order to amplify it and reduce noises.

Basic magnetic characterisation of (Ga,Mn)As with SQUID covers measurements of temperature-dependent magnetisation, $M(T)$ (Fig. 2.9 a)), and field-dependent magnetisation, $M(H)$ (Fig. 2.9 b)). As regards $M(T)$ curves, the layers can be characterised using zero-field cooling and field-cooling modes, including measurements of thermoremnant magnetisation (TRM) with the thermal cycling. This is done in order to study the Curie temperature for the ferromagnetic state and the nature of energy barriers of superspins regarding the superparamagnetic state. The typical $M(T)$ curve of ferromagnetic (Ga,Mn)As is shown in Fig. 2.9 a. As can be seen, spontaneous magnetisation decreases with

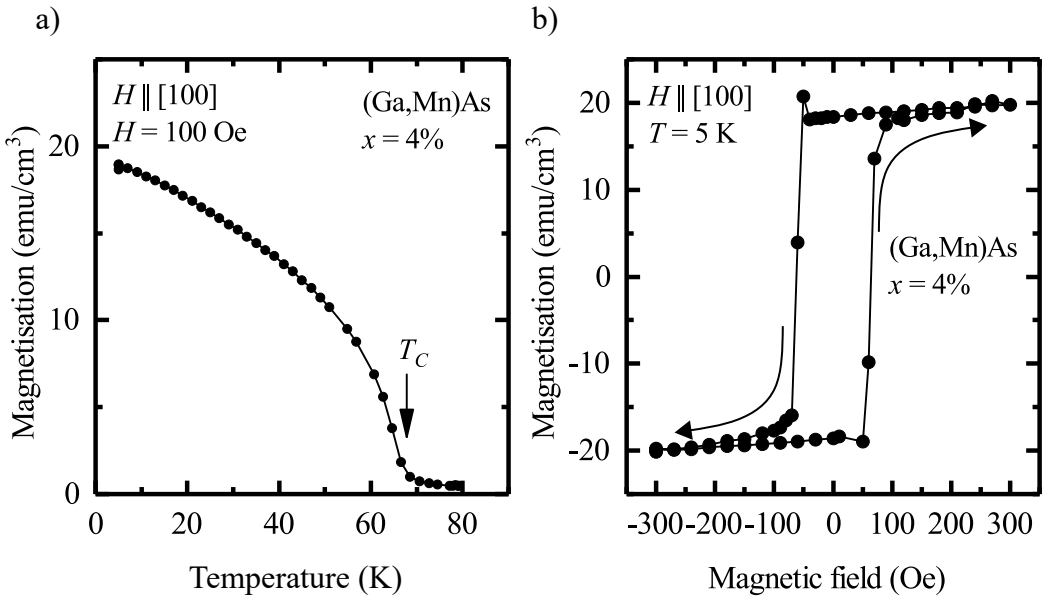

FIGURE 2.9: The exemplary $M(T)$ curve (a) and $M(H)$ (b) loop taken for the (Ga,Mn)As layer with 4% of Mn content. T_C of the layer is denoted by the arrow in part a). Measurements were made for the magnetic field H parallel to [100] crystallographic direction.

the increasing temperature toward the point, T_C denoted by the arrow, below which the layer loses its ferromagnetic properties. The exemplary $M(H)$ loop of a ferromagnetic layer is shown in Fig. 2.9 b. It is obtained after subtraction of diamagnetic contribution of GaAs substrate. The high-field measurements allow to assess saturation magnetisation of a layer and then concentration of magnetically active Mn^{2+} ions.

2.6 Spectroscopic ellipsometry

Spectroscopic ellipsometry is an optical characterisation technique for investigation of the spectral dependence of optical constants (n, k) of a wide range of compounds and structures. Optical constants of a material can be modelled in order to resolve parameters of the structures like for example thickness, composition, disorder, surface or interface roughness. It can be also used for the studies of optical transitions. Spectroscopic ellipsometry consists in detection

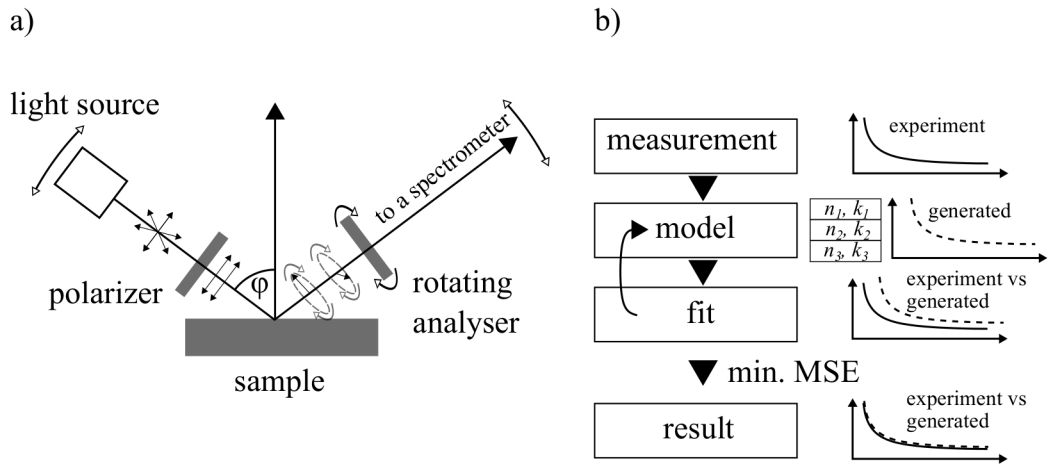

FIGURE 2.10: Technical scheme of rotating analyser ellipsometer a). Figure b) shows the path of modelling the experimental data.

of the polarisation state change of electromagnetic wave due to the interactions with the investigated media. One of the most common ellipsometric setups is equipped with the rotating analyser. The broadband source generates the incident beam, which is passed through a linear polariser. After the reflection from the sample, the polarisation changes can be tracked down with the help of a rotating analyser set prior to the use of a monochromator coupled with a detector. Measurements can be done at multiple angles of incidence (ϕ). The polarisation state of reflected light can be described by the ellipsometric angles Ψ and Δ. Ψ is related to the relative reflectance coefficients at p- (R_p) and s- (R_s) polarisations, and Δ corresponds to the phase shift between the p- and s- polarised waves, $\Delta = \delta_p - \delta_s$. The equation connecting the reflectance coefficients with Ψ and Δ is defined by:

$$\rho = \frac{R_p}{R_s} = \tan\Psi \exp(i\Delta) \tag{2.16}$$

Then the ellipsometric angles are connected with the optical constants or the complex dielectric function by R_p and R_s that are expressed by the Fresnel equations [129].

The ellipsometry method is "model-based". The measured spectral dependences of Ψ and Δ are compared with a structure model generated by the software. Free parameters set in the model are then fitted with some non-linear regression methods in order to minimise the mean square error between the modelled and measured spectra. For investigations of (Ga,Mn)As layers the Variable Angle Spectroscopic Ellipsometer (VASE) with rotating analyser by J.A. Woollam Co. was used. The setup allows performing measurements at RT. The calculations are usually done using the software dedicated to the ellipsometer, WVASE32 [130].

Chapter 3

Results

3.1 The onset of ferromagnetism in (Ga,Mn)As

3.1.1 Room temperature photoreflectance studies

Among the problems of explaining ferromagnetic spin-spin coupling in (Ga,Mn)As, the prominent role in the discussion was played by the onset of ferromagnetic phase in (Ga,Mn)As with the increasing Mn content x. As it was pointed out in Chapter 1, the result of valence band modification by Mn acceptor states is under a broad discussion, and different models were proposed. Alberi et al. [86] developed the VBAC model (p. 17). For low enough x, before the Mn-related impurity band can merge with the valence band edge due to broadening, the anticrossing phenomena occur, leading to an increase in energy of the optical gap transition. The studies on the infrared optical conductivity by Chapler et al. [82, 83] and Singley et al. [60, 76] also lead to a conclusion that for the low enough x the detached Mn-related impurity band exists within the energy gap. Contrary to those findings, the merged picture of the Mn states and valence band at the onset of ferromagnetism was proposed by Muneta et al. [94]. However, a very different picture was provided by Kanski et al. [107] where the ARPES spectrum of the top of the valence band of GaAs is modified by much lower doping level allowing to establish the ferromagnetic phase in (Ga,Mn)As.

In this chapter, I present the room and LT-PR studies of (Ga,Mn)As aimed

TABLE 3.1: The layer thicknesses, lattice parameters (c and a_{rel}), lattice mismatch ($(a_{rel} - a_{sub})/a_{sub}$, where $a_{sub} = 5.65349$ Å is the lattice constant of GaAs substrate), and vertical strain ($(c - a_{rel})/a_{rel}$) calculated from the results of HR-XRD measurements performed at room temperature.

x (%)	Thickness (nm)	c (Å)	a_{rel} (Å)	Lattice mismatch ($\times 10^4$)	Vertical strain ($\times 10^4$)
0	800	5.65527	5.65436	1.5	1.6
0.001	900	5.65536	5.6544	1.6	1.7
0.005	800	5.65546	5.65445	1.7	1.8
0.8	300	5.65959	5.65646	5.3	5.5
1.2	230	5.66509	5.65914	10	10.5

at resolving the mechanism of the valence band modification by the Mn acceptor doping at the onset of ferromagnetism.

Structural, electronic, and magnetic properties

Four (Ga,Mn)As layers with the Mn contents of 0.001 %, 0.005 %, 0.8 %, and 1.2 % and the thicknesses between 230-900 nm were investigated. The layers were grown epitaxially using the LT-MBE method at a temperature of 230°C on the semi-insulating (001)-oriented GaAs substrates. As a reference, there was used an 800-nm-thick undoped GaAs layer grown on GaAs under the same conditions as the (Ga,Mn)As layers. The layer thicknesses and Mn content, which are listed in Tab. 3.1, were verified during the growth by monitoring the RHEED intensity oscillations. The HR-XRD measurements revealed that all the layers are grown at a compressive misfit stress, and were fully strained to the GaAs substrate. The results exhibited a clear X-ray interference fringes for the (004) Bragg reflections evidencing a high structural perfection of the layers, as shown in Fig. 3.1.

The layer thicknesses derived from the angular spacing of the fringes correspond very well to the thicknesses specified by the growth parameters. The LT-GaAs and (Ga,Mn)As diffraction peaks in Fig. 3.1 shift to smaller angles

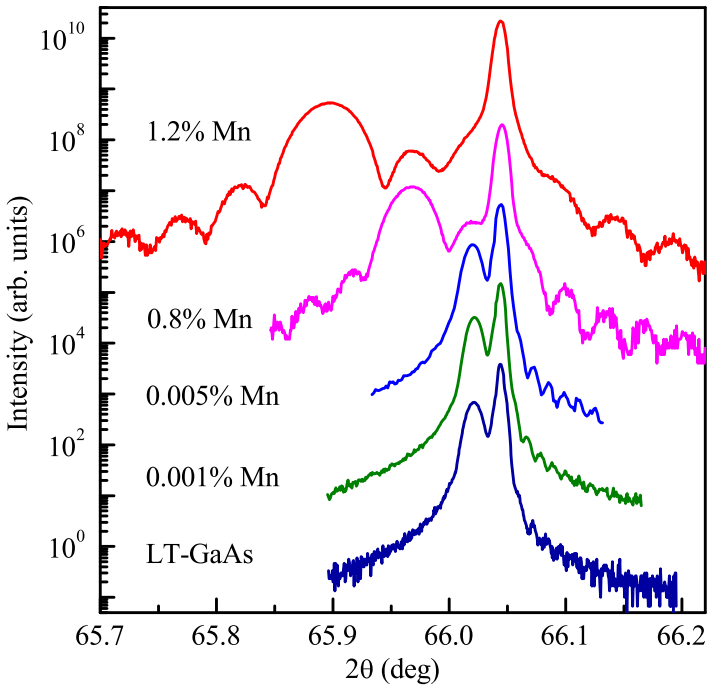

FIGURE 3.1: The HR-XRD results: $2\theta/\omega$ scans for (004) Bragg reflections for the LT-GaAs and (Ga,Mn)As epitaxial layers grown on the (001) semi-insulating GaAs substrate. The curves were vertically offset for clarity. The narrow line corresponds to the reflection from the GaAs substrate, and the broader peaks at lower angles are the reflections from the layers. With the increasing Mn content the (Ga,Mn)As diffraction peaks shift to smaller angles with respect to that of the LT-GaAs reference layer.

with regard to that of the GaAs substrate. The shift is a result of larger lattice parameters caused by incorporation of a large amount of As_{Ga} defects in LT-GaAs and, additionally, Mn interstitial defects in (Ga,Mn)As. Due to Mn doping in GaAs, the unit cell of the layers changes with the increasing lattice mismatch. The zinc-blende cubic structure of GaAs transforms into the tetragonal structure whose the perpendicular lattice parameter is larger than the lateral one (GaAs substrate lattice parameter). Using the values of the angular positions of diffraction peaks, it was possible to calculate the perpendicular lattice parameters (c), the relaxed lattice parameters (a_{rel}) - assuming the (Ga,Mn)As elasticity constants to be the same as for GaAs, the layer/substrate lattice mismatch, and the vertical strain. The Mn composition of the (Ga,Mn)As layers

determined from the epitaxial growth parameters is consistent with those obtained from HR-XRD. The results of HR-XRD analysis are listed in Tab. 3.1.

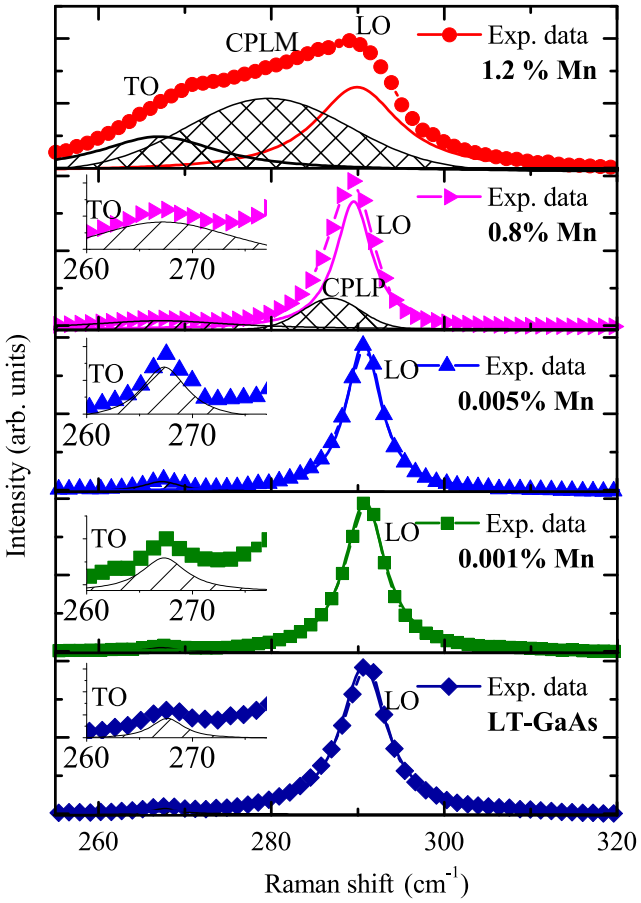

FIGURE 3.2: Raman spectra for the (001) surfaces of the reference layer (LT-GaAs) and four (Ga,Mn)As layers, where full symbols represent the experimental data. Data were recorded at RT in the backscattering configuration. The intensities were normalised. The spectra with $x \leq 0.005\%$ were decomposed into the two components of the TO- and LO-phonons, whereas for $x \geq 0.8\%$ the three components were found: the TO- and LO-phonons (solid lines) and the CPLM (cross-hatched area). Reproduced from [14], with the permission of AIP Publishing.

Fig. 3.2 shows the Raman scattering spectra for the (Ga,Mn)As layers and the reference LT-GaAs. The spectra were recorded in the backscattering configuration from the (001) surface where the laser excitation activates only the LO phonons and the TO mode is symmetry-forbidden [131]. The weak signal from the TO phonon is observed due to the disorder-related scattering provided by residual strain in the epitaxial layers causing slight deviations from

the (001) surface orientation [131, 132]. The TO phonon mode is present in all the spectra presented in Fig. 3.2 and the relative intensity of this mode increases with the increasing Mn content and the lattice mismatch in the layers, as shown in Tab. 3.1. All the first-order micro-Raman spectra revealed a clear signal from the LO phonons. LT-GaAs and the (Ga,Mn)As layers with very low (0.001% and 0.005%) Mn contents were fitted using two Lorentzian line-shapes attributed to symmetry-forbidden TO phonons and from the LO phonons. Nevertheless, a similar two-component approach was not sufficient for the spectra of (Ga,Mn)As layers with higher Mn contents (0.8% and 1.2%) because of the emergence of hole-plasma related CPLM [125]. Hence, three contributions of Lorentzian shape were taken into account, corresponding to the CPLM and the TO- and LO-phonon lines, as shown in Fig. 3.2. Applying the method of estimation of the hole density in (Ga,Mn)As after Seong et al. [127] and comparing them with the literature data, [127, 131], the estimated hole concentrations are $0.5 \times 10^{19}\text{cm}^{-3}$ and $8 \times 10^{19}\text{cm}^{-3}$ in the (Ga,Mn)As layers with x equals to 0.8% and 1.2%, respectively.

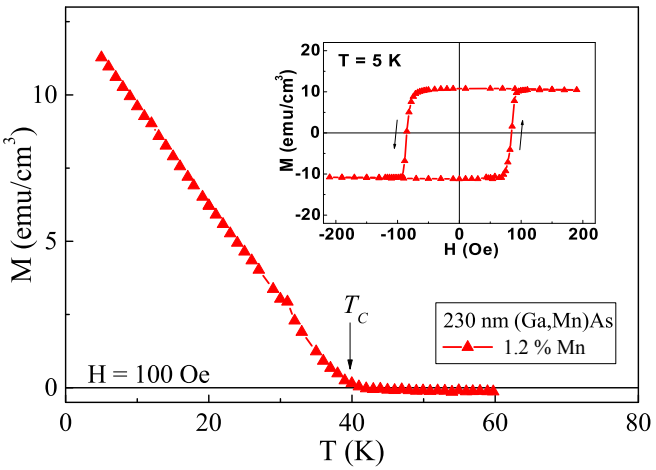

FIGURE 3.3: SQUID magnetisation along the in-plane [110] crystallographic direction vs temperature for the 230-nm-thick (Ga,Mn)As film. The magnetisation hysteresis loop measured at a temperature of 5 K is shown in the inset.

The ferromagnetic ordering is exposed for the layer with the highest, $x =$

1.2% Mn content only with T_C of about 40 K, shown in Fig. 3.3. The well-defined hysteresis loop measured at 5 K is shown in the inset of Fig. 3.3.

Photoreflectance studies

The RT-PR spectra of the LT-GaAs and (Ga,Mn)As epitaxial layers measured from 1.35 to 1.70 eV are shown in Fig. 3.4. The intensities of the spectra are normalised for clarity. The experimental spectra of LT-GaAs, as well as (Ga,Mn)As, expose the electric-field-induced FKOs at the energies above the fundamental absorption edge [133]. The thinnest layer with $x = 1.2\%$ Mn content and 230 nm thick, exhibits an additional, below-band-gap feature at about 1.42 eV. This feature is related to a PR signal originating from the layer-substrate interface region and is negligibly small for thicker layers.

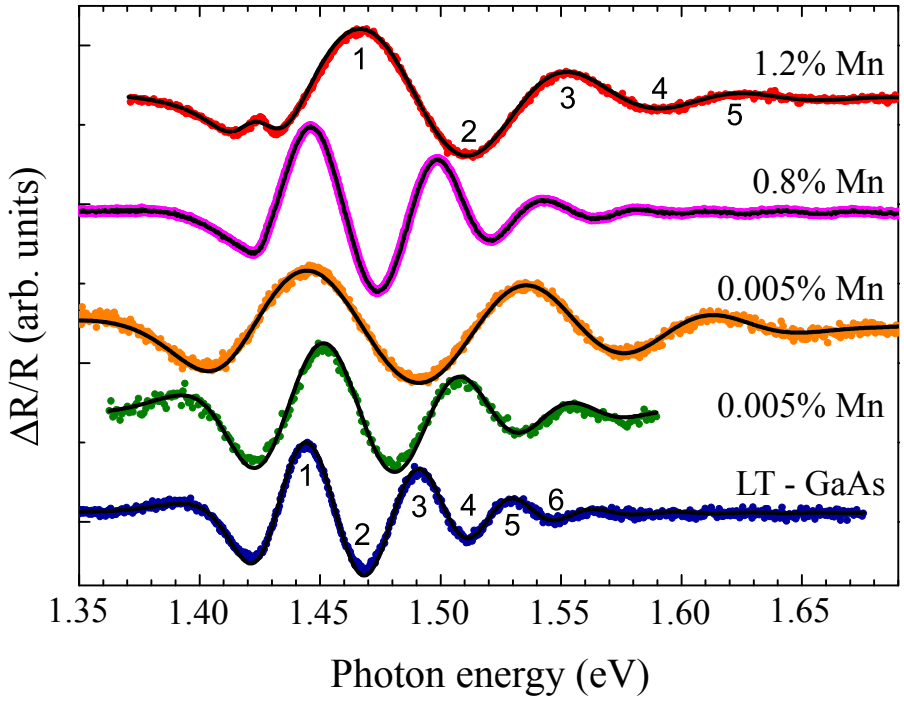

FIGURE 3.4: Modulation PR spectra of four (Ga,Mn)As layers with various Mn contents and the reference LT-GaAs epitaxially grown on the GaAs substrate. The FKOs extrema are denoted by numbers. The spectra were normalised to the same intensity and vertically offset for clarity. Solid lines represent the full-line-shape fit of the experimental data. Reproduced from [14], with the permission of AIP Publishing.

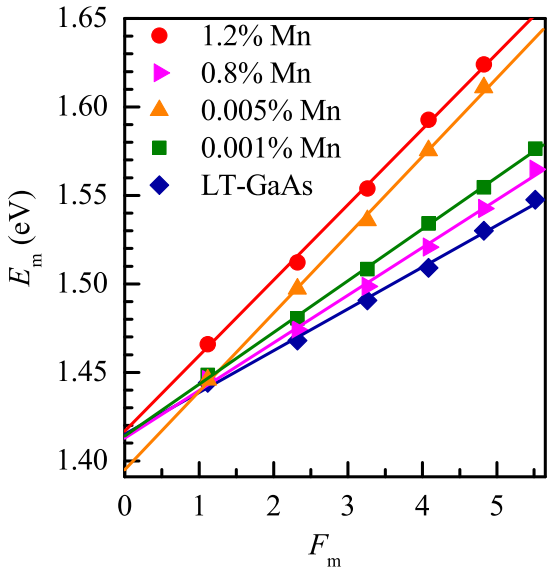

FIGURE 3.5: Linear dependencies of the FKO extrema energy as a function of the extrema index for (Ga,Mn)As with various Mn contents and LT-GaAs layers. Solid lines represent the linear fits in accordance to Eq. 2.6. Reproduced from [14], with the permission of AIP Publishing.

Sydor et al. [134] investigated such a spectral feature for a set of differently doped layers with various thicknesses grown on the semi-insulating GaAs substrate by MBE. The below-band-gap feature distorts the band-gap-transition PR signal. The interface source of this feature is verified by studies of the relation between the incidence angle of the laser beam and the intensity of the components in the PR spectra. The modulation mechanism for this feature can be caused by the thermal excitation of traps or impurities at the interface and their quick refilling by the laser-injected carriers [134]. In the previous PR investigations carried out by Yastrubchak et al. [87], the (Ga,Mn)As layers with x up to 6% and thicknesses up to 300 nm exhibit the below-band-gap feature in the PR spectra.

The experimental PR spectra from Fig. 3.4 were fitted using the complex Airy functions and their derivatives describing FKO (Eq. 2.4) [119]. The full-line-shape analysis allowed to determine the optical gap transition, E_0, and the electro-optic energies, $\hbar\theta_{lh}$ and $\hbar\theta_{hh}$, for LH and HH, respectively, in the investigated epitaxial layers. For the thinnest (Ga,Mn)As layer (x = 1.2%),

the PR spectral feature related to the layer-substrate interface is described by the Aspnes's TDLS function [121] (Eq. 2.2). Solid lines in Fig. 3.4 represent the fits. The best fit parameters of E_0, $\hbar\theta_{lh}$ and $\hbar\theta_{hh}$ for all studied layers are summarised in Tab. 3.2. The energy value of E_0 optical transition obtained for the LT-GaAs film is in good agreement with the results of 1.42 eV obtained earlier for LT-GaAs by Giordana et al. [135] in the PR spectroscopy studies. The energies of the band gap optical transition were examined, also using the simplified method based on the analysis of FKO energy positions in the PR spectra (described in Chapter 2.2). The linear dependences of E_m vs. F_m derived from FKO for all the PR spectra are plotted in Fig. 3.5. The values of E_G and $\hbar\theta$, obtained using Eq. 2.6 are listed in Tab. 3.2. One can see that the E_G (band gap energies for the simplified method) values are smaller than the E_0 critical-point energies obtained from the full-line-shape analysis of the PR spectra but behave similarly with increasing x. The values of $\hbar\theta$, obtained from the analysis of FKOs periods differ from those of $\hbar\theta_{\mathrm{hh}}$. However, their values also behave similarly with increasing x, which substantiate the correctness of the two approaches used in the analysis of the measured PR spectra in the examined series of samples. Thorough inspection of the results presented in Tab. 3.2 shows that the values of E_0 and E_G critical-point energies, in the (Ga,Mn)As layers decrease, while increasing the Mn content up to 0.005%. A further increase in the Mn content leads to the increase of those energies. For the (Ga,Mn)As layer with 1.2% Mn content the critical point energies obtained with both methods are larger than those in the LT-GaAs layer. In order to interpret these results, the band-structure evolution with the increasing Mn concentration in the small Mn content (Ga,Mn)As is proposed and schematically shown in Fig. 3.6.

In LT-GaAs, a large concentration of $\mathrm{As_{Ga}}$ defects forms $\mathrm{As_{Ga}}$-related defect bands in the middle of the band gap with the Fermi energy pinned therein [23, 136], as schematically shown in Fig. 3.6 a. The $\mathrm{As_{Ga}}$ band is not entirely filled. The double donor defects are compensated by residual carbon and native

TABLE 3.2: The values of transition energies E_0 and electro-optic energies for LH and HH, $\hbar\theta_{\rm lh}$ and $\hbar\theta_{\rm hh}$, respectively, obtained from the full-line-shape analysis of the PR spectra shown in Fig. 3.4 a), and the values of energies E_G and electro-optic energies $\hbar\theta$, obtained from the analysis of the FKOs period presented in Fig. 3.5.

x (%)	E_0 (eV)	$\hbar\theta_{\rm lh}$ (meV)	$\hbar\theta_{\rm hh}$ (meV)	E_G (eV)	$\hbar\theta$ (meV)
0	1.423	25.91	22.01	1.415	23.64
0.001	1.416	32.13	26.67	1.414	29.21
0.005	1.407	52.6	42.32	1.395	44.35
0.8	1.42	28.5	23.23	1.413	26.94
1.2	1.429	50.12	38.3	1.417	42.69

V_{Ga} acceptors (gallium vacancy). Therefore, the As_{Ga} band allows for hopping conduction in LT-GaAs [137]. The predominant feature in the PR spectra originates from the band-to-band optical transition marked with an arrow in the same picture. In the (Ga,Mn)As layers with very small x and n-type hopping conductivity, the Fermi level position is still within the band gap. However, its energy position is determined by the compensation between the total amount of incorporated acceptors (residual C, V_{Ga}, and Mn_{Ga}), and the donor defects. It is assumed that the decrease in the optical gap energy with respect to that in LT-GaAs, is due to build-up of the top of the valence band with Mn-related impurity states, as shown schematically in Fig. 3.6 b), referring to the (Ga,Mn)As layer with $x = 0.005\%$. This assumption is consistent with the results of the four-wave mixing spectroscopy experiments by Yildirim et al. [89] who observed a strong increase in the optical response just below the GaAs band gap for a similar sample with the 0.005% Mn content. This observation also was attributed to an increase in the density of states near the valence band edge caused by hybridisation between the p states of the host GaAs valence band and the d levels of the Mn_{Ga}. On the other hand, the peak of their four-wave mixing spectra obtained for higher x, namely 0.045% and 0.1%, shifts to higher photon

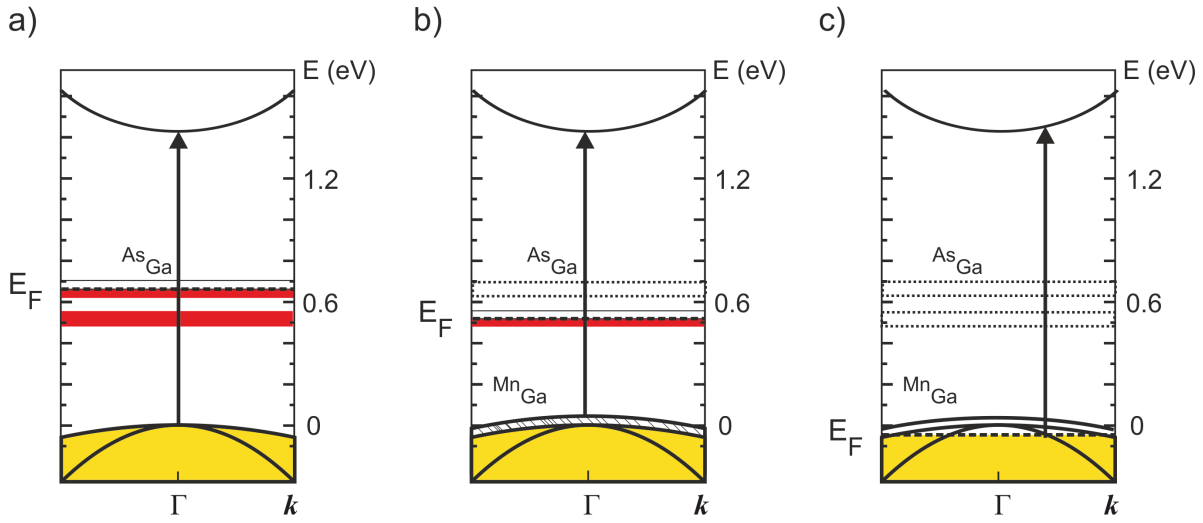

FIGURE 3.6: Band structure diagram in the vicinity of Γ point of the Brillouin zone for LT-GaAs (a) and its evolution for the increasing x in (Ga,Mn)As for n-type (b) and p-type (c). Splitting of the bands due to spontaneous magnetisation is neglected for simplicity. Arrows indicate the electronic excitations from the valence band to the conduction band. The Mn_{Ga}-related impurity states are assumed to be merged with the valence band in the cases (b) and (c). In p-type (Ga,Mn)As the Fermi level position lies within the valence band leading to a k-space shift of the optical transition from the centre of the Brillouin zone, as shown in (c). Reproduced from [14], with the permission of AIP Publishing.

energies [89].

The PR results for the (Ga,Mn)As layers with 0.8% and 1.2% Mn contents and p-type conductivity proved by Raman scattering spectroscopy, shows an increase in the interband transition energy. It is interpreted as the Burstein-Moss effect causing the blue-shift of the absorption edge due to the lowering of the Fermi level energy within the valence band [64]. The band structure related to the (Ga,Mn)As layer with $x = 1.2\%$ is schematically shown in Fig. 3.6 c). It displays the Fermi level position below the top of the GaAs valence band and increases the energy of the band-to-band transition due to the band filling effect.

TABLE 3.3: The Mn contents obtained from the SIMS and HR-XRD results, the values of the out-of-plane strain obtained by HR-XRD and hole densities estimated from the Raman spectra for the LT-GaAs and (Ga,Mn)As layers.

% Mn (SIMS)	% Mn (HR-XRD)	out-of-plane strain $\pm 0.1(\times 10^{-4})$	Hole density (cm^{-3})
0 (LT-GaAs)	-	0.2	-
0.0007	-	0.2	-
0.02	-	0.9	-
0.3	0.3	1.4	2×10^{18}
0.9	0.7	3.2	5×10^{19}
1.6	1.4	6.2	1×10^{20}

3.1.2 Low temperature photoreflectance studies

Structural, electronic, and magnetic properties

A set of 100-nm-thick (Ga,Mn)As layers, with the Mn contents x from 0 (an LT-GaAs reference layer) to 1.6% was prepared by the LT-MBE technique. The GaAs (001) semi-insulating substrate temperature was approximately 230°C during the epitaxial growth. The Mn_{Ga} incorporation was maximised and As_{Ga} and Mn_I defects concentration was reduced by tailoring the substrate temperature depending on the intentional Mn content in the (Ga,Mn)As layers. Moreover, the layers were grown under the so called optimised conditions, that is, with the As_2/(Ga + Mn) flux ratio close to the stoichiometric one, calibrated using test samples. The reference layer, LT-GaAs, was grown at a slightly lower temperature than the (Ga,Mn)As films with $x \leqslant 0.02\%$, and therefore a larger concentration of As_{Ga} defects is expected. Additionally, the LT-GaAs and (Ga,Mn)As ($x = 1.6\%$) layers were grown on conductive p-type GaAs substrate for the in-situ photoemission studies to prevent sample charging effects. The 2D growth of the layers was controlled by RHEED [138].

Fig. 3.7 shows $2\theta/\omega$ curves for the (004) Bragg reflections for all investigated samples obtained from the HR-XRD measurements. The lack of X-ray fringes

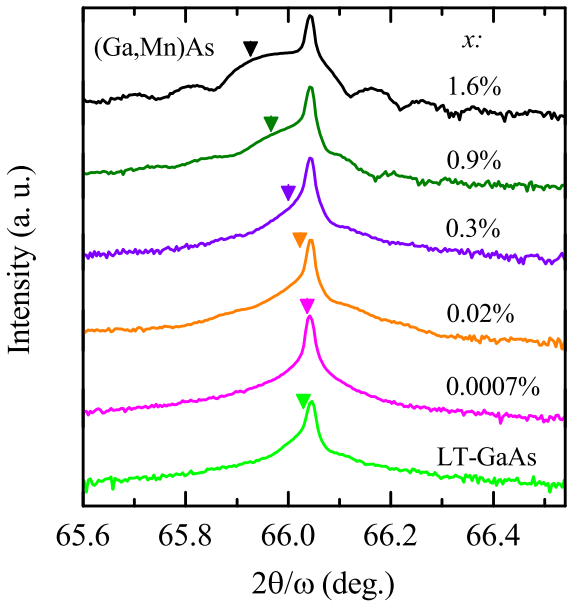

FIGURE 3.7: The HR-XRD patterns of the studied layers: $2\theta/\omega$ scans ($\lambda_{CuK\alpha 1}$) of (004) Bragg reflections for the LT-GaAs and (Ga,Mn)As layers. The narrow features are denoted to the reflections from the GaAs substrate. The features marked with arrows are the reflections from the epitaxially grown layers. Their positions for the LT-GaAs and (Ga,Mn)As layers with $x = 0.0007\%$ and 0.02% are very close to the main reflection from the GaAs substrate. The Mn contents (x) were determined by secondary ion mass spectrometry (SIMS). ©2018 by the American Physical Society [13]

for the layers with $x \leqslant 0.3\%$ (including the reference layer) indicates that differences between the lattice parameters of these layers and the substrate are very small. This is as a result of optimised epitaxial growth conditions and incorporation of a low amount of As_{Ga} defect (in the range of $10^{19}cm^{-3}$ [128]). However, a larger quantity of As_{Ga} defects in LT-GaAs than in the lowest doped (Ga,Mn)As layers is expected due to a slightly lower substrate temperature during the epitaxial growth. Clear X-ray interference fringes were revealed for the samples with $x \geqslant 0.9\%$ demonstrating a good quality of the interfaces and great structural perfection of the layers. It was possible to calculate the layer thickness from the angular spacing of the fringes for the $x = 1.6\%$ layer that corresponds very well to the value derived from the RHEED and SIMS measurements. The diffraction peaks representing the (Ga,Mn)As layers shift

to smaller angles, as compared to the GaAs substrate peak angle. This is expected because of larger perpendicular lattice parameters with increasing x in the compressively strained layers grown pseudomorphically on GaAs [128]. The angular positions of diffraction peaks were used to calculate the perpendicular (c) and the relaxed lattice parameters (a_{rel}) of the layers, assuming the values of elasticity constants for GaAs. The lattice parameters were used to calculate the out-of-plane strain in the layers, defined as $(c - a_{\mathrm{rel}})/a_{\mathrm{rel}}$. Tab. 3.3 summarises the calculated parameters and, in addition, shows the values of Mn contents estimated from HR-XRD and SIMS with a good agreement between the two methods. In the remaining part of this section, the x values obtained with SIMS are used to label the layers.

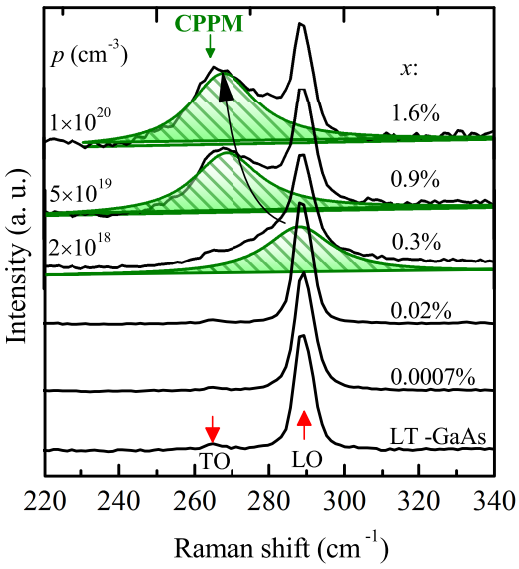

FIGURE 3.8: Micro-Raman spectra of the studied (Ga,Mn)As and LT-GaAs epitaxial layers. Only LO, weak TO phonon modes are found for $x \leq 0.02\%$. The CPLM feature (hatched area) indicating a p-type character of the layers emerges for $x \geq 0.3\%$. The estimated hole densities (p in cm^{-3}) are listed on the left-hand side of the corresponding spectra. ©2018 by the American Physical Society [13].

Raman spectroscopy was used to evaluate the electronic properties of the layers by the analysis of the hole plasma related CPLM feature in the spectra. Measurements were done using a 514 nm Ar^+ ion laser line in the backscattering

configuration at room temperature with the spectral resolution of 1 cm^{-1}, shown in Fig. 3.8. The spectra of LT-GaAs and (Ga,Mn)As layers with x=0.0007% and 0.02% revealed only a strong LO phonon line and a very weak (symmetry-forbidden) TO phonon line located near 290 and 265 cm^{-1}, respectively. For the current set of samples about 0.3% of Mn was needed to compensate the double donor defects (mainly As_{Ga} [137]) introduced due to the LT-MBE growth. The compensation of defects allowed to form the CPLM band in the Raman spectra, indicating that at this concentration of Mn the layer turns p-type. With the further increase in x, the CPLM shifts towards the TO-phonon-line wavenumber and dominates the spectra. This is the direct evidence of an increasing holes density with x. The full line-shape fitting was performed using a generalisation of Drude theory of the CPLM, assuming LO-phonon damping, effective masses of LH and HH for GaAs and plasmon damping (Chapter 2.3) [125, 139]. The values of plasmon damping were estimated basing on the typical carrier mobilities from Ref. [80], namely, 15 cm^2/Vs (x = 0.3% and 0.9%) and 9 cm^2/Vs for the sample with x = 1.6%. The hole densities determined from the fits are given in Fig. 3.8 and listed in Tab. 3.3.

SQUID magnetometry did not reveal ferromagnetic coupling in the studied layers with x up to 0.3% down to 1.8 K due to an insufficient amount of Mn dopant present for such low doping levels in the 100-nm-thin layers [140]. Only the paramagnetic response can be seen in the p-type 0.3% sample but the so small concentration of holes (2×10^{18} cm^{-3} - (well below the Mott critical concentration, $p_C \sim 10^{20}$ cm^{-3})) is too low to bring up the long-range magnetic interactions at the studied temperature. The further increase in x (up to 0.9%) and in p up to the Mott critical concentration brings in a superparamagnetic-like response shown in Fig. 3.9.

Its presence is revealed by the temperature-dependent studies at the weak magnetic field. A magnetically composite (granular) character of the sample

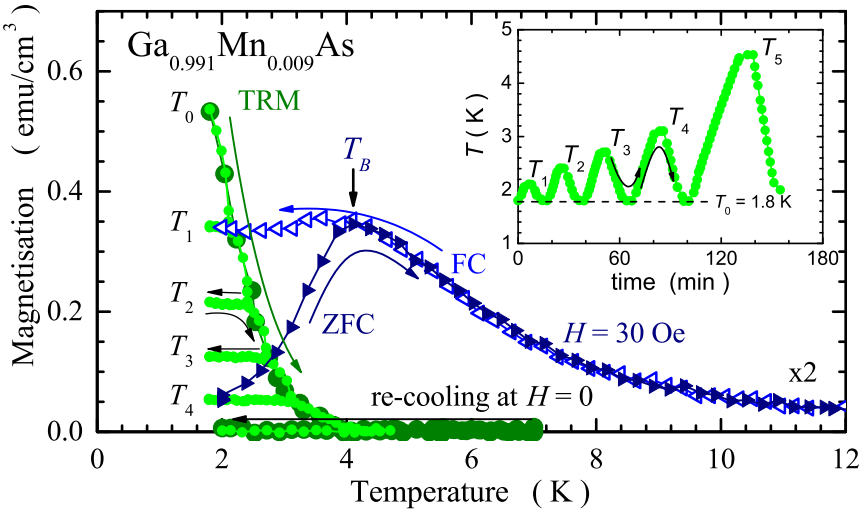

FIGURE 3.9: Temperature-dependent studies of $x = 0.9\%$ (Ga,Mn)As layer at low magnetic field. The thermoremnant magnetisation (TRM) measured in two modes: (light circles) the thermal cycling between T_0 and progressively higher temperature (T_1 through T_4), as shown in the inset, and (dark circles) TRM collected during warming the sample from $T_0 = 1.8$ K until the signal vanishes and then during re-cooling down to T_0 under the same zero-field conditions. The triangles illustrate the temperature-dependent magnetisation measured using zero-field cooling (ZFC, full triangles) and field cooling (FC, open triangles) routines at 30 Oe. T_B indicates the mean blocking temperature, and the arrows mark the directions of temperature sweeps. ©2018 by the American Physical Society [13].

can be deduced from rapid decay with temperature thermoremnant magnetisation (TRM) associated with a maximum in the Zero Field Cooling (ZFC) trace. The ferromagnetic coupling is already present in this sample but it is sustained only in the mesoscopic volumes distributed in the paramagnetic host. The mean blocking temperature (T_B) is related to a mean volume (V) of local ferromagnetic regions by $25k_BT_B = KV$, where K, the anisotropy constant in (Ga,Mn)As ranges between 5000 and 50000 erg/cm^3 [141], k_B is the Boltzmann constant, and the factor 25 is set by the experimental time scale- about 100 s, in SQUID magnetometry. T_B=4 K corresponds to a mean volume of spheres with the diameters between 8 and 20 nm. The thermal cycling of the TRM

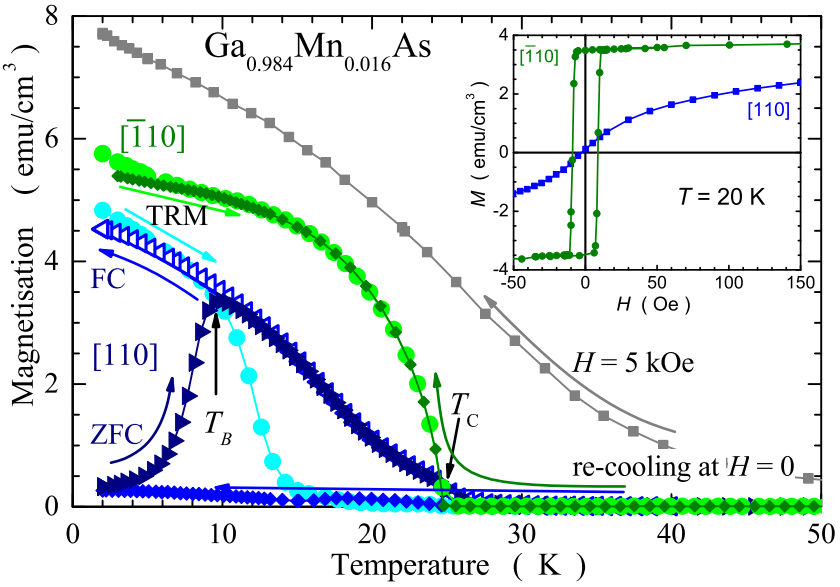

FIGURE 3.10: Temperature-dependent measurements of (Ga,Mn)As layer with $x = 1.6\%$ revealed coexistence of mesoscopic and microscopic ferromagnetic components of the sample. Bullets and diamonds of light and dark hues of green and blue indicate the thermoremnant magnetisation (TRM) and the re-cooling measurement to the base temperature under the $H = 0$ Oe condition along in-plane [–110] and [110] orientations, respectively. T_C indicate the Curie temperature for this sample. The triangles indicate the temperature dependences of magnetisation measured at 30 Oe using zero-field cooling (ZFC, full triangles) and field cooling (FC, open triangles) routinnes. T_B marks the mean blocking temperature. Full squares indicate the magnetisation at 5 kOe. The arrows indicate the directions of temperature sweeps. The inset shows the isothermal magnetisation field sweeps at 20 K for [–110] (bullets) and [110] (squares). ©2018 by the American Physical Society [13].

shown in Fig. 3.9 brings up another evidence confirming the magnetically inhomogeneous structure of this layer. This type of measurement reveals that the remnant magnetisation is reduced only after incremental warmings (from T_i to T_{i+1}), following the original TRM trace. When the sample is cooled, the TRM value remains fairly constant, and is insensitive to temperature changes in any directions between the T_i and T_0. Therefore the dominant role of the thermal agitation over the individual energy barriers specific to each mesoscopic ferromagnetic volume is inferred. Finally, a lack of any magnetic moment maintained by this sample during re-cooling at $H = 0$ Oe from a temperature at

above which the TRM dropped to zero confirms the absence of long-range ferromagnetic phase in the layer, despite the fact that a nonzero TRM occurs before re-cooling. Increasing x to 1.6% brings in the global long-range ferromagnetic coupling. That can be inferred from the TRM trace along [-110] in-plane direction which exhibits Brillouin-like concave curvature and a quite rapid drop to the zero magnetic moment at the T_C characteristic of the global ferromagnetic phase, shown in Fig. 3.10. More importantly, after the re-cooling from above T_C the magnetisation signal follows the initial TRM trace. The inset of Fig. 3.10 and similar values of remnant and spontaneous magnetisations infer relatively strong in-plane uniaxial magnetic anisotropy [141]. However, the difference between magnitudes of the saturation magnetisation measured at H = 5 kOe and the spontaneous (and thermoremnant) magnetisation indicates that only a part of Mn spins contributes to this global coupling in the layer. To determine the magnetic properties of these Mn spins which do not support the spontaneous magnetisation, the temperature-dependent studies at H = 0 Oe along the uniaxial hard (the [110] direction) were performed. The magnetic response along [110] direction is qualitatively the same as that of the x = 0.9%, the superparamagnetic sample. TRM decreases more quickly than in the magnetisation along the easy axis and after re-cooling the magnetic moment it also remains to be zero. Furthermore, the ZFC-FC temperature cycling exhibited the superparamagnetic-like behaviour with a characteristic maximum on the ZFC trace and a strong bifurcation between FC and ZFC below T_B = 10 K. This higher value compared to the sample with x = 0.9% corresponds to the somewhat larger diameter of 10 nm to 25 nm and is related to a larger hole density and x. Interestingly, in the samples with x = 1.6% the ferromagnetic and superparamagnetic components have orthogonal easy axes allowing their clear experimental separation. This is possible due to uniaxial magnetic anisotropy in (Ga,Mn)As whose magnitude and sign depend largely on the hole density.

Therefore, the spatially limited ferromagnetic order displayed as a superparamagnetic response originates from the regions with low hole density and provided from those parts of the sample where ferromagnetism is spread by itinerant holes.

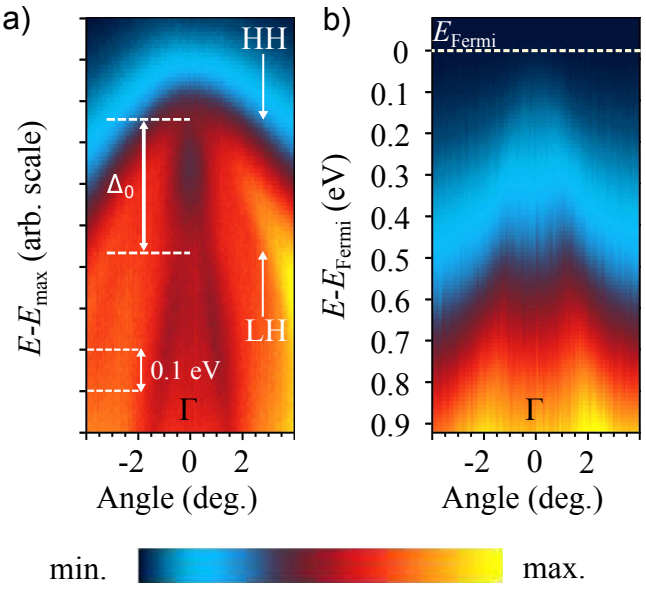

FIGURE 3.11: Angle-resolved photoemisson spectroscopy (ARPES) of (a) LT-GaAs and (b) (Ga,Mn)As 1.6% Mn performed at $T \approx 20$ K. The arrows indicate heavy (HH), light (LH) hole subbands, and split-off energy (Δ_0). The marked spectral features are distinguishable only in the case of LT-GaAs spectrum. Drop of the photoemission intensity below the Fermi level does not allow to distinguish the GaAs-like valence band (VB) features in the low-doped (Ga,Mn)As spectrum. ©2018 by the American Physical Society [13]

The valence band dispersion and the density of states near the top of the valence band in the low-Mn-doped ferromagnetic layer were examined using the angle-resolved photoemission spectroscopy (ARPES). *In-situ* measurements were performed mainly to avoid the issues of the high reactivity of Mn-rich (Ga,Mn)As surface [107, 142].

The ARPES was measured at the MAX-IV synchrotron radiation facility at I3 beamline vacuum-connected to the MBE growth chamber, enabling to transfer the sample directly in the ultra high vacuum between MBE and ARPES setup. Before the measurement, the sample was also examined by the low

energy electron diffraction in the preparation chamber which showed the c(4× 4) and (1×2) surface reconstruction patterns typical of LT-GaAs and (Ga,Mn)As, respectively. For the photoemission experiments, the excitation energy 22.5 eV and p polarisation were used. The samples were cooled to about 20 K. The spectrum of (Ga,Mn)As was smoothed with a cubic spline function. The Fermi level was determined using the metallic Mn stripe located at the border of the wafer. The region of the top of the valence band, the valence band maximum (E_{max}) and the Fermi level (E_{Fermi}), are displayed in Fig. 3.11. In the case of LT-GaAs, the spectrum reflects the curvature of the valence band dispersion with the HH and split-off bands. The Fermi level is located in the middle of the band gap due to the existence of uncompensated double-donor defects introduced by the low-temperature growth conditions [107]. As follows from Fig. 3.11(b), Mn doping modifies significantly the top valence band structure of (Ga,Mn)As compared to LT-GaAs. One can see that the spectrum is deformed and does not allow to distinguish band edges of the split-off band as clearly as in the case of LT-GaAs (Fig. 3.11(a)). The spectra of (Ga,Mn)As revealed the lack of the sharp band edges, as compared to LT-GaAs. Instead, one can notice a decrease in the photoemission intensity with the approaching E_{Fermi} without a sudden increase near the Fermi level, which could suggest the existence of a detached and dispersion-less band-related density of states for such a low Mn-doping level. The ARPES results are consistent with those in Ref. [107] and the results in Ref. [109] for low T_C (Ga,Mn)As inferring the small influence of the Coulomb gap on the density of states near the Fermi level.

Photoreflectance studies

The PR studies were carried out to obtain the values of the optical-energy-gap in (Ga,Mn)As with the increasing Mn content. The collected LT-PR (ΔR/R) spectra, presented by open circles in Fig. 3.12(a) were fitted using the TDLS function (equation 2.2). The fitted single spectral components were integrated

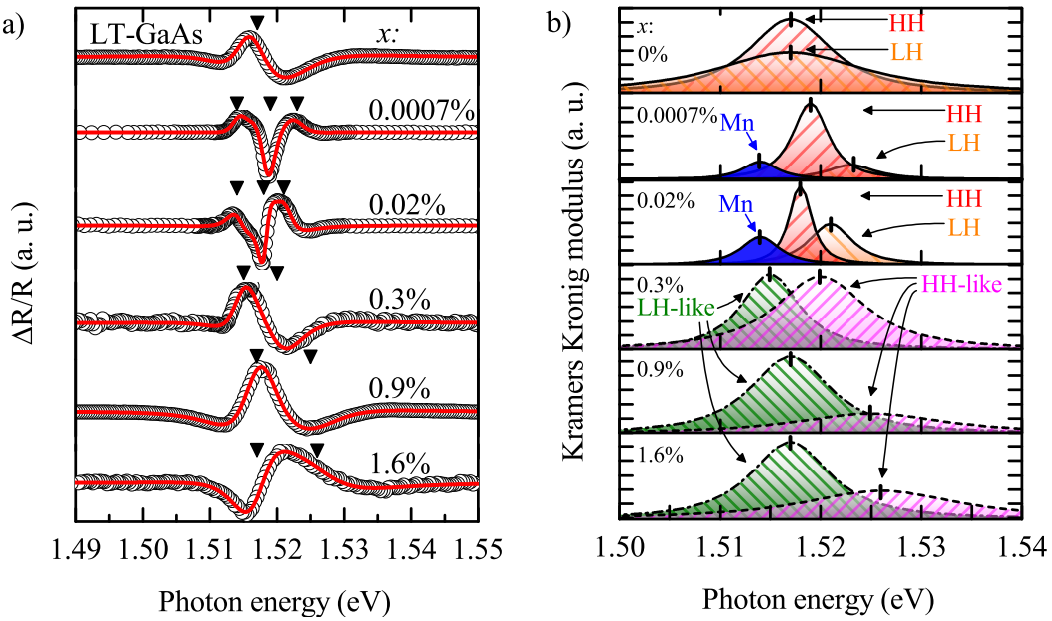

FIGURE 3.12: (a) $\Delta R/R$ spectra of the LT-GaAs and (Ga,Mn)As layers (open circles) and fits with TDLS line-shapes (line). Arrows mark the transition energies. (b) decomposition of $\Delta R/R$ spectra using Kramers-Kronig integration of the fitted TDLS features. The LT-GaAs layer spectrum revealed heavy-hole (HH) and light-hole (LH) subband features (diagonally hatched). After Mn doping the low energy feature (solid filled one, marked with "Mn") emerges accompanied with the energy separation of the HH and LH features. For $x \geqslant 0.3\%$ and n- to p-type transition, the character of the spectra evolves into two broadened features instead of three. ©2018 by the American Physical Society [13]

using the Kramers-Kronig (KK) relations (equations 2.7, 2.8) shown in Fig. 3.12(b).

As expected, the LT-PR spectrum of the reference LT-GaAs layer revealed two spectral features shown in Fig. 3.12(b), of the same energy representing optical transitions between the light hole (LH) and heavy hole (HH) valence subbands and the conduction band (CB). In turn, the LT-PR spectra of (Ga,Mn)As with x =0.0007% and 0.02% display the two valence-band contributions, and the additional lower-energy peak (denoted by the dark solid filling in Fig. 3.12(b)). Moreover, the HH-CB and LH-CB optical transitions differ from those of the LT-GaAs spectrum - they are energetically separated and blue shifted with respect to those of the reference layer. Additionally, the widths of the peaks are

smaller compared to the LT-GaAs spectrum. This narrowing is caused by a slightly higher growth temperature of the two n-type (Ga,Mn)As films compared to LT-GaAs resulting in the generation of fewer As_{Ga} trap states within the band gap. A smaller quantity of defects in the crystallographic structure extends the lifetime of photogenerated carriers and therefore it decreases the spectral feature broadening. The appearance of the LT-PR spectra is significantly changed for the layers with $x \geqslant 0.3\%$. One can see only two broad features. In the $x = 0.3\%$ layer, the lower-energy peak is red-shifted compared to the HH feature in the spectrum of $x = 0.0007\%$ layer. However, for the other layers, the low energy peak, which becomes dominant, slightly shifts to higher energies. Furthermore, the separation between the two features and their broadening increases with the Mn content.

In the Mn concentration range in (Ga,Mn)As, between $x = 0\%$ and 1.6% the transition from presumably the n-type and p-type conductivities is shown. In particular, Mn concentration $0.02\% \leqslant x_b \leqslant 0.3\%$, to be the bordering one can be identified. The Mn-related impurity states were revealed by the LT-PR studies as the additional below-band-gap peak, besides the HH and LH-related spectral features. The appearance of this band results in a red shift of the optical gap energy in p-type but nearly compensated (Ga,Mn)As as compared to LT-GaAs - confirming the earlier results in the PR spectra obtained at room temperature, reported in section 3.1.1. HH-LH splitting observed as low- and high-energy peaks in the KK analysis of LT-PR may be related to hybridisation of the valence band states in the presence of Mn impurities. The sketches of the band structure cases for LT-GaAs and $x \leqslant x_b$ (Ga,Mn)As are schematically shown in Figs. 3.13(a) and 3.13(b), respectively. The LT-PR spectra change completely when x exceeds x_b, showing only two broadened features. The lack of the below-band gap spectral feature related to the filled Mn impurity states and broadening of the two observed spectral features indicate that the Fermi level is located below top of the valence band. The energy positions of the

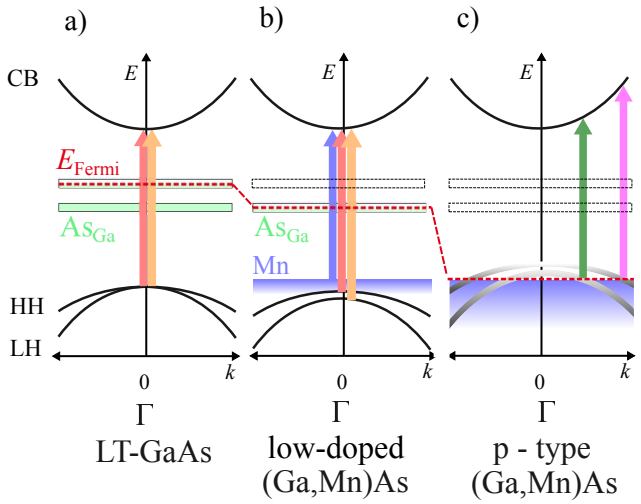

FIGURE 3.13: The schematic diagram for (a) LT-GaAs, (b) n-type, and (c) p-type (Ga,Mn)As band structure. The interband optical transitions are marked with arrows. For LT-GaAs the transitions originate from the heavy (HH) and light (LH) hole valence subbands at the Γ critical point of the Brillouin zone. For n-type (Ga,Mn)As, a slight splitting of the valence subbands is observed together with appearing the additional Mn-related below-band-gap transition. In this case the Fermi level moves downward with the increasing Mn content due to the partial compensation of As_{Ga}-related donors. For p-type (Ga,Mn)As the Fermi level goes below the top of the valence band causing a k-space shift of the HH- and LH-related interband transitions. The valence band extends into the band gap due to Mn states and carrier-induced many-body effects. ©2018 by the American Physical Society [13]

spectral features in the LT-PR spectra indicate rather small influence of strain. Taking into account the shear potential (b=-2 eV), elastic constants (C_{11}=119 GPa, C_{12}=53.8 GPa [143]), and spin-orbit splitting (Δ_0=0.34 eV) for GaAs the HH-LH splitting at $k = 0$ can be estimated to be approximately 2 meV for the calculated out-of-plane strain in the layer with x=1.6% - much smaller than observed here. Therefore, the splitting of the two spectral features can be interpreted by the optical transitions occurring at $k \neq 0$. It makes that the HH-CB transition is higher in energy than LH-CB due to the Fermi level position in the valence band, as sketched in Fig. 3.13(c). In the $x = 0.3\%$ case, the observed red shift is due to the carrier-induced many-body band-gap

renormalisation [35, 144] which dominates evidently over the band filling effect for such a low p. That is also supported by the similar magnitudes of the KK peaks in the spectra indicating a shallow Fermi level position in the valence band and that both optical transitions originate from the similar k wavevector. In line with such an interpretation, LH-CB and HH-CB optical transitions are assigned to the low- and high-energy features in the KK analysis, respectively. Such a scenario requires the p-type character of all $x \geqslant 0.3\%$ layers and indeed, it is corroborated by the Raman spectroscopy studies, which proved the presence of the hole-related CPLM structure showing that intensity increases with x. Nonetheless, an expected substantial blue Burstein-Moss shift of the optical gap (on increasing x) was not observed. This is a further consequence of the band gap renormalisation-related narrowing effects, which also arise with the increase in p. Nevertheless, lowering of the Fermi level into the valence band postulated here is reflected by the difference in the amplitudes and broadening of these two LT-PR peaks, seen in the KK analysis spectra. In the first case, the optical transition probability decreases with the k vector value moving further away from the center of the Brillouin zone, where k=0. The latter one results from the transition energy uncertainty which depends (inversely proportional) on a finite lifetime of photogenerated carriers interacting with the hole plasma. This interpretation of the band structure in (Ga,Mn)As is supported by the *in-situ* ARPES studies which revealed a modified but unitary structure below the Fermi level for the $x = 1.6\%$ ferromagnetic sample.

3.1.3 Summary

All the experimental findings presented here (considering low and room temperature PR studies) converge into a cohesive picture of (Ga,Mn)As properties in the low Mn concentration limit. The LT-PR studies, with detailed analysis of the structural, electronic, magnetic properties, complement fully the picture of

the emergence of long-range ferromagnetic coupling in (Ga,Mn)As provided by the RT investigations (Chap. 3.1.1). For both sample series, one can identify the bordering Mn concentration x_b below which the Mn-related impurity states are revealed by the red shift of the absorption edge in the FKO-dominated RT-PR spectra, and below the band-gap feature unveiled in LT-PR. The corresponding scenarios are shown in Figs. 3.6(b) and 3.13(b), respectively. However, due to the applied LT-PR, it was possible to resolve the spectral features and deduce that Mn states are partly detached from the valence band, but still, hybridise with them. Most of the features observed in the layers with $x \leqslant x_b$ are very similar (if not identical) to those observed in the reference LT-GaAs layers. This is the case of the HR-XRD, the micro-Raman spectroscopy, and the SQUID magnetometry.

For $x \geqslant x_b$, the increase in the Mn incorporation into GaAs results in a remarkable transition of the magnetic properties from a weak paramagnet through the inhomogeneous superparamagnetic-like ferromagnet, up to the homogeneous long-range itinerant ferromagnetic material which complemented the RT-PR studies. The research presented here points out that there exists a kind of a threshold value of p/x ratio, or a maximum compensation level above which neither the global nor the mesoscopic ferromagnetic coupling develops in DFS. This can be seen in the $x = 0.8\%$ (RT) and $x = 0.3\%$ (LT) layers. The Raman studies prove that they are p-type. However, its hole concentration is so small that it does not manifest any signs of a ferromagnetic coupling. This fact implies that the Mn-induced modification of the GaAs valence band observed by the PR occurs for x much lower than required to establish the ferromagnetic coupling. Furthermore, and perhaps most importantly, the combined magnetic characterisation and PR studies presented here clearly indicate that the paramagnetic $\longleftrightarrow$ ferromagnetic transformation in the carrier-mediated (Ga,Mn)As takes place without any changes of the valence band character. The valence

band is modified when the hole plasma fills its top states. In the RT-PR studies, the modification of the valence band is exposed by the blue shift of the optical energy gap transition after crossing x_b. In the case of LT-PR studies, a very slight blue shift as well as the broadening and splitting of valence subband features are observed. Those findings are connected with the band filling effect. Nevertheless, the observation of the Burstein-Moss shift of the optical gap with the increasing x is limited by the gap narrowing due to the many-body interactions.

3.2 Annealing effects on (Ga,Mn)As

The post-growth annealing of (Ga,Mn)As layers is a procedure enabling to obtain the highest T_C of ferromagnetic samples. The mechanism lies in out-diffusion of weakly bound Mn interstitials, Mn_I, from the layer introduced by the low-temperature growth conditions. Mn_I is a double donor defect compensating Mn_{Ga} acceptors in the (Ga,Mn)As layers and therefore it decreases the hole density. Furthermore, Mn_I can interact with substitutional Mn antiferromagnetically and accordingly it reduces the number of magnetic moments participating in long-range ferromagnetism. Both mechanisms affect T_C of (Ga,Mn)As epitaxial layers. Owing to the fact that the annealing treatment can increase the hole density of the layer, it may also affect the Fermi level position, and thus, the energy of the optical gap. In this section the studies of annealing-induced changes of the optical gap in (Ga,Mn)As epitaxial layers probed by the RT-PR spectroscopy are presented.

3.2.1 Structural, electronic, and magnetic properties

The annealing treatment has to be performed below the optimal epitaxial growth temperature to prevent the formation of MnAs precipitates in the layer. The out-diffusion can be more effective by applying an additional capping layer

on top of an epitaxial (Ga,Mn)As before the annealing. The cap traps out-diffused Mn_I, and therefore T_C can be enhanced, compared to the uncapped layer. The arsenic capping layer is usually used since it reacts with Mn_I by creating the MnAs compound on the surface [145]. As an alternative to arsenic, amorphous Sb cap is used due to a more controllable deposition process and isoelectronic character in GaAs [146].

In this study, 100 nm thick (Ga,Mn)As layers with 6% Mn content were investigated. They were grown using the LT-MBE technique at a temperature of approximately 230°C on the semi-insulating (001)-oriented GaAs substrates. After the growth, one sample was covered *in-situ* in the MBE chamber with ten monolayers of amorphous Sb. Those samples are labelled (Ga,Mn)As/Sb. The obtained (Ga,Mn)As and (Ga,Mn)As/Sb layers were also cleaved and then annealed to get a series of samples with/without cap and also annealed/as-grown. The low-temperature annealing treatment was performed in air at 180°C for 60 h.

Additionally, two undoped LT-GaAs layers were used as a reference. Their thicknesses are 230 and 800 nm. They were grown on GaAs under the same conditions as (Ga,Mn)As. Both the Mn content and the layer thicknesses were verified during the epitaxial growth by the RHEED intensity oscillations [138].

The HR-XRD results for LT-GaAs and (Ga,Mn)As layers are shown in Fig. 3.14. Apparent X-ray interference fringes for the (004) Bragg reflections of all the layers evidence their good quality. The angular spacings of the fringes were used to calculate the layer thicknesses that correspond very well to their thicknesses determined from the growth parameters. All the epitaxial layers were grown pseudomorphically on the GaAs substrate under the compressive misfit strain which is demonstrated by the shift of the diffraction peaks to smaller angles as compared to the GaAs substrate. The increase of the lattice parameter (c) is caused mainly by As_{Ga} [137] in LT-GaAs, and additionally Mn_I defects. The results of HR-XRD analysis by means of the perpendicular

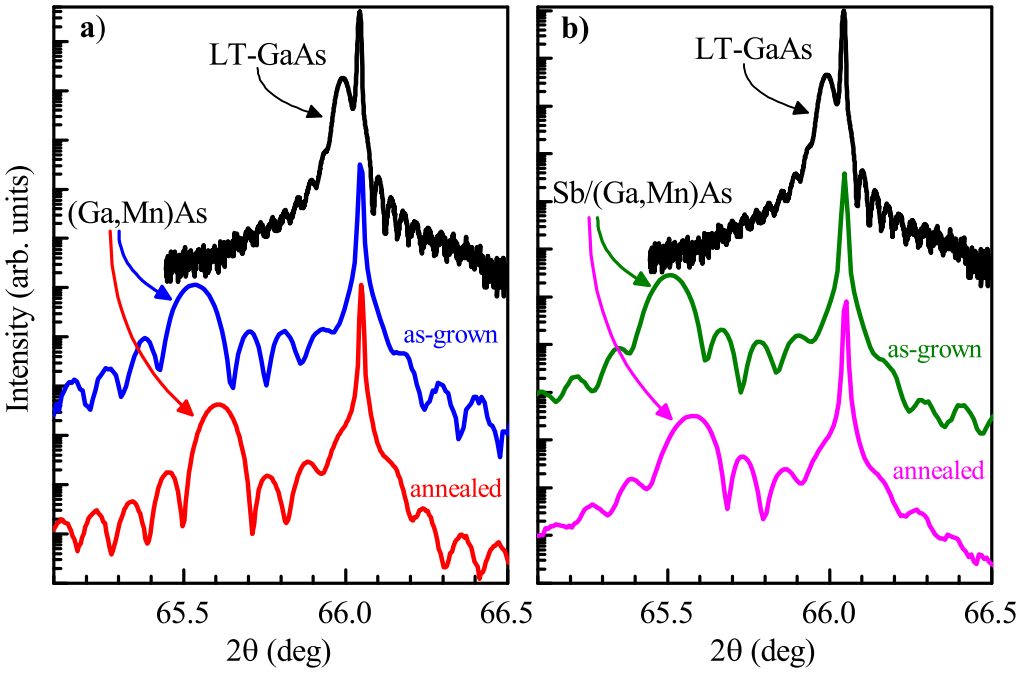

FIGURE 3.14: HR-XRD results: $2\theta/\omega$ scans for (004) Bragg reflections of Cu K_{α_1} for a) as-grown and annealed (Ga,Mn)As/GaAs ($x = 6\%$) heterostructures compared to the LT-GaAs/GaAs data. Picture b) shows similar situation but for (Ga,Mn)As layer covered with additional Sb cap (Sb/(Ga,Mn)As).The narrow features correspond to the reflection from the GaAs substrate, and the broader peaks marked with arrows are reflections from the epitaxial layers. The curves are vertically offset for clarity. Reproduced from [15], with the permission of AIP Publishing.

and relaxed lattice parameters, c and a_{rel} respectively, are listed in Tab. 3.4. As can be seen in Fig. 3.14 the angular positions of the diffraction peaks of (Ga,Mn)As and (Ga,Mn)As/Sb move to higher values after the annealing treatment, resulting in a decrease in the perpendicular lattice parameters. The observation is expected due to out-diffusion of Mn_I defects from the (Ga,Mn)As layers [147].

SQUID magnetometry results of the (Ga,Mn)As nad (Ga,Mn)As/Sb heterostructures are depicted in Fig. 3.15 and summarised in Tab. 3.4. The measurements were performed along the in-plane easy axis of magnetisation that is typical of compressively strained (Ga,Mn)As. The as-grown layers displayed

TABLE 3.4: The layer thicknesses and their lattice parameters, c and a_{rel}, calculated from the results of HR-XRD measurements performed at 27°C, Curie temperatures, T_C, obtained from the SQUID magnetometry measurements. The values of optical gap E_G and electro-optic energies $\hbar\theta$, obtained from the analysis of the FKOs periods of the modulation PR spectra for the investigated epitaxial layers of LT-GaAs, (Ga,Mn)As and (Ga,Mn)As/Sb.

Layer	Thickness (nm)	c (Å)	a_{rel} (Å)	T_C (K)	E_G (eV)	$\hbar\theta$ (meV)	CPLM (cm^{-1})
LT-GaAs, as-grown	800	-	-	-	1.415	23.64	-
LT-GaAs, as-grown	230	5.65789	5.65563	-	1.413	40.61	-
(Ga,Mn)As, 6%, as-grown	100	5.6934	5.67294	40	1.408	53.95	268.01
(Ga,Mn)As, 6%, annealed	100	5.68773	5.67018	73	1.411	54.9	269.28
(Ga,Mn)As/Sb, 6%, as-grown	100	5.69543	5.67393	50	1.408	54.6	267.04
(Ga,Mn)As/Sb, 6%, annealed	100	5.69057	5.67156	115	1.419	44.9	267.29

the T_C values of 40 K and 50 K for the uncapped and capped layers, respectively. The higher T_C values obtained for the 6% (Ga,Mn)As layer (Fig. 3.15) with respect to the value for the (Ga,Mn)As/Sb suggest a somewhat higher x in the former layer, which is confirmed by a slightly larger value of the lattice parameter for that layer (Tab. 3.4). The difference in T_C values in as-grown films can be also a result of the air exposition of the samples. The Sb cap prevents the (Ga,Mn)As layer from oxygen diffusion into the layer that can lead to suppressing the magnetic moments of Mn^{2+}. The Curie temperature of (Ga,Mn)As layers increased after the annealing treatment. The process was more efficient for the capped (Ga,Mn)As/Sb layer giving T_C equal to 115 K. On the other hand, for the uncapped layer T_C it yielded 73 K after annealing. The low-temperature values of magnetisations differ significantly (by about a factor of 2) comparing the as-grown and annealed samples. This indicates that the

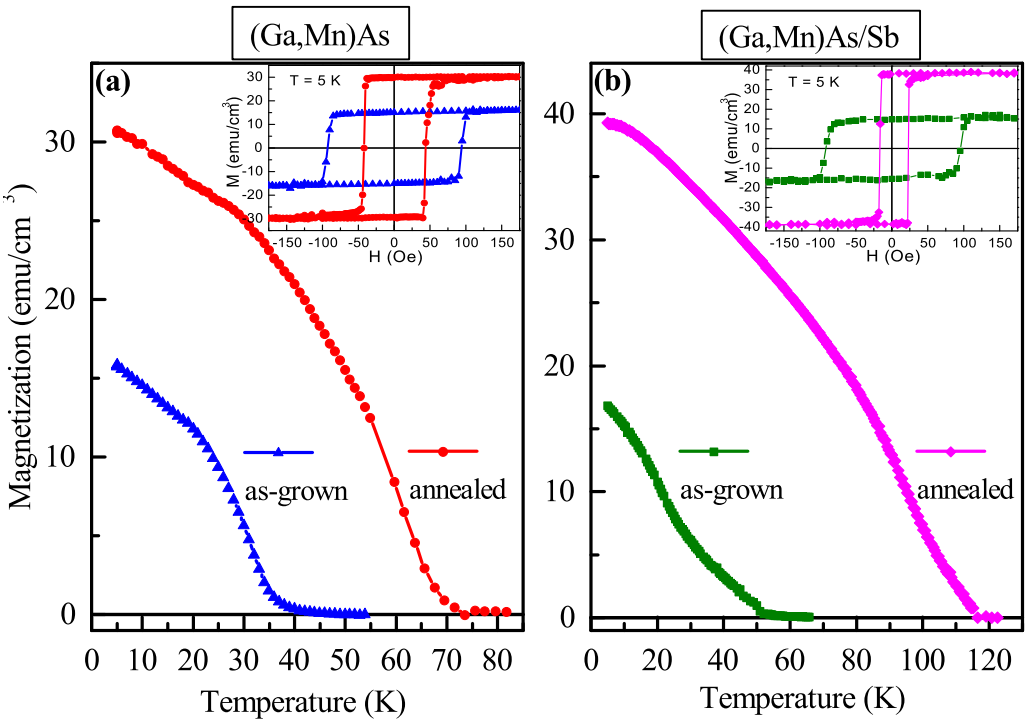

FIGURE 3.15: Temperature-dependent magnetisation along the in-plane crystallographic direction for the as-grown and annealed (Ga,Mn)As (a) and Sb-capped (Ga,Mn)As (b). Instets show magnetisation hysteresis loops measured at a temperature of 5 K. Reproduced from [15], with the permission of AIP Publishing.

layers contain a large value of Mn_I defects neighbouring Mn substitutional ions. As it was pointed out in Chapter 1, the Mn^{2+} magnetic moment can be neutralised by the neighbouring Mn_I defect and thus suppressing the magnetisation magnitude. After the annealing treatment and the out-diffusion process more Mn_{2+} ions are able to contribute to the long range ferromagnetic coupling.

Furthermore, the annealing treatment resulted in a decrease in the coercive field of the (Ga,Mn)As layers connected with an increase in their saturation magnetisation at 5 K, as shown in the insets in Fig. 3.15. The coercive field of about 100 Oe in the two as-grown layers decreased, as a result of annealing, to 50 Oe in the uncapped 6% (Ga,Mn)As layer and even to 25 Oe in the case of Sb-capped (Ga,Mn)As one. This decrease in the coercive field strength results from an increase in the hole concentration in the annealed layers [148] and is successfully explained considering the valence band holes [149]. The magnetic

characteristics of (Ga,Mn)As/Sb sample infer that the high-T_C MnSb compound does not contribute to the ferromagnetic phase transition temperature. Small MnSb precipitates display T_C as high as about 600 K, exceeding even T_C=585 K for the bulk MnSb, as shown by Kochura et al. [150]. On the other hand, as can be deduced from the HR-XRD and SQUID results the Sb cap traps out-diffused Mn_I defects efficiently. Most possibly a MnSb compound is formed. However, it does not create a ferromagnetic layer but rather single superparamagnetic or paramagnetic particles.

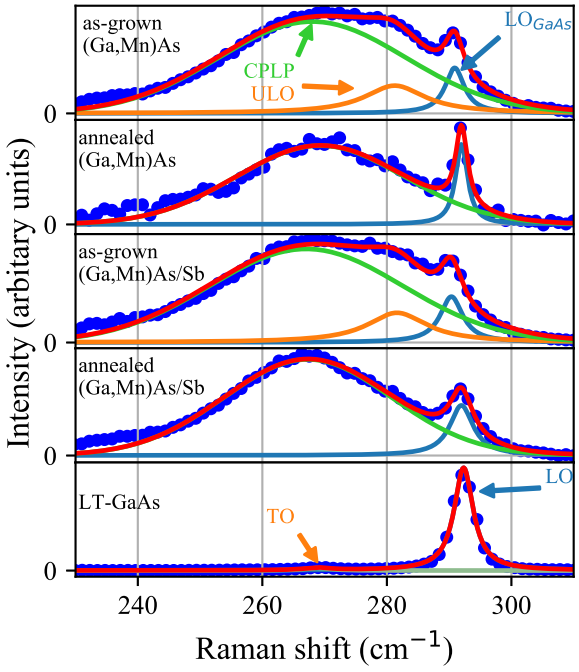

FIGURE 3.16: Raman spectra collected at RT in the backscattering configuration from the (001) surfaces of the as-grown and annealed (Ga,Mn)As and (Ga,Mn)As/Sb layers with x = 6%. The deconvolution of Mn-doped layers spectra shows developed CPLM features near the wavenumber of the TO phonon and also the LO phonon mode. The spectra of as-grown (Ga,Mn)As layers revealed a contribution of ULO (unscreened longitudinal optical phonon mode) that vanishes after the annealing treatment.

The Raman scattering spectroscopy spectra of the studied samples are depicted in Fig. 3.16. The spectra were taken using a 514 nm argon-ion laser at RT. In the vicinity of 292 cm^{-1}, and 267 cm^{-1} of LT-GaAs spectra, one can see

the LO and very weak TO phonon modes, respectively. The fits in Fig. 3.16 were done using the Lorentzian line shape for the LO, ULO, and TO phonons and the Gaussian function for CPLM features. In the spectra related to all Mn-doped layers, one can find the developed CPLM features. Additionally, for the as-grown layers the ULO feature emerges and then vanishes after annealing. The wavenumber position near the TO phonon and dominating character of the CPLM spectral feature suggest a high level of acceptor doping in (Ga,Mn)As [127]. However, the CPLM peak position shows that there is no expected red shift of the CPLM due to the annealing treatment as can be seen in Table 3.4. The red shift can be observed in the annealed samples where the CPLM of Sb-capped high-T_C layer moved to smaller wavenumbers compared to the uncapped counterpart. For the Sb-capped layer the most significant increase in T_C was observed as a result of annealing. It is worth noting that broadening of CPLM decreased after annealing. The Raman shift values for the CPLM peak correspond very well to 6-7% of Mn content samples in ref. [127] and indicate large hole density. However, due to the broadening of the CPLM feature and its overlapping with the LO peak, there was no possibility to fitting the ULO feature and obtaining the hole densities according to the method proposed by Seong et al. [127]. It was feasible only for the as-grown layers and giving 4.7×10^{19} cm^{-3}. Decreasing the intensity of ULO peak after annealing is also a symptom of increasing hole density after it. Additionally, according to Seong et al. [127] the Raman shift value of ULO for $x = 6\%$ is expected at 285 cm^{-1}. At the same time, the spectral deconvolution indicates that the Raman shift of LO features exceeds 290 cm^{-}1 in all layers. That substantiates the statement that the narrower peak in the spectra can not be assigned to ULO of p-type (Ga,Mn)As but rather an LO phonon feature from the GaAs substrate. However, the as-grown (Ga,Mn)As and (Ga,Mn)As/Sb samples revealed a red shift of LO phonons in reference to its wavenumber position in LT-GaAs. Moreover, annealing causes restoration of the Raman shift of this feature towards the GaAs

LO position. That observation may arise from the presumptive occurrence of ULO_R, and $CPLM_R$ features contributing to the spectra from the regions of samples with reduced hole densities which can not be spectrally resolved here. After the annealing, the ferromagnetic phase becomes more homogeneous across the volume of the layers. As a result, the ULO_R peak may decrease its intensity and together with $CPLM_R$ shifts towards smaller wavenumbers reducing the overlapping with the substrate LO peak. As was mentioned earlier in this paragraph, broadening of the CPLM feature decreases after the annealing in the present series of samples but overall it is doubtfully large. In particular, the theory of the CPLM, including a generalisation of the Drude theory and also the Lindhard-Mermin approach, does not predict such broadening for highly p-type doped semiconductor layers [125]. Thus the broadening magnitude may be somewhat connected with the change of both the hole density and the level of disorder, which plays a more important role in the case of heavily doped layers grown under the low-temperature conditions. One can also recall the Raman scattering spectroscopy results from the next chapter shown in Fig. 3.21. There the broadening of CPLM features is smaller for all the samples indicating that the $x = 4\%$ layers were grown under more optimised conditions than the present ones. Unfortunately, the current theories on CPLM do not consider the influence of disorder.

3.2.2 Photoreflectance studies

The PR measurements of LT-GaAs, (Ga,Mn)As and (Ga,Mn)As/Sb layers were performed at RT using an argon-ion pumping laser (514 nm). The PR spectra measured in the energy range from 1.35 to 1.65 eV are shown in Fig. 3.17 (a) and (b). All the experimental spectra revealed the electric-field-induced FKO [133] at the energies above the fundamental absorption edge, whose oscillations are marked with numbers as can be seen in Fig. 3.17. Moreover, the PR

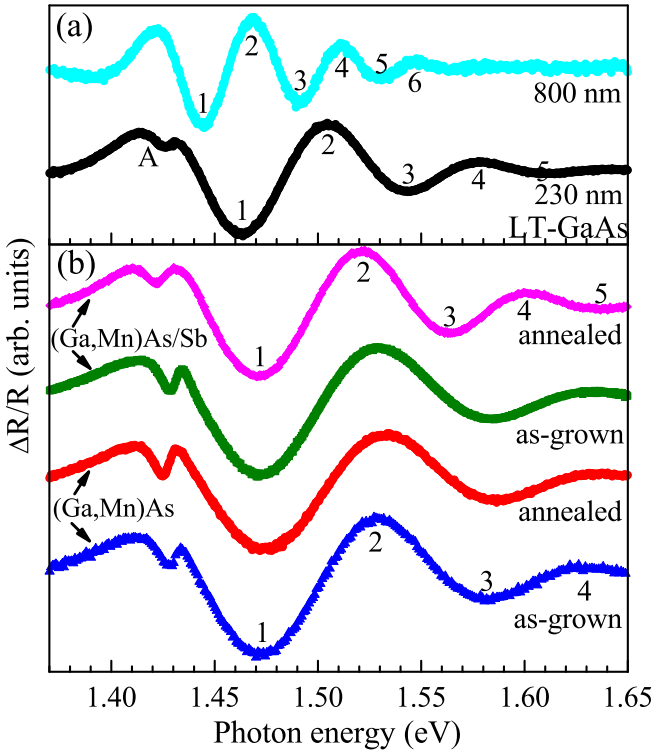

FIGURE 3.17: PR spectra for (a) two LT-GaAs reference layers of different thicknesses (written in the figure) and for (b) as-grown/annealed layers of (Ga,Mn)As and (Ga,Mn)As/Sb epitaxially grown on the GaAs substrate. Numbers mark the FKO extrema index. The letter "A" denotes a layer-substrate interface contribution to the spectrum. The spectra were normalised to the same intensity and vertically offset. Reproduced from [15], with the permission of AIP Publishing.

spectra for all the epitaxial layers, except 800-nm thick LT-GaAs, exhibit the layer-substrate interface related feature designated with capital "A" the Fig. 3.17 (a). The description of this feature was given earlier in the section about RT-PR in Chapter 3.1.1 (low-x layers). Previously it was studied by Sydor et al. [134]. The lack of the feature "A" in the PR spectrum for the 800-nm thick LT-GaAs layer confirms its heterostructure interface origin. The analysis of the optical gap was done using the simplified method described in Chapter 2.2 (Eq. 2.6), based on the analysis of energetic positions of FKO oscillations in the PR spectra. The results of this procedure are depicted in Fig. 3.18 and the obtained values of E_G and $\hbar\theta$ are listed in Tab. 3.4. For the two investigated LT-GaAs layers with different thicknesses, very similar E_G values but noticeably

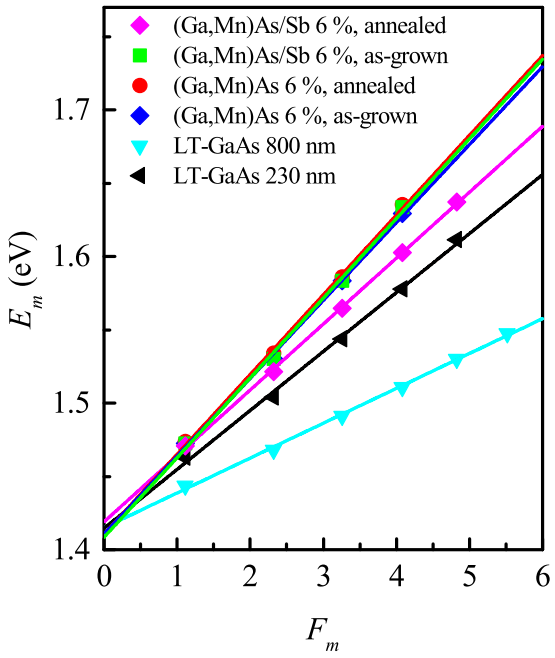

FIGURE 3.18: Linear dependencies of the FKO extrema energy as a function of the extrema index for the LT-GaAs reference layers and the as-grown and annealed (Ga,Mn)As and (Ga,Mn)As/Sb layers shown in figure 3.17. Solid lines represent the linear fits in accordance to Eq. 2.6. Reproduced from [15], with the permission of AIP Publishing.

different electro-optic energies $\hbar\theta$ were obtained, resulting from different slopes of the corresponding linear dependences shown in Fig. 3.18. The smaller value of $\hbar\theta$ revealed for the thicker LT-GaAs layer is seemingly caused by a much lower electric field in this layer. The energy of the optical gap for the reference LT-GaAs layers yielded 1.415 and 1.413 eV for 800 and 230 nm-thick layers, respectively. Both the as-grown (Ga,Mn)As and (Ga,Mn)As/Sb layers display very similar linear characteristics in Fig. 3.18 that translates to the same value of $E_G = 1.408$ eV, which is red-shifted as compared to the E_G value for the LT-GaAs layers. This result is in qualitative agreement with the previous PR analysis from Ref. [87]. The proposed interpretation assumes merging the Mn-related electronic states with the host GaAs valence band for large enough x. However, considering the Raman scattering results the red shift can be also

contributed by the band tailing due to disorder. The annealing treatment of the (Ga,Mn)As and (Ga,Mn)As/Sb layers caused a blue shift of the interband transition energy. However, the effect is distinctly stronger for the (Ga,Mn)As layer covered with the Sb cap as can be seen in Tab. 3.4. Considering that the annealing treatment causes an increase in the hole concentration in the layers, as inferred from the SQUID magnetometry and Raman scattering spectroscopy analysis, the blue shift is a result of the Fermi level position lowering due to valence band filling with itinerant holes. Namely, the blue shift of the interband transition in annealed samples is caused by the Burstein-Moss shift of the absorption edge [62]. According to this interpretation, a larger hole density in the annealed (Ga,Mn)As/Sb layer results in stronger blue shift of the optical gap. Nevertheless, the effect magnitude is supressed by the gap narrowing due to the hole plasma-related many-body interactions. These results are in agreement with the itinerant valence band character of holes [32, 35].

3.2.3 Summary

In this section the effect of out-diffusion of Mn_I defects from the (Ga,Mn)As epitaxial layers due to the annealing treatment on their band structure properties was studied by means of modulation PR spectroscopy. Structural, magnetic, and electronic properties of the layers were characterised with HR-XRD, SQUID magnetometry, and Raman scattering spectroscopy, respectively. The results of HR-XRD characterisation showed a decrease in the lattice parameter values of the (Ga,Mn)As layers after the annealing treatment, confirming the efficient out-diffusion of Mn_I defects toward the surface. The SQUID magnetometry measurements showed a significant increase in the T_C and saturation magnetisation at 5 K. On the other hand, the annealing-related decrease in the coercivity field of the hysteresis loops suggests an enhancement of the hole

density in the layers. The increase in T_C and also the decrease in the coercivity field were much more evident for the (Ga,Mn)As/Sb layer, reflecting the efficiency of the Sb cap in gathering of out-diffused Mn interstitials. Raman scattering spectroscopy revealed the broad hole plasma-related CPLM spectral features in the Mn-doped samples. The wavenumber of the main peak near the TO phonon position implies large hole density. However, the spectral shape does not change significantly with T_C of particular layers indicating an essential role of disorder in forming the wide CPLM structure. Nevertheless, the CPLM slight red shifts are observed after the annealing due to an increase in hole density. The most significant energy shift is found for the (Ga,Mn)As/Sb layer with the largest obtained T_C. The PR spectra of all the samples revealed FKO above the fundamental absorption edge energy. The band gap energy of as-grown (Ga,Mn)As and (Ga,Mn)As/Sb decreased compared to the energy gap value of the reference LT-GaAs. It is interpreted as build-up of Mn-related electronic states in the vicinity of the top of GaAs valence band for relatively high x resulting in narrowing of the optical gap. Nevertheless, the band gap transition energy increased due to the annealing treatment interpreted as the Burstein-Moss shift of the absorption edge. It infers that the Fermi level location lies within the disordered valence band, and its energy is determined by the free-hole concentration.

3.3 Quaternary DMS (Ga,Mn)(Bi,As)

In this chapter the results of studies on the new DMS (Ga,Mn)(Bi,As) are presented. The main purpose of such a compound growth was an idea of combining the properties of Ga(Bi,As) and magnetic semiconductor (Ga,Mn)As.

The Ga(Bi,As) semiconductor is a highly mismatched alloy (HMA) studied from the perspective of fundamental properties as well as applications. One of the essential properties of HMA is having nonlinear characteristics of the

band gap with an increasing fraction of a dopant as it was observed in nitrogen-doped GaAs [151]. Bi is an isoelectronic dopant in the case of As substitution in the GaAs matrix. Its small amount induces reduction of the band gap by about 80 meV for 1% of the Bi content [85, 152] (for comparison 1% of In content gives about 15 meV red shift in the (In,Ga)As compound). This gap shrinking was explained by the valence band anti-crossing (VBAC) model [85, 153]. Thus, bismuth-based semiconductors are an excellent testing ground for the band structure engineering for photonic or photovoltaic applications. The obtained energy range due to Bi doping of III-V semiconductors covers the infrared region of the optical spectrum making this material competitive for quaternary GaInAsP or AlGaInAs grown on InP used in lasers for telecommunication (1.53 μ m to 1.57 μ m). Indeed, it is desirable to use the GaAs substrates for laser heterostructures [154]. Apart from the band gap reduction, there was also observed a significant increase in the split-off energy (E_{SO}, SO) in the valence band. For the Bi content, about 10% and higher, the energy gap becomes smaller than E_{SO}. It is believed that this property of Ga(Bi,As) can lead to a boost of the efficiency of bismuth-based near-infrared optoelectronic devices by suppressing one of the Auger recombination processes whereby a hole recombines non-radiatively with an electron excited from the spin-orbit split-off (SO) band [154]. The spin-orbit bowing induced by Bi atoms in GaAs is also in the interest of spintronics. The spin-orbit interaction is one of the essential factors considering spin relaxation in the semiconductor structures. It defines the spin-splitting of a band structure. Tuning of the SO-related band with the Bi dopant may allow developing some new non-magnetic spin-devices based on an enhancement of the Rashba and/or Dresselhaus effects working without the external magnetic field [155, 156]. Furthermore, it can contribute to improving semiconductor structures that utilise the spin Hall effect [155].

Building on the above, the new compounds combining properties of (Ga,Mn)As and Ga(Bi,As) - (Ga,Mn)(Bi,As) were studied. It can be further exploited for

the spin-orbit engineering in DMS. However, in this thesis an emphasis is put on the controversial issue of Fermi level in (Ga,Mn)As.

In this section, the impact of Bi incorporation into the epitaxial (Ga,Mn)As layers on their band-structure, electronic, magnetic and structural properties is studied. Thus the 100-nm thick (Ga,Mn)As and (Ga,Mn)(Bi,As) layers with Mn and Bi contents of 4% and 0.3%, respectively in the Bi-codoped samples were used. Besides, the 150-nm thick Ga(Bi,As) also with the 0.3% Bi content and 230-nm thick undoped GaAs layer for reference were studied. The layers were grown by LT-MBE on the semi-insulating (001)-oriented GaAs substrates at a temperature of approximately 230°C . The growth parameters were monitored by the RHEED. The composition of the layers, particularly the Bi content, was confirmed using *ex-situ* Rutherford Backscattering Spectrometry (RBS). The wafers with the epitaxial layers of (Ga,Mn)As and (Ga,Mn)(Bi,As) were cleaved, and then the parts of each wafer were annealed in air at 180°C for 80 h.

3.3.1 Structural properties

The HR-XRD measurements demonstrate that all the epitaxial layers were grown coherently on the GaAs substrate at the compressive strain. The clear X-ray interference fringes revealed for the (004) Bragg reflections of all the layers, as shown in Fig. 3.19, infer high structural perfection of the films. The diffraction peaks corresponding to the all as-grown layers shown in Fig. 3.19 shift to smaller angles owing to the larger perpendicular lattice parameters as compared to GaAs. Furthermore, the perpendicular lattice parameters in the Ga(Bi,As), (Ga,Mn)As, and (Ga,Mn)(Bi,As) layers, become larger than LT-GaAs as a result of additional incorporation of the Bi, As_{Ga}, and Mn_I in the crystal lattices.

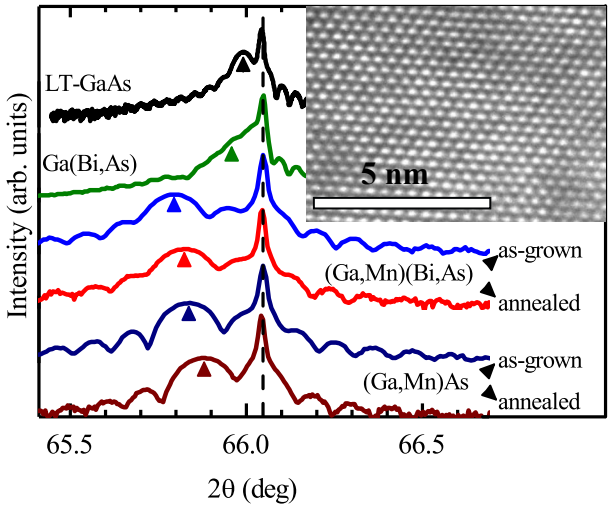

FIGURE 3.19: $2\theta/\omega$ scans for (004) Bragg reflections for the as-grown LT-GaAs and Ga(Bi,As) layers and the as-grown and annealed (Ga,Mn)(Bi,As) and (Ga,Mn)As layers epitaxially grown on the (001) semi-insulating GaAs substrate. The vertical line indicate the reflection from the GaAs substrate. The broader peaks at lower angles, marked by the arrows, are the reflections from the epitaxial layers. The scans are vertically offset for clarity. The inset shows high-resolution transmission electron microscopy (TEM) cross-sectional image of the as-grown (Ga,Mn)(Bi,As) epitaxial layer. Reproduced from [16], with the permission of AIP Publishing.

As a result of the annealing treatment the angular positions of the diffraction peaks, corresponding to the epitaxial layers, shift to higher values. That is caused by a decrease in the misfit strain in the layers and their perpendicular lattice parameter, mainly due to the Mn_I out-diffusion [157](see chapter 3.2). Angular positions of the diffraction peaks in the $2\theta - \omega$ scans corresponding to the epitaxial layers were used to calculate the perpendicular lattice parameters (c) and the relaxed lattice parameters (a_{rel}), on the assumption that the elasticity constants are the same as for GaAs. They are listed in Tab. 3.5. Additionally to the lattice parameters, the values of in-plane misfit strain in the layers (lattice mismatch) are also included. The Bi content in the relevant layers was confirmed by the Rutherford Backscattering Spectrometry (not discussed in this thesis). The high-resolution transmission electron microscopy

TABLE 3.5: The in-plain misfit strain values, calculated from the results of HR-XRD measurements, the T_C values, revealed from the SQUID magnetometry measurements, and the E_0 transition energies and the electro-optic energies $\hbar\theta_{lh}$ and $\hbar\theta_{hh}$, obtained from the full-line-shape analysis of the PR spectra for the investigated epitaxial layers.

Layer	In-plane strain $\times 10^4$	T_C (K)	E_0 (eV)	$\hbar\theta_{lh}$ (meV)	$\hbar\theta_{hh}$ (meV)
LT-GaAs, (as-grown)	1.5	-	1.427	45.11	36.78
Ga(Bi,As) (as-grown)	3.3	-	1.402	44.3	33.09
(Ga,Mn)(Bi,As) (as-grown)	16.9	50	1.416	44.58	33.96
(Ga,Mn)(Bi,As) (annealed)	14.4	60	1.42	46.93	28.94
(Ga,Mn)As (as-grown)	14.2	57	1.428	28.27	23.59
(Ga,Mn)As (annealed)	10.8	70	1.434	37.85	27.64

(HR-TEM) cross-sectional image of the (Ga,Mn)(Bi,As) layer, confirming the high structural perfection, is presented in the inset of Fig. 3.19.

To sum up, it was possible to grow homogeneous (Ga,Mn)(Bi,As) epitaxial layers and characterise them by X-ray diffractometry and transmission electron microscopy. The measurements showed the high structural quality of the obtained films and allowed to calculate their lattice parameters. The low-temperature annealing treatment of (Ga,Mn)(Bi,As), similarly to (Ga,Mn)As, leads to the decrease in the compressive strain in the layers by out-diffusion of mobile Mn_I defects.

3.3.2 Magnetic and electronic characterisation

The results of SQUID magnetometry of magnetically doped layers (as-grown and annealed) are presented in Fig. 3.20. The magnetisation vs the magnetic field dependences shown in the insets in Fig. 3.20 present nearly rectangular

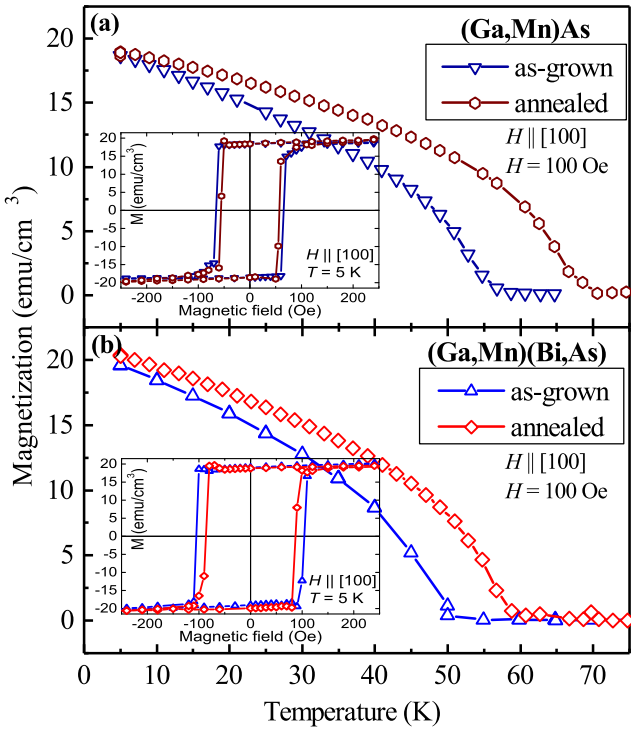

FIGURE 3.20: Temperature-dependent magnetisation along the in-plane [100] crystallographic direction for the as-grown and annealed (Ga,Mn)As (a) and (Ga,Mn)(Bi,As) (b) layers after subtraction of diamagnetic contribution from the GaAs substrate. The insets show the magnetisation hysteresis loops measured at a temperature of 5 K. Reproduced from [16], with the permission of AIP Publishing.

hysteresis loops at the temperature 5 K. The results evidence that all Mn-doped layers display an easy magnetisation axis along the in-plane [100] cubic direction. Such a behaviour is expected for the (Ga,Mn)As layers grown on the GaAs substrate at the compressive misfit strain [158, 159]. As shown in Fig. 3.20, the as-grown (Ga,Mn)As and (Ga,Mn)(Bi,As) layers displayed the T_C values of 57 K and 50 K, respectively. That indicates that incorporation of Bi into the (Ga,Mn)As layer results in the decreasing Curie temperature. As expected, out-diffusion of Mn_I defects from the layers volume due to the annealing treatment rises the T_C in both layers. This increase in T_C appears with a distinct decrease in the coercive field strength caused by the annealing, as can be deduced from the hysteresis loops shown in the insets in Fig. 3.20. This coercivity decrease comes mainly from the increase in the hole density in the

annealed layers [148, 149]. The values of T_C for all magnetically doped layers are listed in Tab. 3.5. The values of magnetisation in $M(T)$ curves at the lowest temperature ($T = 5$ K) are quite the same for (Ga,Mn)As and (Ga,Mn)(Bi,As) including the as-grown and annealed samples. Two things can be deduced from this observation. Firstly, in the case of as-grown (Ga,Mn)As there is a small number of Mn_{Ga} - Mn_I coupled defects. For the (Ga,Mn)As layers with a large concentration of Mn_{Ga} and Mn_I (like in the case of the layers analysed in Chapter 3.2), after the annealing treatment the low-T magnetisation value increases due to out-diffusion of Mn_I leaving an unpaired spins of Mn^{2+} ions and releasing free holes. Secondly, Bi co-doping of (Ga,Mn)As did not change significantly the shape of $M(T)$ curves as well as the LT magnetisation values, either this result is rather connected with the lack of mechanisms responsible for vanishing of the magnetic moments and/or occurring of bismuth-based second phases in the samples (for instance ferromagnetic BiMn) [160]. In conclusion, bismuth doping in (Ga,Mn)As caused a small decrease in T_C in comparison to the (Ga,Mn)As layer. The reason for that can be an increase in the lattice constant due to Bi doping and thus increase in the Mn_{Ga}-Mn_{Ga} distances influencing their indirect ferromagnetic interactions. The $M(H)$ loops, as expected, revealed a decrease of the coercivity after the annealing due to the increase in the hole density.

The Raman scattering spectra for all the investigated layers are depicted in Fig. 3.21. The reference LT-GaAs spectrum revealed the LO and TO phonon modes fitted with two Lorentzian functions. Additionally, the Mn-doped layers revealed the hole plasma related CPLM feature near the Raman shift value of TO phonon mode in the reference spectra. These features were fitted using the Gaussian lineshape. Additionally, one can see the unscreened LO phonon mode feature (ULO) fitted also with the Lorentzian. The wavenumber position of the CPLM and ULO features indicates a relatively high hole density for all the Mn doped layers. As expected, 0.3% of Bi in GaAs is not enough to affect significantly the Raman spectra as compared to LT-GaAs results.

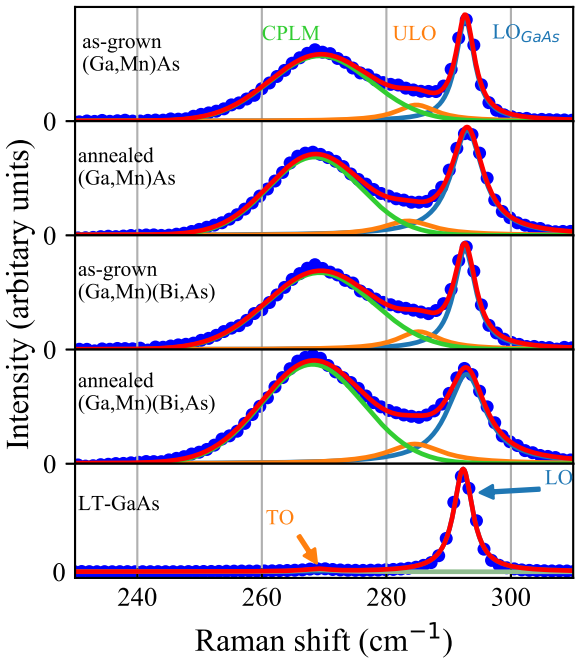

FIGURE 3.21: Raman spectra of the as-grown LT-GaAs and Ga(Bi,As) layers and the as-grown and annealed (Ga,Mn)(Bi,As) and (Ga,Mn)As layers recorded at RT in the backscattering configuration from the (001)-oriented surfaces. The spectra revealed the LO phonon mode from the substrate, (LO_{GaAs}), ULO (unscreened LO mode), and the hole plasma related CPLM feature. The spectra are vertically offset for clarity. The arrows indicate the positions of the Raman LO- and TO-phonon lines for the reference LT-GaAs layer.

Raman scattering did not reveal any significant differences in the hole plasma related mode due to Bi co-doping or annealing. However, as a result of the annealing treatment, the CPLM and ULO reveal a small red shift (for (Ga,Mn)As as well as (Ga,Mn)(Bi,As)) which is in qualitative agreement with the conclusions from the SQUID magnetometry results (increase in T_C) - similarly to the layers with $x = 6\%$ studied in Chapter 3.2. No damping or blue shifting of the CPLM feature can be seen due to doping with Bi atoms which may be a result of the decreasing hole density due to additional defects generation (as it was observed, for instance, in the acceptor co-doped (Ga,Mn,Be)As [161]) or even existence of a second phase at the expense of Mn_{Ga} acceptors. The analysis of the spectra with the method by Seong et al. [127] revealed that the hole density

is $\approx 0.5 \times 10^{19}\text{cm}^{-3}$ and it is underestimated for all the samples. The analysis did not reveal any significant differences in the hole concentration resulting from Bi co-doping or annealing. The comparison of SQUID results for the as-grown and annealed samples showed a relatively low level of Mn_I defects number, and therefore, the annealing is not very effective in increasing of the T_C. On the other hand, the CPLM broadening decrease after the annealing may suggest some improvement of the crystal ordering. Similar behaviour was observed in the $x = 6\%$ layers and discussed in Chapter 3.2.

3.3.3 Photoreflectance spectroscopy

The normalised PR spectra, measured with a 442 nm He-Cd laser pumping line are displayed in Fig. 3.22. All the experimental spectra contain the electric-field-induced FKOs above the fundamental absorption edge energy (Fig. 3.22). Moreover, the PR spectra for (Ga,Mn)As and (Ga,Mn)(Bi,As) exhibit an additional sharp feature interpreted as a contribution to the PR signal from the layer-substrate interface region (similarly to that in Fig. 3.17 in Chapter 3.2 and Ref. [87]). The full-line-shape fit of the experimental PR spectra was performed using the complex Airy (equation 2.4) and TDLS (equation 2.2) functions. The solid lines in Fig. 3.22 represent the fits. The best-fit parameters of the E_0 transition energies, $\hbar\theta_\text{lh}$ and $\hbar\theta_\text{hh}$ -the electro-optic energies for the LH and HH, respectively, are listed in Tab. 3.5. The obtained band gap energies are also marked with arrows in Fig. 3.22. The results evidence clear differences in the energy band structures of the investigated layers near the centre of the Brillouin zone. The significant red shift of E_0 optical transition in the Ga(Bi,As) layer of about 25 meV, with respect to that in the LT-GaAs one, is in good agreement with the previous PR results and the VBAC model [153]. Consequently, the Bi-codoped layers display distinctly lower values of the optical gap transition energies than the (Ga,Mn)As layers due to the Bi-induced VBAC mechanism.

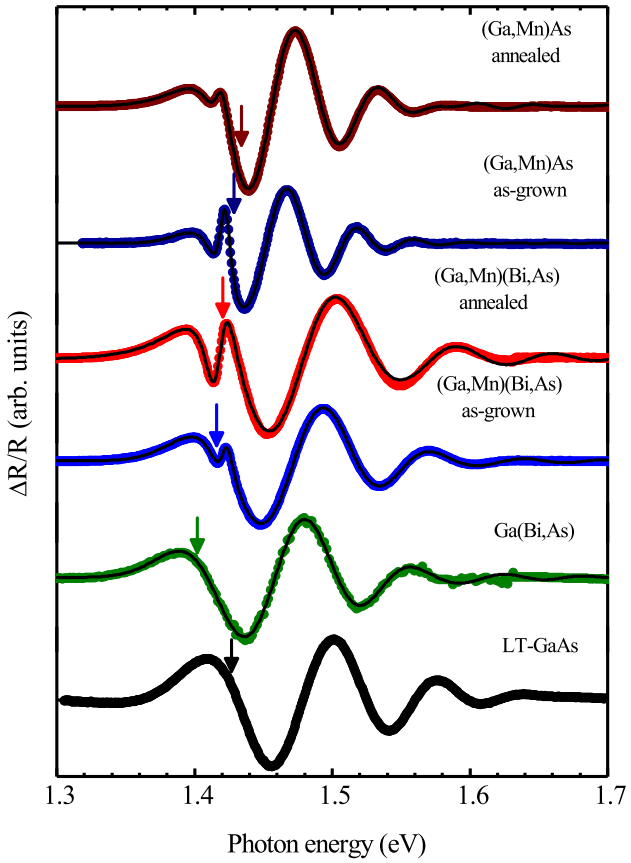

FIGURE 3.22: RT-PR spectra of the as-grown LT-GaAs and Ga(Bi,As) layers and the as-grown and annealed (Ga,Mn)(Bi,As) and (Ga,Mn)As layers (dots). Solid line indicate fits using the full-line-shape analysis with complex Airy functions (eq. 2.4) The spectra were normalised to the same intensity and vertically offset. The vertical arrows indicate the values of the E_0 transition energies for each layer obtained from the fit.Reproduced from [16], with the permission of AIP Publishing.

On the other hand, the (Ga,Mn)As and (Ga,Mn)(Bi,As) layers, with a hole concentration of over 10^{20}cm^{-3}, display larger values of E_0 transition energy than the LT-GaAs and Ga(Bi,As) films, respectively. This result is inconsistent with the seemingly similar situation in Chapter 3.2 where E_G increases after Mn doping. However, from the comparison of SQUID magnetometry and Raman scattering spectroscopy results of the two sets of samples it is possible to deduce that here the disorder-related narrowing may be reduced. The results of E_0 optical transition indicate that the shift of the absorption edge is due to the

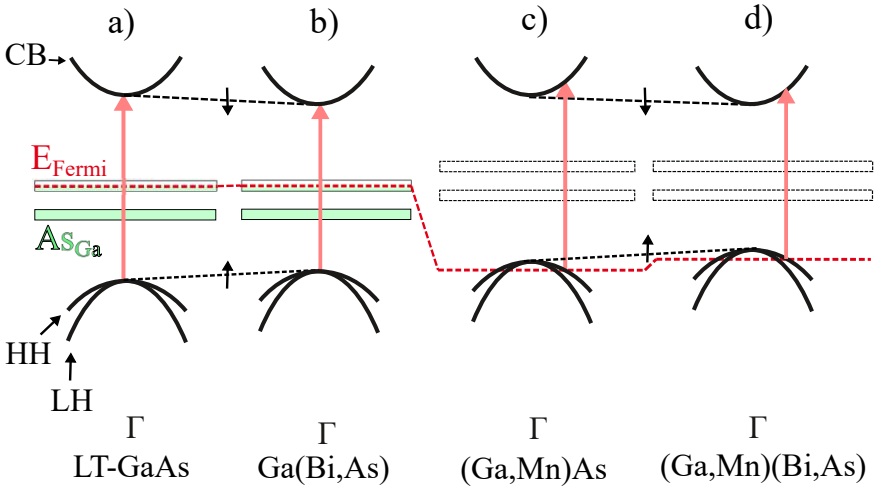

FIGURE 3.23: The schemes of the band structure in the vicinity of Γ point of the Brillouin zone for a) LT-GaAs, b) Ga(Bi,As), c) (Ga,Mn)As and d) (Ga,Mn)(Bi,As)

Burstein-Moss effect associated with the Fermi level location within the valence band and is dependent on the free-hole concentration [62, 88]. As regards the optical gap, E_0, the value of the Burstein-Moss shift calculated assuming the effective mass model for GaAs with the hole concentration of 10^{20}cm^{-3}, is about 150 meV [88]. This value is grater than the changes in the actual E_0 transition energies obtained from the PR measurements. This is interpreted as an effect of the band-gap renormalisation due to the many-body effect arising from the hole-hole Coulomb interactions in the valence band [144]. Secondly, the band gap in (Ga,Mn)As may be reduced as a result of mixing the Mn-related electronic states with the host GaAs valence band and establishing a disordered top of the valence band that expands into the band gap [80]. In the case of the Bi co-doped (Ga,Mn)As layers, such a disordered valence band is influenced by the valence band anticrossing interactions, leading to the band gap reduction according to the VBAC model [85]. This interpretation is in line with the revealed increase in the E_0 transition energies by about 5 meV after the annealing. This is caused by a further downward shift of the Fermi level into the valence band, owing to the increased hole density (observed also in Chapter 3.2).

3.3.4 Summary

In conclusion, the (Ga,Mn)(Bi,As) epitaxial layers were investigated employing structural, magnetic and optical characterisation methods. Also, the samples subjected to *ex-situ* annealing were studied. HR-XRD revealed high structural quality of the obtained layers allowing to calculate their lattice parameters. The layer quality was confirmed by HR-TEM. The Bi content in (Ga,Mn)(Bi,As) and Ga(Bi,As) was measured by RBS. The SQUID characterisation revealed a decrease in T_C due to Bi doping in comparison to the (Ga,Mn)As layer. As expected, the annealing treatment increased T_C and led to a decrease in coercivity in the $M(H)$ loops. The Raman spectra of all Mn-doped layers revealed the CPLM in the vicinity of TO phonon wavenumber. This indicates a high carrier density of the layers without damaging of Bi doping effect. Annealing caused a red shift of the CPLM feature and a decrease in its broadening sugesting an increase of hole density and improvement of structure, respectively. The PR spectra of all the layers revealed FKOs. The obtained energy of the optical gap of Ga(Bi,As) in reference to LT-GaAs, showed a red shift attributed to the VBAC mechanism reducing the band gap in the Bi-doped layers. Consequently, the optical gap values obtained for (Ga,Mn)(Bi,As) have lower energies than for (Ga,Mn)As. The optical gap of (Ga,Mn)As is blue shifted comparing to LT-GaAs. Similarly, (Ga,Mn)(Bi,As) layers are blue shifted compared to Ga(Bi,As). The blue shift is interpreted as the Burstein-Moss shift involving the valence band filling with holes. Annealing of the ferromagnetic samples revealed further small blue shifts for (Ga,Mn)As as well as (Ga,Mn)(Bi,As) related to the increase in the free hole concentration and the enhanced Burstein-Moss effect confirmed by the Raman spectroscopy results and change in coercivity shown in the SQUID measurements. To sum up, the PR results are consistent with the valence-band origin of itinerant holes that mediate ferromagnetic coupling, in both (Ga,Mn)As and (Ga,Mn)(Bi,As), in accordance with the $p-d$

Zener model for ferromagnetic semiconductors.

3.4 E_1 and $E_1+\Delta_1$ optical transitions in (Ga,Mn)As

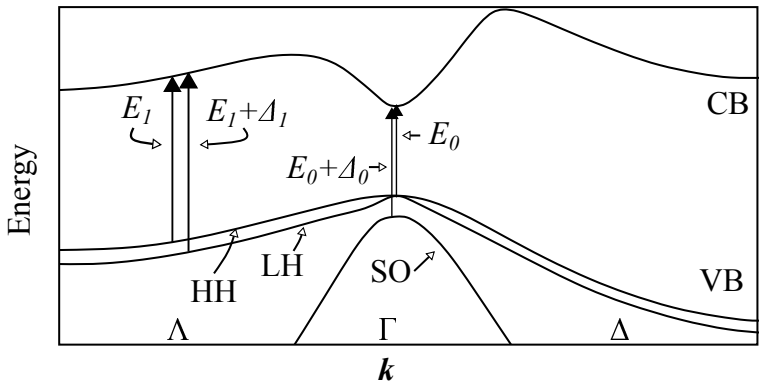

FIGURE 3.24: The band structure of GaAs obtained by the tight binding method with marked optical transitions. The E_1 and $E_1+\Delta_1$ transitions can be seen in the vicinity of Λ direction of the Brillouin zone.

E_1 and $E_1+\Delta_1$ are the inter-band optical transitions in the vicinity of Λ direction of the Brillouin zone in GaAs depicted in Fig. 3.24. The motivation of analysis of those critical points is mainly a large k distance from the centre of the Brillouin zone where the band edges can be strongly affected by the Fermi level position, like the band filling effect and many-body interactions arising from the existence of hole plasma [144]. Therefore, the observation of the E_1 and $E_1+\Delta_1$ transitions can give an additional insight into the influence of Mn doping on the GaAs band structure. In the case of (Ga,Mn)As the published results of SE measurements in the vicinity of E_1 and $E_1+\Delta_1$ optical transitions in the (Ga,Mn)As layers provided ambiguous conclusions. In particular, Burch et al. [75] reported on the ellipsometric investigations of (Ga,Mn)As layers. The authors prove that the peak corresponding to the E_1 interband transition in the imaginary part of the dielectric function spectra moves to higher energies with the increasing Mn content. The authors explained these results in terms of the second-order perturbation theory Hamiltonian where the Mn impurity band-related sp-d hybridisation potential term is responsible for repulsion of s and p

states of GaAs valence band by the Mn *d* states. Due to the directional character of this term, the most significant effect would be seen in the [111] direction of the Brillouin zone, i.e. feasible by probing E_1 and $E_1 + \Delta_1$. Contrary to those results, Kang et al. [90] found a small red shift of the E_1 transition and a constant $E_1 + \Delta_1$ energy with the increasing Mn content. Furthermore, some contradictory results were obtained by LT-SE [91] and MCD [162] supporting the impurity band model.

To resolve those issues, the epitaxial (Ga,Mn)As/GaAs heterostructures were studied by means of spectroscopic, structural and magnetic characterisation methods.

3.4.1 Structural and magnetic properties

For the purpose of those studies two series of samples were used. The first with the Mn content of ranging from 1% to 6% and thicknesses from 230 nm (x = 6%) to 300 nm. The other set is composed of 20 nm and 100-nm-thick layers, both with 6% of the Mn content. For those two sets of samples the reference 230-nm thick LT-GaAs layer was used. The layers were grown by LT-MBE on the semi-insulating (001) GaAs substrates at a temperature of approximately 230°C. The layer thicknesses and the Mn contents were controlled during the growth by the RHEED oscillatory amplitude analysis. In order to improve the structural quality, optical response and increase in their T_C, the two layers of 20 nm and 100 nm thicknesses (x = 6%), were annealed for 6 h and 60 h, respectively. The annealing treatment was performed in the air at a temperature of 180°C. The as-grown layers with x = 1%, 2%, 4%, and 6% and LT-GaAs were characterised in Ref. [87] employing Raman scattering spectroscopy, HR-XRD, SQUID, and RT-PR spectroscopy at the E_0 critical point.

The crystalline quality of the (Ga,Mn)As epitaxial layers was analysed using the high-resolution TEM. In particular, the as-grown 300-nm thick layer with x

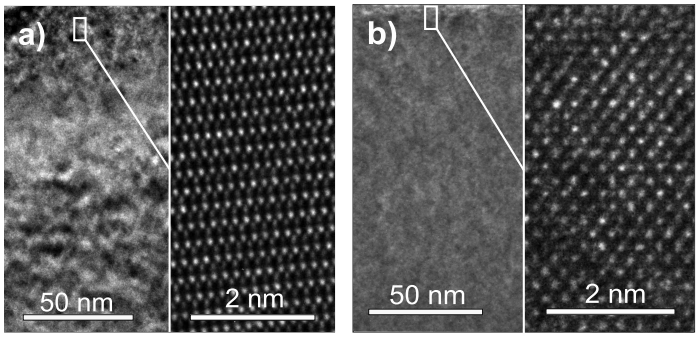

FIGURE 3.25: Cross-sectional TEM images of (a) the 300-nm-thick as-grown (Ga,Mn)As layer and (b) the 100-nm-thick (Ga,Mn)As layer annealed at 180°C for 60 h, both with $x = 6\%$. The right-hand side of the figures present the high-resolution magnification of the near-surface parts of the layers. The surface is located at the top of the low-resolution image. Reproduced from [17], with the permission of AIP Publishing.

= 4% (analysed also in Ref. [87]) and the annealed 100 nm thick sample with x = 6% revealed that the structure of the as-grown (Ga,Mn)As layer is disturbed compared to the annealed one as follows Fig. 3.25. However, the HR-XRD results for the 230 and 300-nm-thick layers with x from 0% to 6%, showed a good structural quality of the layers which were grown pseudomorphically on the GaAs substrate at the compressive misfit strain as shown in Ref. [87].

Examination of the magnetic properties with SQUID magnetometry revealed ferromagnetic ordering at LT in all the (Ga,Mn)As layers. The as-grown (Ga,Mn)As layers displayed the T_C values in the range from 25 K to 60 K for the Mn contents of 1%-6 %, respectively, as shown in Ref. [87]. The (Ga,Mn)As layers with $x = 6\%$ subjected to the post-growth annealing displayed a distinctly higher T_C of 73 K and 145 K for the 100 nm and 20-nm-thick layers, respectively, as concluded from the temperature-dependent magnetisation results shown in Fig. 3.26. Moreover, the 20-nm thick layer reaches a larger value of the low-temperature magnetisation showing that despite the same Mn content, a larger amount of Mn contributes to the long-range ferromagnetic phase than in the 100-nm thick layer.

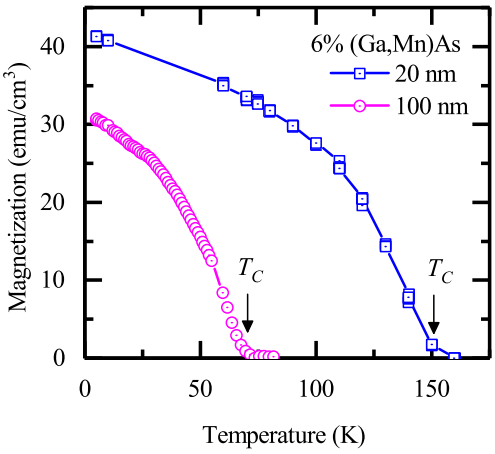

FIGURE 3.26: Temperature-dependent magnetisation obtained for the 100-nm and 20 nm-thick (Ga,Mn)As with $x = 6\%$ layers. Arrows indicate the Curie temperature (T_C) of the layers.

3.4.2 Photoreflectance and spectroscopic ellipsometry studies

In order to explain the controversial results of SE [75, 90, 91], SE and PR spectroscopy for the energy range of E_1 and $E_1 + \Delta_1$ interband transitions in (Ga,Mn)As were applied.

The SE measurements were performed at RT at the incidence angles of 70°and 80°, using the VASE (Variable Angle Spectroscopic Ellipsometer) configured with the rotating analyser. The real and imaginary parts of the pseudo dielectric function spectra were analysed using the WVASE software [163]. In the ellipsometric model, contrary to Burch et al. [75], it is assumed that after the etching the native oxide on the (Ga,Mn)As layer was negligibly thin. Its thicker oxide layer could provide an additional factor influencing a modelled dielectric function. This assumption is supported by the previous studies on the chemical etching of (Ga,Mn)As surface [19, 164, 165]. In particular, it was shown that the native oxide has a smaller growth rate on the (Ga,Mn)As surface compared to GaAs. Unfortunately, there are no extensive studies concerning the dielectric function of native oxide on the (Ga,Mn)As surface. In order to simplify

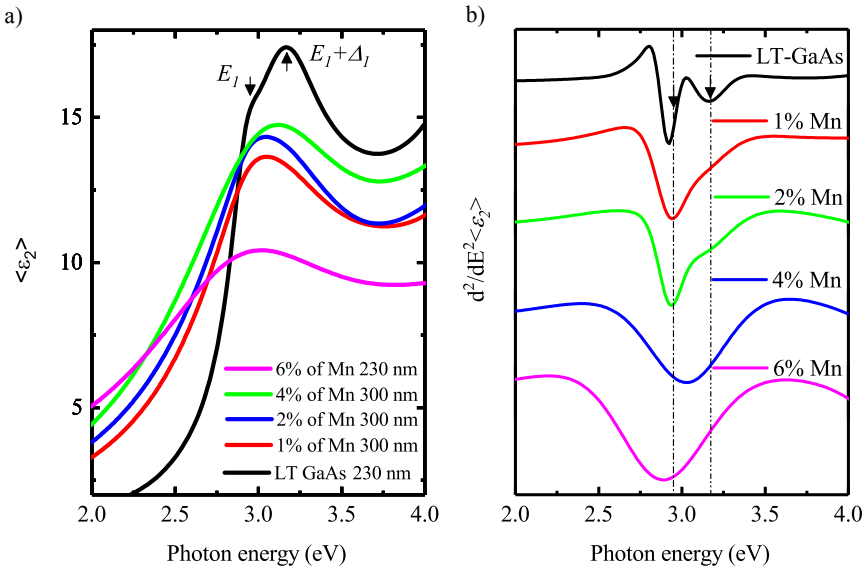

FIGURE 3.27: The modelled imaginary part of the dielectric function of the (Ga,Mn)As layers and LT-GaAs in the spectral region of E_1 and $E_1 + \Delta_1$ optical transitions. b) the second derivative of the layer modelling result. The vertical lines designate the well resolved energies of E_1 and $E_1 + \Delta_1$ of LT-GaAs.

the model by decreasing a number of fitting parameters in the SE spectra modelling, the oxide layers on (Ga,Mn)As were chemically removed and neglected in the calculations. The pseudo dielectric functions of the (Ga,Mn)As layers were obtained by means of the least-squares fit of the excitonic features E_1 and $E_1 + \Delta_1$ described by the Lorentzian oscillators, as previously used in Ref. [90] and using a simple two-phase layer/substrate model ((Ga,Mn)As/GaAs) of the heterostructures. The model of the substrate consists of the optical constants (n,k) of GaAs that were taken from the WVASE database. In the case of LT-GaAs, there was used a three-phase model, taking into account the native oxide layer with the thickness obtained from the nuclear reactions measurements (not discussed in this thesis). The model of (Ga,Mn)As layer is composed of two Lorentzians with the energies of about 2.95 eV and 3.17 eV for E_1 and $E_1 + \Delta_1$, respectively. The oxide on LT-GaAs was modelled with the standard GaAsOX model embedded in the WVASE software. The modelled spectra of the imaginary parts of the pseudo-dielectric function of the studied layers are shown in Fig. 3.27 and together with their second derivatives in Fig. 3.27 b. The spectral

features corresponding to the E_1 and $E_1 + \Delta_1$ interband transitions are clearly distinguishable in the ϵ_2 spectra only for the LT-GaAs layer. They broaden and merge into a single peak for the (Ga,Mn)As layers for the all presented Mn contents. At this point, it is also possible to fit a single feature into the peak corresponding to the broadened E_1 and $E_1 + \Delta_1$ optical transitions. However, the second derivative of the ϵ_2 (Fig. 3.27 b) revealed very small features of $E_1 + \Delta_1$ that are barely visible in the ϵ_2 spectra for the samples with 1% and 2% of Mn. For a layer with 4% and 6% of Mn the ϵ_2 spectra and its derivative revealed only single features. The spectral shift of the main peak of the similar band with the increasing Mn content in (Ga,Mn)As was analysed by Burch et al. [75]. The ϵ_2 spectra and its derivative show that there is a red shift of the main feature in the $x = 6\%$ sample compared to the $x = 4\%$ one. The energy shift of the feature depicted in Fig. 3.27 does not follow the trend from Burch et al. (significant blue shift with the increasing Mn content of ≈ 0.15 eV for $x = 6\%$). The resulting feature in the vicinity of 3 eV is rather a sum of two broadened peaks corresponding to the E_1 and $E_1 + \Delta_1$ optical transitions.

Modulation PR spectroscopy measurements were performed at RT using a set-up equipped with a 630 nm laser as a pump beam and the probe beam from a 250 W halogen lamp. The reflected PR signal was filtered by a 0.5 m focal length monochromator and then detected by a silicon photodiode with a quartz window. In this case the so-called "bright" configuration was used. That means the halogen light is reflected from a sample and then analysed with a monochromator coupled with a detector [123]. The attempts to obtain PR spectra in the photon energy range of the E_1 and $E_1 + \Delta_1$ optical transitions were unsuccessful for the as-grown (Ga,Mn)As layers with x from 1% to 6%. The main reason for that was probably a large number of defects in the near surface layer probed by the near-UV probe beam, as previously suggested by Bernussi et al. [166] and Hsu et al. [167] in their papers on the LT-MBE grown GaAs layers. This result is somewhat confirmed by the HR-TEM pictures of the

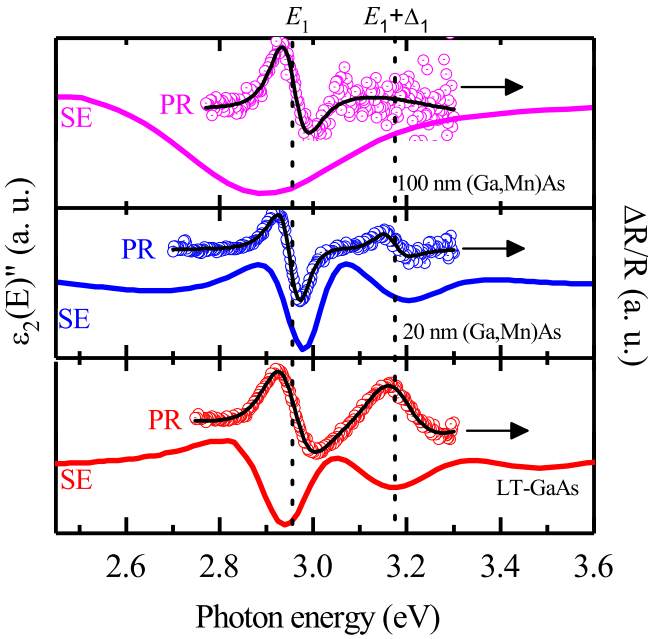

FIGURE 3.28: PR results (dots) and the second derivative of imaginary part of the pseudo dielectric function (ϵ_2) obtained from the SE spectra modelling (solid line) for the 20 nm and 100 nm-thick annealed (Ga,Mn)As layers with $x = 6\%$ and the reference LT-GaAs. The spectra were normalised to the same intensity and vertically offset. The black solid lines represent the TDLS function (eq. 2.2) fits to the experimental PR data. The vertical dashed lines indicate the energies of the E_1 and $E_1 + \Delta_1$ transitions. Reproduced from [17], with the permission of AIP Publishing.

compared as-grown and annealed samples in Fig. 3.25. The picture shows that the structure of the annealed layer is more homogeneous which may be reflected in the quality of the subsurface layer. Nonetheless, it was possible to obtain PR spectra of a reasonable quality and a signal-to-noise ratio for the reference LT-GaAs layer, shown in Fig. 3.28. Moreover, a reasonable quality of PR spectra of the $x = 6\%$ annealed (Ga,Mn)As layers was obtained. The results of SE spectra modelling are also included for comparison. The second derivatives [168] of the imaginary part of pseudo-dielectric functions were calculated to emphasise the similarities of PR and SE spectra. The vertical lines indicate the E_1 and $E_1 + \Delta_1$ mean transition energies obtained from the fitting procedure of the TDLS function (equation 2.2) considering the three-dimensional band-to-band transition in the case of the PR and SE spectra modelling [118]. The fitted

values of E_1 and $E_1 + \Delta_1$ optical transition energies are 2.95 eV and 3.16 eV, respectively for the (Ga,Mn)As layers (2.95 eV and 3.18 eV for LT-GaAs). The critical point energies calculated from the SE and PR spectra differ from each other. However, one must stress the importance of the fact that the pseudo dielectric function derivative spectrum is a result of inverse modelling. On contrary, PR gives a direct derivative-like output.

Furthermore the PR spectrum of the thinner, 20-nm-thick layer (middle spectrum in Fig. 3.28) is of much better signal-to-noise ratio than that of the thicker, 100-nm-thick one (upper spectrum in Fig. 3.28). The positions of the spectral features for the annealed (Ga,Mn)As layers are very similar. The higher signal-to-noise ratio of the PR spectrum for the 20-nm-thick layer results probably from the better surface quality and the more efficient out-diffusion of Mn_I after the annealing treatment compared to the thicker sample which is also confirmed by a significantly higher Curie temperature. In both (Ga,Mn)As films, the values of $E_1 + \Delta_1$ optical transition energy are loaded with uncertainties more than the E_1 energy value due to the larger absorption coefficient at higher energies and thus a smaller penetration depth. As well, for the energies in the vicinity of $E_1 + \Delta_1$ the surface condition plays a more important role than at E_1 energy. The spectrum of 100-nm-thick layer revealed a very unclear $E_1 + \Delta_1$ optical transition implying similarities to the single broadened E_1 feature shown by Burch et al. [75] in SE. However, the feature is not shifted compared to the LT-GaAs spectra in the way presented in Ref. [75]. The further confirmation of the valence band splitting in the studied spectral region gave the results of the 20-nm-thick layer with the well-resolved E_1 and $E_1 + \Delta_1$ spectral features visible in PR as well as in the doubly differentiated ϵ_2 spectrum. No significant blue energy shift of E_1 and $E_1 + \Delta_1$ is in agreement with Kang et al. [90]. More recently this result was confirmed by Prucnal et al. [93] using the flash lamp annealed Mn^+ ion-implanted GaAs.

Dependence of the E_1 and $E_1 + \Delta_1$ transition energies on the hole density

in p-type GaAs was previously studied using SE in ref. [169] and modulation spectroscopy methods in Ref. [170]. The SE measurements revealed a power-law dependence of the E_1 and $E_1+\Delta_1$ red shift energies with the increasing hole concentration up to 10^{20} cm^{-3}, which was attributed to the screening of dopant impurities[169]. However, this effect can be strongly influenced by the surface conditions for high doping levels, as pointed out by Kuball et al. [171]. One can assume that the power-law dependence on the hole concentration proposed in refs. [169, 171] holds for even higher concentrations of over 10^{20} cm^{-3} present in ferromagnetic (Ga,Mn)As layers. Then the red shift of about 20 meV will be expected for the 4% Mn layer compared to the 1% one for the samples used by Burch et al. [75]. On the other hand, a compressive strain in the layers leads to a blue shift of the E_1 transition as shown by Hsu et al. in Ref. [167]. The Authors pointed out to an energy shift to higher values of the E_0 and E_1 transitions for LT-GaAs as the epitaxial growth temperature decreases owing to the increasing density of defects and nonstoichiometry. In the LT-MBE grown (Ga,Mn)As layers the influence of defects, like Mn_I and As_{Ga}, on the perpendicular lattice parameter is even more evident and the lattice mismatch is larger than that in the LT-GaAs layers. The resultant change of the E_1 and $E_1+\Delta_1$ energies due to Mn doping in GaAs is then a sum of the anticompetitive effects of Mn acceptors screening and a compressive strain that may cancel each other.

3.4.3 Summary

Concluding, the SE and PR spectroscopy results of the (Ga,Mn)As/GaAs heterostructures in contradiction to the SE results by Burch et al. [75], do not show a significant blue shift of the E_1 interband transition. In consequence, the results can not be explained within the model where hybridisation of the Mn induced impurity band and the GaAs valence band is found. As confirmed by Qi et al., [172] such a hybridisation should depend on the k wavevector and be

very strong near the L point - the direction of Mn-As bonding. In consequence, the existence of the impurity band hybridisation with the valence band should lead to a distinct blue shift of the E_1 interband transition with the increasing x. In this respect, the Mn impurity band as the source of holes in highly Mn doped (Ga,Mn)As can not be confirmed.

Chapter 4

Discussion and conclusion

(Ga,Mn)As became a model ferromagnetic semiconductor whose magnetic state can be controlled by a variety of factors like light, pressure, and electric field. Due to the combination of semiconducting and magnetic properties in this material, many ideas of controlling magnetism in semiconductors were accomplished showing extensive spintronic capabilities of DMS. However, for many years the identification of the band structure source of ferromagnetism in this material has not brought a consensus. The reason for that is the complicated nature of (Ga,Mn)As. The main factors causing confusion in analysing (Ga,Mn)As are large high holes density required to obtain the ferromagnetic phase and number of double-donor point defects introduced by the LT-MBE growth. They influence nearly every experiment that undoubtedly, in other cases of some better quality materials can characterise the band structure instantly. Nevertheless, so far the LT-MBE technique has been the best method for growing high-T_C layers. The presented experimental studies challenge the question whether the impurity band or valence band is the source of spin-polarised holes in the ferromagnetic semiconductor (Ga,Mn)As. That was done using PR spectroscopy and analysis of the inter-band optical transitions. The choice of PR for analysing the optical transitions in (Ga,Mn)As was very fortunate. That is because, at the same time it was widely used for the investigations of the non-magnetic LT-MBE grown semiconductor heterostructures (LT-GaAs and Ga(Bi,As)). On the other hand, there were few reports on modulation spectroscopy applied for the LT-MBE

grown (Ga,Mn)As layers. Here, the PR studies were supplemented with other characterisation techniques to obtain a possibly broad scope of the properties of the studied samples.

Chapter 3 with the experimental results of the thesis, is divided into four parts dealing with the raised question from different points of view. Chapter 3.1, deals with the behaviour of the optical gap depending on the Mn content at the onset of magnetism. This chapter consists of RT-PR and LT-PR studies included in subchapters 3.1.1 and 3.1.2, respectively. The samples used for the RT-PR part cover the transition from the paramagnetic-to-ferromagnetic and n-to-p conductivity phase. In this series, 0.8% Mn was needed to compensate for the donor defects and to introduce a relatively small number of holes manifesting a CPLM feature in the Raman scattering spectra. However, this amount of Mn and holes was still not enough to obtain ferromagnetism. The RT-PR results showed a red shift of the optical gap for x up to 0.005% (n-type) compared to the undoped reference. The transition from n to p-type conduction with the further increasing x resulted in a blue shift of the band gap. The blue shift continues up to $x = 1.2\%$ (Ga,Mn)As layer with developed ferromagnetism. The initial red shift of the optical gap for the acceptor-compensated layers with $x \geqslant 0.005\%$ is interpreted as the build-up of the filled Mn states on top of the GaAs valence band. This controversial statement is in a contradiction with a typical picture of the (Ga,Mn)As band structure for low Mn contents before the ferromagnetic phase can be established. In this region of x, the Mn impurity band develops initially at about 100 meV above the valence band, and it does not influence the valence band [73, 77, 82, 83, 86, 94]. With the increase in the hole density and transition to p-type an ongoing blue shift of the band gap is observed in RT-PR for the samples with 0.8% (paramagnetic) and 1.2% (ferromagnetic) of the Mn content. The blue shift is interpreted as the Burstein-Moss effect. It is a result of shifting the k wave vector of the optical transition from 0 to higher values due to the band filling with holes. The magnitude of the shift

is a product of competition of band filling with the hole plasma related many-body effects and Mn states build-up. This blue shift has shed new light on the resonant tunnelling [94] and photoemission [102, 104–106] results in which the Fermi level goes upwards with the increasing x (for $x \gtrsim 1\%$) supporting the impurity band merged with the valence band picture. As a matter of fact, the Fermi level upshift due to Mn doping is consistent with the valence band theory and is a result of the hole plasma-related gap narrowing [35, 144]. Otherwise, when the band filling effect does not apply to this case the k wave vector of the optical transition will not be changed due to the acceptor doping. Consequently, an upward shift of the Fermi level pinned to the Mn impurity band due to the increasing x would be possibly seen as a red shift of the band gap in the PR studies. Similar conclusions can be drawn for the results of near-infrared optical conductivity in ref. [82] in the "impurity band conduction" regime ($x \geqslant 1.5\%$) in which the Mn impurity band has a detached form. Subchapter 3.1.2 includes more detailed studies on the magnetic, electronic, and band structure evolution of (Ga,Mn)As than it was demonstrated in subchapter 3.1.1. The main improvements are the utilisation of PR at 10 K (LT-PR), more detailed SQUID characterisation, and the use of ARPES. The PR measurements performed at 10 K allowed to get rid of broad FKO present at RT and to obtain better measuring feature separation. The Mn content in the sample series covers the transition from n to p-type with the increasing x, demonstrated by the development of CPLM feature in the Raman scattering spectra. From those data, the bordering Mn content for n- to p-type transition ($0.02\% \leqslant x_b \leqslant 0.3\%$), was identified. The SQUID measurements revealed evolution of the magnetic properties of (Ga,Mn)As from the paramagnetic ($x \leqslant 0.3\%$) through superparamagnetic ($x = 0.9\%$) to ferromagnetic phase ($x = 1.6\%$). The LT-PR studies proved that the optical spectra for the (Ga,Mn)As layers with $x \leqslant x_b$, apart from the HH and LH features visible for the reference LT-GaAs, contain the below band gap peak. The additional feature is possibly responsible for the

red shift of the FKO-rich RT-PR spectra for x up to 0.005% and is attributed to the contribution of Mn states to the GaAs valence band. Additionally, the presence of the Mn-related feature is associated with the energy split of HH and LH spectral features. The presence of the Mn-related spectral feature in the LT-PR spectra corroborates the conclusions from the RT-PR studies that the Mn states modify the top of the valence band for $x \leqslant x_b$. The same conclusion is drawn in the in-situ ARPES studies published by Kanski et al. [107] where the Authors demonstrate that the top of the valence band spectrum is deformed compared to pure GaAs for as low as 0.4% of the Mn content. Such effect was also theoretically predicted using the tight-binding Anderson approach to the band structure calculations, showing that the isolated Mn-impurity band can be seen up to about 0.1% of the Mn content [173]. Similarly to the RT studies, the LT-PR spectroscopy results contradict the hypothesis that for the (Ga,Mn)As layers with $x \leqslant x_b$ [80, 94] or even in the entire range of x [73, 82, 96], the valence band remains unperturbed. In the $x > x_b$ regime, the LT-PR spectra changed its appearance and revealed the two broadened spectral features that correspond to the optical transitions involving the HH and LH subbands. The energies of those transitions as well as the LH-HH energy splitting grow on increasing x and hole density. Furthermore, the Mn-related feature seen for $x \leqslant x_b$ is somewhat consumed by the LH-like feature in the 0.3% spectra. The blue shift of the optical transition, the energy splitting with the increasing Mn content, and vanishing of the Mn-related spectral feature for $x > x_b$ are interpreted as evidence of the Burstein-Moss shift caused by the band filling effect, that fully supports the earlier RT-PR studies. The magnitude of the shift is limited by the band gap narrowing caused by the carrier-related many-body effects influencing the Mn-modified valence band. Therefore, it is not possible to obtain an energy shift of the optical gap in acceptor doped GaAs, compared to the undoped reference that follows the values obtained only from the parabolic band approximation for a given hole density. The lack of clear and significant

Burstein-Moss shift (40 meV and 180 meV for $x = 1\%$ and 2%, respectively that can be calculated from the effective mass model) was the reason for ruling out the band filling effect from the interpretation of E_0 optical transition energies in the MCD spectra of (Ga,Mn)As layers series in Terada et al. [74]. The Raman scattering spectroscopy and SQUID results indicate that the evolution of magnetic properties from paramagnetic to ferromagnetic occurs for $x > x_b$ (p-type conduction). In this regime, however, the LT-PR spectra do not suggest any changes in the character of the holes related to the Mott insulator-to-metal transition [32, 80]. Indeed, it is widely accepted that at about 1% of the Mn content, the isolated Mn-impurity band merges with the valence band [80, 94, 111, 147]. Here, the RT and LT-PR studies demonstrate that the band filling effect may occur even for the paramagnetic $x = 0.3\%$ (Ga,Mn)As layer and continue up to 1.6% where the ferromagnetic phase occurs. The in-situ ARPES results confirm the unitary character of the valence band of the $x = 1.6\%$ sample- ferromagnetic but still low doped one which is consistent with the results of most photoemission studies [102–107]. This particular result undermines the existence of the detached impurity band and nearly unperturbed valence band for the low doped ferromagnetic (Ga,Mn)As layers shown in refs. [82, 83, 86, 96]. Furthermore, the SQUID measurements for the $x = 1.6\%$ layer revealed two orthogonal easy-axis for the ferromagnetic and superparamagnetic-like components in the [-110] and [110] directions, respectively. Such a clear distinction between the magnetic characteristics for different crystallographic directions is possible due to a strong in-plane uniaxial magnetic anisotropy whose magnitude and sign depend largely on the hole density [158]. Therefore, those two magnetic components originate from different regions of the layer with also different hole densities. The in-plane uniaxial magnetic anisotropy in (Ga,Mn)As is well explained (quantitatively) by the p-d Zener model [35].

The influence of the low-temperature annealing treatment on the optical gap in the highly doped (Ga,Mn)As layers with 6% of the Mn content was studied

in Chapter 3.2. However, for the discussion it is suitable to include here also the analysis of the samples submitted to annealing from Chapter 3.3 with $x = 4\%$. In both cases the annealing treatment caused typical changes of layers properties like an increase in T_C, a decrease in coercivity in the $M(H)$ loops, and a red shift of the hole-related CPLM feature in the Raman spectra as a result of the increase in the hole density. The RT-PR measurements revealed several-meV changes in the optical gap due to Mn-doping and annealing. However, those two series of samples revealed different patterns of those changes. First of all, besides the annealing effects, the optical gap of the as-grown (Ga,Mn)As (or (Ga,Mn)As/Sb) with $x = 6\%$ in Chapter 3.2 decreased its values in comparison to the LT-GaAs energy gap value. A similar effect was observed in the as-grown $x = 6\%$ sample by Yastrubchak et al. [87]. On the other hand, as-grown LT-GaAs and LT-Ga(Bi,As) doped with Mn in Chapter 3.3 exhibited a blue shift of the E_0 transition energies compared to the undoped reference. In the paper by Yastrubchak et al. [87] the $x = 4\%$ layer displayed a red shift of the optical gap compared to the reference layer. Based on the SQUID and Raman scattering spectroscopy results from Chapters 3.2 and 3.3 in this thesis, it can be concluded that both present sample series with $x = 4\%$ and 6% were epitaxially grown under different conditions whereby the samples with $x = 4\%$ are better defect-optimised. An analogous situation was observed by Terada et al. [74] in the MCD studies where for $x = 2\%$ (Ga,Mn)As (as-grown, $T_C = 41$ K) the Authors proved a significant 30 meV blue shift of the E_0 transition and no shift for $x = 8\%$ (annealed, $T_C = 85$ K). That indicates the importance of electronic compensation at different levels of disorder that influences the Fermi level position in the Mn-disordered top of the GaAs valence band. Indeed, the level compensation may cause either a blue or red shift of the optical gap due to high-Mn doping depending on the growth conditions. That differentiation can not be explained based on the impurity band models. For a majority of papers showing the studies on highly-Mn-doped (Ga,Mn)As the band structure

interpretation indicates the Mn states merged with the valence band with the Fermi level pinned to the Mn-related extended states within the GaAs band gap (for the ferromagnetic samples with $x > 1\%$) [94, 96, 98, 102, 104–106]. The results presented in the thesis seem to be somewhat in agreement with this picture with the exception that the Fermi level lies in the Mn modified and extended valence band. This description is in line with the interpretation provided by Yastrubchak et al. [87]. The annealing treatment in both $x = 4\%$ and 6% caused an increase in the optical gap energy due to the lowering of the Fermi level. In all the cases, the resultant gap energy was higher than the optical gap in the reference samples despite not clear initial situation seen in the as-grown layers. That evidences directly the presence of the band filling effect due to the acceptor doping in the largely doped (Ga,Mn)As layers. On the other hand, one can have a closer look at the Fermi level shifts found in other experiments. For the 6% layers, the resonant tunnelling shows 50 meV upshift of the Fermi level from the top of the valence band and 30 meV for 4% [94, 96]. The high-resolution hard X-ray photoemission spectroscopy experiment exhibited 50 meV for $x = 13\%$ [104]. Those values of the Fermi level shifts related to the energy of the GaAs valence band top are not found in the PR studies. That suggests the effect of the Fermi level upshift seen in the resonant tunnelling and photoemission experiments is reduced in the PR measurements because the optical transitions are excited from $k \neq 0$.

Chapter 3.3 includes the very first results of Bi co-doping in (Ga,Mn)As and its influence on structural electronic and magnetic properties. Bi doping caused an increase in the lattice parameter and a decrease in T_C compared to (Ga,Mn)As. The decrease in T_C is explained as a result of the increasing Mn-Mn distances due to Bi doping. On the other hand, Dietl et al. [11] noted that the increase in the magnitude of spin-orbit interactions could impact T_C, as shown for the case of (Zn,Mn)Te. As expected, the band gap of (Ga,Bi)As is red-shifted as compared to LT-GaAs by 25 meV for 0.3% Bi. This result

is in quantitative agreement with the VBAC model [85] and also more recent calculations [174]. In turn, Mn-acceptor doping of Ga(Bi,As) caused a blue shift of the optical gap. Annealing of (Ga,Mn)(Bi,As) led to a further increase of the band gap due to an increase in the hole density by Mn_I defects out-diffusion, similarly as in the case of (Ga,Mn)As samples from this series. The energies of the optical gap in the (Ga,Mn)(Bi,As) layers are always smaller than in (Ga,Mn)As. That indicates explicitly the occurrence of the Burstein-Moss shift due to the band filling effect in the Bi-modified valence band. Nevertheless, the result is difficult to verify because of a lack of studies on the band gap in the LT-grown p-type Ga(Bi,As) which also identifies a knowledge gap. Based on the impurity band scenario, the Bi-induced red shift of the band gap in LT-GaAs would be enhanced due to Mn doping because of the the Fermi level upshift [94]. Therefore, the results support the conclusions mentioned above on the band filling effect in pure (Ga,Mn)As.

Finally, chapter 3.4 shows the ellipsometric and PR studies on E_1 and $E_1 + \Delta_1$ optical (at L direction of the Brillouin zone) transitions in the highly doped (Ga,Mn)As layers with $x = 6\%$. This chapter is a response and validation of the paper published by Burch et al. [75] that is often cited as an example confirming the Mn impurity band theory. In that paper, the peak associated with the E_1 optical transition blue-shifts with the increasing x (up to 6.6%) in (Ga,Mn)As indicating hybridisation between the Mn-derived impurity band and the valence band states. However, the PR and SE studies presented in this thesis demonstrate that the E_1 and $E_1 + \Delta_1$ critical point energies do not shift even for $x = 6\%$ as compared to the energy values for the undoped reference. The research results obtained by Burch et al. [75] were not confirmed later by Zhu et al. [175], Prucnal et al. [93], and Gan'shina et al. [176] either.

The findings shown in the thesis contribute to the discussion on the nature of the band structure of (Ga,Mn)As. The results demonstrate that the short

and long range ferromagnetism is mediated by the valence band holes in Mn-doped p-type GaAs. This can help to develop new ways to control spins in semiconductors by improving the band structure models. On the other hand, better understanding of the band structure of (Ga,Mn)As can support knowledge about the interplay between the disorder and the magnetic interactions in the complex solid state systems.

Appendix A

Statement of Contribution

- **Chapter 3.1.1**

  HR-XRD: Dr. J.Z. Domagała (IP PAS) - measurements and calculations.

  Raman spectroscopy: MSc. R. Keller, Dr. O. Yastrubchak (MCSU) - measurements, Ł. Gluba, Dr. O. Yastrubchak (MCSU) - analysis.

  PR spectroscopy: Dr. O. Yastrubchak (MCSU), Ł. Gluba - measurements, Dr. O. Yastrubchak (MCSU), Dr. H. Krzyżanowska (VU), Ł. Gluba - analysis.

  SQUID: Dr. T Andrearczyk (IP PAS) - measurements.

  MBE growth: Prof. J. Sadowski (MAX-IV/IP PAS).

  Results integration/conclusions: Dr. O. Yastrubchak (MCSU), Prof. T. Wosiński (IP PAS), Ł. Gluba, Prof. J. Sadowski (MAX-IV/IP PAS), J. Żuk (MCSU).

- **Chapter. 3.1.2**

  HR -XRD: Dr. J.Z. Domagała (IP PAS) - measurements and calculations.

  SIMS: R. Jakieła (IP PAS) - measurements.

  Raman spectroscopy: MSc. R. Keller (MCSU), Ł. Gluba - measurements, Ł. Gluba, O. Yastrubchak (MCSU) - analysis.

PR spectroscopy: Ł. Gluba - measurements, Ł. Gluba, Dr. O. Yastrubchak (MCSU) - analysis.

ARPES: Ł. Gluba, Dr. O. Yastrubchak (MCSU), Mats Leandersson (MAX-IV) - measurements, Ł. Gluba, Dr. O. Yastrubchak (MCSU) - analysis.

SQUID: Prof. M. Sawicki (IP PAS) - measurements and analysis.

MBE growth: Prof. J. Sadowski (MAX-IV/IP PAS).

Results integration/conclusions: Ł. Gluba, Dr. O.Yastrubchak (MCSU), Prof. M. Sawicki (IP PAS), Prof. J. Sadowski (MAX-IV/IP PAS), Prof. T.Wosiński (IP PAS), Prof. J. Żuk (MCSU).

- **Chapter 3.2**

HR -XRD: Dr. J.Z. Domagała (IP PAS) - measurements and calculations.

Raman spectroscopy: MSc. R. Keller (MCSU), Dr. O. Yastrubchak (MCSU) - measurements, Ł.Gluba - analysis.

PR spectroscopy: Dr. O. Yastrubchak (MCSU), Ł. Gluba - measurements and analysis.

SQUID: Dr. T. Andrearczyk (IP PAS) - measurements.

MBE growth: Prof. J. Sadowski (MAX-IV/IP PAS).

Results integration/conclusions: Dr. O.Yastrubchak (MCSU), Prof. T.Wosiński (IP PAS), Prof. J. Sadowski (MAX-IV/IP PAS). Ł. Gluba, J. Żuk (MCSU).

- **Chapter 3.3**

HR-XRD: Dr. J.Z. Domagała (IP PAS) - measurements and calculations.

Raman spectroscopy: MSc. R. Keller (MCSU), Ł. Gluba - measurements, Ł. Gluba, O. Yastrubchak - analysis.

PR spectroscopy: Ł. Gluba, Dr. O. Yastrubchak (MCSU) - measurements, Ł. Gluba - calculations.

SQUID: Dr. T. Andrearczyk (IP PAS) - measurements.

MBE growth: Prof. J. Sadowski (MAX-IV/IP PAS).

RBS/NR: Dr. M. Kulik (MCSU/JINR) - measurements and calculations.

HR-TEM: Dr. M. Rawski (MCSU) - measurements.

Results integration/conclusions: Dr. O. Yastrubchak (MCSU), Prof. T. Wosiński (IP PAS), Ł. Gluba, Prof. J. Sadowski (MAX-IV/IP PAS), Prof. J. Żuk (MCSU).

- **Chapter 3.4**

PR spectroscopy: Prof. G.Sęk (WUT), Dr. W. Rudno-Rudziński (WUT), Ł. Gluba - measurements, Ł. Gluba - calculations.

SQUID: Dr. T. Andrearczyk (IP PAS) - measurements.

MBE growth: Prof. J. Sadowski (MAX-IV/IP PAS).

SE: MSc. W. Rzodkiewicz (IET), Dr. M. Kulik (MCSU) - measurements, Ł. Gluba - calculations.

RBS/NR: Dr. M. Kulik (MCSU/JINR) - measurements and calculations.

HR-TEM: Dr. M. Rawski (MCSU) - measurements.

Results integration/conclusions: Ł. Gluba, Dr. O. Yastrubchak (MCSU), Prof. T. Wosiński (IP PAS), Prof. J. Żuk (MCSU).

References

[1]L. J. Edgar, *Method and apparatus for controlling electric currents*, US Patent 1,745,175, 1930.

[2]L. J. Edgar, *Device for controlling electric current*, US Patent 1,900,018, 1933.

[3]M. N. Baibich, J. M. Broto, A. Fert, F. N. V. Dau, F. Petroff, P. Etienne, G. Creuzet, A. Friederich, and J. Chazelas, "Giant magnetoresistance of (001)Fe/(001)Cr magnetic superlattices", Phys. Rev. Lett. **61**, 2472–2475 (1988).

[4]J. K. Furdyna, "Diluted magnetic semiconductors", J. Appl. Phys. **64**, R29–R64 (1988).

[5]T. Story, R. R. Gałązka, R. B. Frankel, and P. A. Wolff, "Carrier-concentration–induced ferromagnetism in PbSnMnTe", Phys. Rev. Lett. **56**, 777–779 (1986).

[6]A. Haury, A. Wasiela, A. Arnoult, J. Cibert, S. Tatarenko, T. Dietl, and Y. M. d'Aubigné, "Observation of a Ferromagnetic Transition Induced by Two-Dimensional Hole Gas in Modulation-Doped CdMnTe Quantum Wells", Phys. Rev. Lett. **79**, 511–514 (1997).

[7]H. Munekata, H. Ohno, S. von Molnar, A. Segmüller, L. L. Chang, and L. Esaki, "Diluted magnetic III-V semiconductors", Phys. Rev. Lett. **63**, 1849–1852 (1989).

[8]H. Ohno, H. Munekata, T. Penney, S. von Molnár, and L. L. Chang, "Magnetotransport properties of p-type (In,Mn)As diluted magnetic III-V semiconductors", Phys. Rev. Lett. **68**, 2664–2667 (1992).

[9]H. Ohno, A. Shen, F. Matsukura, A. Oiwa, A. Endo, S. Katsumoto, and Y. Iye, "(Ga,Mn)As: a new diluted magnetic semiconductor based on GaAs", Appl. Phys. Lett. **69**, 363–365 (1996).

[10]M. Wang, R. P. Campion, A. W. Rushforth, K. W. Edmonds, C. T. Foxon, and B. L. Gallagher, "Achieving high Curie temperature in (Ga,Mn)As", Appl. Phys. Lett. **93**, 132103 (2008).

[11]T. Dietl, "Zener Model Description of Ferromagnetism in Zinc-Blende Magnetic Semiconductors", Science **287**, 1019–1022 (2000).

[12]T. Jungwirth, J. Wunderlich, V. Novák, K. Olejník, B. Gallagher, R. Campion, K. Edmonds, A. Rushforth, A. Ferguson, and P. Němec, "Spin-dependent phenomena and device concepts explored in (Ga,Mn)As", Rev. Mod. Phys. **86**, 855–896 (2014).

[13]L. Gluba, O. Yastrubchak, J. Z. Domagala, R. Jakiela, T. Andrearczyk, J. Żuk, T. Wosinski, J. Sadowski, and M. Sawicki, "Band structure evolution and the origin of magnetism in (Ga,Mn)As: from paramagnetic through superparamagnetic to ferromagnetic phase", Phys. Rev. B **97**, 115201 (2018).

[14]O. Yastrubchak, J. Sadowski, H. Krzyżanowska, L. Gluba, J. Żuk, J. Z. Domagala, T. Andrearczyk, and T. Wosinski, "Electronic- and band-structure evolution in low-doped (Ga,Mn)As", J. Appl. Phys. **114**, 053710 (2013).

[15]O. Yastrubchak, T. Wosinski, L. Gluba, T. Andrearczyk, J. Z. Domagala, J. Żuk, and J. Sadowski, "Effect of low-temperature annealing on the electronic- and band-structures of (Ga,Mn)As epitaxial layers", J. Appl. Phys. **115**, 012009 (2014).

[16]O. Yastrubchak, J. Sadowski, L. Gluba, J. Z. Domagala, M. Rawski, J. Żuk, M. Kulik, T. Andrearczyk, and T. Wosinski, "Ferromagnetism and the electronic band structure in (Ga,Mn)(Bi,As) epitaxial layers", Appl. Phys. Lett. **105**, 072402 (2014).

[17]L. Gluba, O. Yastrubchak, G. Sęk, W. Rudno-Rudziński, J. Sadowski, M. Kulik, W. Rzodkiewicz, M. Rawski, T. Andrearczyk, J. Misiewicz, T. Wosinski, and J. Żuk, "On the nature of the Mn-related states in the band structure of (Ga,Mn)As alloys via probing the E_1 and $E_1 + \Delta_1$ optical transitions", Appl. Phys. Lett. **105**, 032408 (2014).

[18]K. C. Ku, S. J. Potashnik, R. F. Wang, S. H. Chun, P. Schiffer, N. Samarth, M. J. Seong, A. Mascarenhas, E. Johnston-Halperin, R. C. Myers, A. C. Gossard, and D. D. Awschalom, "Highly enhanced Curie temperature in low-temperature annealed [Ga,Mn]As epilayers", Appl. Phys. Lett. **82**, 2302–2304 (2003).

[19]K. Olejník, M. H. S. Owen, V. Novák, J. Mašek, A. C. Irvine, J. Wunderlich, and T. Jungwirth, "Enhanced annealing, high Curie temperature, and low-voltage gating in (Ga,Mn)As: A surface oxide control study", Phys. Rev. B **78**, 054403 (2008).

[20]A. H. MacDonald, P. Schiffer, and N. Samarth, "Ferromagnetic semiconductors: moving beyond (Ga,Mn)As", Nat. Mater. **4**, 195–202 (2005).

[21]M. Henini, *Molecular beam epitaxy: from research to mass production* (Elsevier, 2013).

[22]F. Máca and J. Mašek, "Electronic states in $Ga_{1-x}Mn_xAs$: Substitutional versus interstitial position of Mn", Phys. Rev. B **65**, 235209 (2002).

[23]E. R. Weber, H. Ennen, U. Kaufmann, J. Windscheif, J. Schneider, and T. Wosinski, "Identification of As_{Ga} antisites in plastically deformed GaAs", J. Appl. Phys. **53**, 6140–6143 (1982).

[24]Z. G. Yu and M. E. Flatté, "Spin diffusion and injection in semiconductor structures: electric field effects", Phys. Rev. B **66**, 235302 (2002).

[25]K. W. Edmonds, P. Bogusławski, K. Y. Wang, R. P. Campion, S. N. Novikov, N. R. S. Farley, B. L. Gallagher, C. T. Foxon, M. Sawicki, T. Dietl, M. Buongiorno Nardelli, and J. Bernholc, "Mn Interstitial Diffusion in (Ga, Mn)As", Phys. Rev. Lett. **92**, 037201 (2004).

[26]T. Dietl, K. Sato, T. Fukushima, A. Bonanni, M. Jamet, A. Barski, S. Kuroda, M. Tanaka, P. N. Hai, and H. Katayama-Yoshida, "Spinodal nanodecomposition in semiconductors doped with transition metals", Rev. Mod. Phys. **87**, 1311–1377 (2015).

[27]J. Blinowski and P. Kacman, "Spin interactions of interstitial Mn ions in ferromagnetic GaMnAs", Phys. Rev. B **67**, 121204 (2003).

[28]D. E. Bliss, W. Walukiewicz, J. W. A. III, E. E. Haller, K. T. Chan, and S. Tanigawa, "Annealing studies of low-temperature-grown GaAs:Be", J. Appl. Phys. **71**, 1699–1707 (1992).

[29]R. Campion, K. Edmonds, L. Zhao, K. Wang, C. Foxon, B. Gallagher, and C. Staddon, "High-quality GaMnAs films grown with arsenic dimers", J. Cryst. Growth **247**, 42–48 (2003).

[30]H. Ohno, "Properties of ferromagnetic III–V semiconductors", J. Magn. Magn. Mater. **200**, 110–129 (1999).

[31]F. Matsukura, H. Ohno, A. Shen, and Y. Sugawara, "Transport properties and origin of ferromagnetism in (Ga,Mn)As", Phys. Rev. B **57**, R2037–R2040 (1998).

[32]T. Jungwirth, J. Sinova, J. Mašek, J. Kučera, and A. H. MacDonald, "Theory of ferromagnetic (III,Mn)V semiconductors", Rev. Mod. Phys. **78**, 809–864 (2006).

[33]T. Dietl, "Ferromagnetic semiconductors", Semicond. Sci. Technol. **17**, 377–392 (2002).

[34]G. Bir and G. Pikus, *Symmetry and strain-induced effects in semiconductors* (Wiley, 1974).

[35]T. Dietl, H. Ohno, and F. Matsukura, "Hole-mediated ferromagnetism in tetrahedrally coordinated semiconductors", Phys. Rev. B **63**, 195205 (2001).

[36]T. Dietl, A. Haury, and Y. M. d'Aubigné, "Free carrier-induced ferromagnetism in structures of diluted magnetic semiconductors", Phys. Rev. B **55**, R3347–R3350 (1997).

[37]T. Jungwirth, W. A. Atkinson, B. H. Lee, and A. H. MacDonald, "Interlayer coupling in ferromagnetic semiconductor superlattices", Phys. Rev. B **59**, 9818–9821 (1999).

[38]T. Jungwirth, K. Y. Wang, J. Mašek, K. W. Edmonds, J. König, J. Sinova, M. Polini, N. A. Goncharuk, A. H. MacDonald, M. Sawicki, A. W. Rushforth, R. P. Campion, L. X. Zhao, C. T. Foxon, and B. L. Gallagher, "Prospects for high temperature ferromagnetism in (Ga,Mn)As semiconductors", Phys. Rev. B **72**, 165204 (2005).

[39]M. Wang, K. W. Edmonds, B. L. Gallagher, A. W. Rushforth, O. Makarovsky, A. Patanè, R. P. Campion, C. T. Foxon, V. Novak, and T. Jungwirth, "High Curie temperatures at low compensation in the ferromagnetic semiconductor (Ga,Mn)As", Phys. Rev. B **87**, 121301 (2013).

[40]M. A. Mayer, P. R. Stone, N. Miller, H. M. Smith, O. D. Dubon, E. E. Haller, K. M. Yu, W. Walukiewicz, X. Liu, and J. K. Furdyna, "Electronic structure of $Ga_{1-x}Mn_xAs$ analyzed according to hole-concentration-dependent measurements", Phys. Rev. B **81**, 045205 (2010).

[41]Y. Nishitani, D. Chiba, M. Endo, M. Sawicki, F. Matsukura, T. Dietl, and H. Ohno, "Curie temperature versus hole concentration in field-effect structures of $Ga_{1-x}Mn_xAs$", Phys. Rev. B **81**, 045208 (2010).

[42] M. Sawicki, D. Chiba, A. Korbecka, Y. Nishitani, J. A. Majewski, F. Matsukura, T. Dietl, and H. Ohno, "Experimental probing of the interplay between ferromagnetism and localization in (Ga,Mn)As", Nat. Phys. **6**, 22–25 (2009).

[43] M. Gryglas-Borysiewicz, A. Kwiatkowski, M. Baj, D. Wasik, J. Przybytek, and J. Sadowski, "Hydrostatic pressure study of the paramagnetic-ferromagnetic phase transition in (Ga,Mn)As", Phys. Rev. B **82**, 153204 (2010).

[44] M. Sawicki, F. Matsukura, A. Idziaszek, T. Dietl, G. M. Schott, C. Ruester, C. Gould, G. Karczewski, G. Schmidt, and L. W. Molenkamp, "Temperature dependent magnetic anisotropy in (Ga,Mn)As layers", Phys. Rev. B **70**, 245325 (2004).

[45] J. Zemen, J. Kučera, K. Olejník, and T. Jungwirth, "Magnetocrystalline anisotropies in (Ga,Mn)As: systematic theoretical study and comparison with experiment", Phys. Rev. B **80**, 155203 (2009).

[46] U. Welp, V. K. Vlasko-Vlasov, X. Liu, J. K. Furdyna, and T. Wojtowicz, "Magnetic Domain Structure and Magnetic Anisotropy in $Ga_{1-x}Mn_xAs$", Phys. Rev. Lett. **90**, 167206 (2003).

[47] A. Sugawara, H. Kasai, A. Tonomura, P. D. Brown, R. P. Campion, K. W. Edmonds, B. L. Gallagher, J. Zemen, and T. Jungwirth, "Domain Walls in the (Ga,Mn)As Diluted Magnetic Semiconductor", Phys. Rev. Lett. **100**, 047202 (2008).

[48] G. Alvarez, M. Mayr, and E. Dagotto, "Phase Diagram of a Model for Diluted Magnetic Semiconductors Beyond Mean-Field Approximations", Phys. Rev. Lett. **89**, 277202 (2002).

[49] P. Mahadevan and A. Zunger, "First-principles investigation of the assumptions underlying model-hamiltonian approaches to ferromagnetism of 3d impurities in III-V semiconductors", Phys. Rev. B **69**, 115211 (2004).

[50]G. Alvarez and E. Dagotto, "Single-band model for diluted magnetic semiconductors: dynamical and transport properties and relevance of clustered states", Phys. Rev. B **68**, 045202 (2003).

[51]S. Sanvito, P. Ordejón, and N. A. Hill, "First-principles study of the origin and nature of ferromagnetism in $Ga_{1-x}Mn_xAs$", Phys. Rev. B **63**, 165206 (2001).

[52]R. N. Bhatt, M. Berciu, M. P. Kennett, and X. Wan, "Diluted Magnetic Semiconductors in the Low Carrier Density Regime", Journal of Superconductivity **15**, 71–83 (2002).

[53]M. Berciu and R. N. Bhatt, "Effects of Disorder on Ferromagnetism in Diluted Magnetic Semiconductors", Phys. Rev. Lett. **87**, 107203 (2001).

[54]M. A. Majidi, J. Moreno, M. Jarrell, R. S. Fishman, and K. Aryanpour, "Dynamics of impurity and valence bands in $Ga_{1-x}Mn_xAs$ within the dynamical mean-field approximation", Phys. Rev. B **74**, 115205 (2006).

[55]M. Berciu and R. N. Bhatt, "Mean-field approach to ferromagnetism in (III, Mn)V diluted magnetic semiconductors at low carrier densities", Phys. Rev. B **69**, 045202 (2004).

[56]A. Chattopadhyay, S. D. Sarma, and A. J. Millis, "Transition temperature of ferromagnetic semiconductors: a dynamical mean field study", Phys. Rev. Lett. **87**, 227202 (2001).

[57]E. H. Hwang, A. J. Millis, and S. D. Sarma, "Optical conductivity of ferromagnetic semiconductors", Phys. Rev. B **65**, 233206 (2002).

[58]K. M. Yu, W. Walukiewicz, T. Wojtowicz, I. Kuryliszyn, X. Liu, Y. Sasaki, and J. K. Furdyna, "Effect of the location of Mn sites in ferromagnetic $Ga_{1-x}Mn_xAs$ on its Curie temperature", Phys. Rev. B **65**, 201303(R) (2002).

[59]P. Krstajić, F. Peeters, V. Ivanov, V. Fleurov, and K. Kikoin, "Double-exchange mechanisms for Mn-doped III-V ferromagnetic semiconductors", Phys. Rev. B **70**, 195215 (2004).

[60]E. J. Singley, K. S. Burch, R. Kawakami, J. Stephens, D. D. Awschalom, and D. N. Basov, "Electronic structure and carrier dynamics of the ferromagnetic semiconductor $Ga_{1-x}Mn_xAs$", Phys. Rev. B **68**, 165204 (2003).

[61]K. Ando, T. Hayashi, M. Tanaka, and A. Twardowski, "Magneto-optic effect of the ferromagnetic diluted magnetic semiconductor $Ga_{1-x}Mn_xAs$", J. Appl. Phys. **83**, 6548–6550 (1998).

[62]J. Szczytko, W. Mac, A. Twardowski, F. Matsukura, and H. Ohno, "Antiferromagnetic $p-d$ exchange in ferromagnetic $Ga_{1-x}Mn_xAs$ epilayers", Phys. Rev. B **59**, 12935–12939 (1999).

[63]T. Komori, T. Ishikawa, T. Kuroda, J. Yoshino, F. Minami, and S. Koshihara, "Carrier-density dependence of magnetic and magneto-optical properties of (Ga,Mn)As", Phys. Rev. B **67**, 115203 (2003).

[64]J. Szczytko, W. Bardyszewski, and A. Twardowski, "Optical absorption in random media: application to $Ga_{1-x}Mn_xAs$ epilayers", Phys. Rev. B **64**, 075306 (2001).

[65]K. Ando, H. Saito, K. C. Agarwal, M. C. Debnath, and V. Zayets, "Origin of the Anomalous Magnetic Circular Dichroism Spectral Shape in Ferromagnetic $Ga_{1-x}Mn_xAs$: Impurity Bands inside the Band Gap", Phys. Rev. Lett. **100**, 067204 (2008).

[66]B. Beschoten, P. A. Crowell, I. Malajovich, D. D. Awschalom, F. Matsukura, A. Shen, and H. Ohno, "Magnetic Circular Dichroism Studies of Carrier-Induced Ferromagnetism in $Ga_{1-x}Mn_xAs$", Phys. Rev. Lett. **83**, 3073–3076 (1999).

[67] M. Turek, J. Siewert, and J. Fabian, "Magnetic circular dichroism in $Ga_{1-x}Mn_xAs$: Theoretical evidence for and against an impurity band", Phys. Rev. B **80**, 161201(R) (2009).

[68] J. Mašek, J. Kudrnovský, F. Máca, J. Sinova, A. H. MacDonald, R. P. Campion, B. L. Gallagher, and T. Jungwirth, "Mn-doped Ga(As,P) and (Al,Ga)As ferromagnetic semiconductors: Electronic structure calculations", Phys. Rev. B **75**, 045202 (2007).

[69] J.-M. Tang and M. Flatté, "Multiband Tight-Binding Model of Local Magnetism in $Ga_{1-x}Mn_xAs$", Phys. Rev. Lett. **92**, 047201 (2004).

[70] K. Ando, "Comment on "Common origin of ferromagnetism and band edge Zeeman splitting in (Ga,Mn)As at low Mn concentrations" [Appl. Phys. Lett. 91, 171118 (2007)]", Appl. Phys. Lett. **94**, 156101 (2009).

[71] R. Chakarvorty, S. Shen, K. J. Yee, T. Wojtowicz, R. Jakiela, A. Barcz, X. Liu, J. K. Furdyna, and M. Dobrowolska, "Common origin of ferromagnetism and band edge Zeeman splitting in GaMnAs at low Mn concentrations", Appl. Phys. Lett. **91**, 171118 (2007).

[72] R. Chakarvorty, S. Shen, K. J. Yee, T. Wojtowicz, R. Jakiela, A. Barcz, X. Liu, J. K. Furdyna, and M. Dobrowolska, "Response to "Comment on 'Common origin of ferromagnetism and band edge Zeeman splitting in GaMnAs at low Mn concentrations'" [Appl. Phys. Lett. 94, 156101 (2009)]", Appl. Phys. Lett. **94**, 156102 (2009).

[73] M. Berciu, R. Chakarvorty, Y. Y. Zhou, M. T. Alam, K. Traudt, R. Jakiela, A. Barcz, T. Wojtowicz, X. Liu, J. K. Furdyna, and M. Dobrowolska, "Origin of Magnetic Circular Dichroism in GaMnAs: Giant Zeeman Splitting versus Spin Dependent Density of States", Phys. Rev. Lett. **102**, 247202 (2009).

[74] H. Terada, S. Ohya, and M. Tanaka, "Intrinsic magneto-optical spectra of GaMnAs", Appl. Phys. Lett. **106**, 222406 (2015).

[75]K. S. Burch, J. Stephens, R. K. Kawakami, D. D. Awschalom, and D. N. Basov, "Ellipsometric study of the electronic structure of $Ga_{1-x}Mn_xAs$ and low-temperature GaAs", Phys. Rev. B **70**, 205208 (2004).

[76]E. J. Singley, R. Kawakami, D. D. Awschalom, and D. N. Basov, "Infrared Probe of Itinerant Ferromagnetism in $Ga_{1-x}Mn_xAs$", Phys. Rev. Lett. **89**, 097203 (2002).

[77]K. S. Burch, D. B. Shrekenhamer, E. J. Singley, J. Stephens, B. L. Sheu, R. K. Kawakami, P. Schiffer, N. Samarth, D. D. Awschalom, and D. N. Basov, "Impurity Band Conduction in a High Temperature Ferromagnetic Semiconductor", Phys. Rev. Lett. **97**, 087208 (2006).

[78]W. Songprakob, R. Zallen, D. V. Tsu, and W. K. Liu, "Intervalenceband and plasmon optical absorption in heavily doped GaAs:C", J. Appl. Phys. **91**, 171 (2002).

[79]J. Sinova, T. Jungwirth, S.-R. E. Yang, J. Kučera, and A. H. MacDonald, "Infrared conductivity of metallic (III,Mn)V ferromagnets", Phys. Rev. B **66**, 041202(R) (2002).

[80]T. Jungwirth, J. Sinova, A. H. MacDonald, B. L. Gallagher, V. Novák, K. W. Edmonds, A. W. Rushforth, R. P. Campion, C. T. Foxon, L. Eaves, E. Olejník, J. Mašek, S.-R. E. Yang, J. Wunderlich, C. Gould, L. W. Molenkamp, T. Dietl, and H. Ohno, "Character of states near the Fermi level in (Ga,Mn)As: Impurity to valence band crossover", Phys. Rev. B **76**, 125206 (2007).

[81]T. Dietl and H. Ohno, "Dilute ferromagnetic semiconductors: physics and spintronic structures", Rev. Mod. Phys. **86**, 187–251 (2014).

[82]B. C. Chapler, R. C. Myers, S. Mack, A. Frenzel, B. C. Pursley, K. S. Burch, E. J. Singley, A. M. Dattelbaum, N. Samarth, D. D. Awschalom, and D. N. Basov, "Infrared probe of the insulator-to-metal transition in $Ga_{1-x}Mn_xAs$ and $Ga_{1-x}Be_xAs$", Phys. Rev. B **84**, 081203 (2011).

[83]B. C. Chapler, S. Mack, L. Ju, T. W. Elson, B. W. Boudouris, E. Namdas, J. D. Yuen, A. J. Heeger, N. Samarth, M. D. Ventra, R. A. Segalman, D. D. Awschalom, F. Wang, and D. N. Basov, "Infrared conductivity of hole accumulation and depletion layers in (Ga,Mn)As- and (Ga,Be)As-based electric field-effect devices", Phys. Rev. B **86**, 165302 (2012).

[84]C. Śliwa and T. Dietl, "Thermodynamic and thermoelectric properties of (Ga,Mn)As and related compounds", Phys. Rev. B **83**, 245210 (2011).

[85]K. Alberi, J. Wu, W. Walukiewicz, K. M. Yu, O. D. Dubon, S. P. Watkins, C. X. Wang, X. Liu, Y.-J. Cho, and J. Furdyna, "Valence-band anticrossing in mismatched III-V semiconductor alloys", Phys. Rev. B **75**, 045203 (2007).

[86]K. Alberi, K. M. Yu, P. R. Stone, O. D. Dubon, W. Walukiewicz, T. Wojtowicz, X. Liu, and J. K. Furdyna, "Formation of Mn-derived impurity band in III-Mn-V alloys by valence band anticrossing", Phys. Rev. B **78**, 075201 (2008).

[87]O. Yastrubchak, J. Żuk, H. Krzyżanowska, J. Z. Domagala, T. Andrearczyk, J. Sadowski, and T. Wosinski, "Photoreflectance study of the fundamental optical properties of (Ga,Mn)As epitaxial films", Phys. Rev. B **83**, 245201 (2011).

[88]T. de Boer, A. Gamouras, S. March, V. Novák, and K. C. Hall, "Observation of a blue shift in the optical response at the fundamental band gap in $Ga_{1-x}Mn_xAs$", Phys. Rev. B **85**, 033202 (2012).

[89]M. Yildirim, S. March, R. Mathew, A. Gamouras, X. Liu, M. Dobrowolska, J. K. Furdyna, and K. C. Hall, "Electronic structure of $Ga_{1-x}Mn_xAs$ probed by four-wave mixing spectroscopy", Phys. Rev. B **84**, 121202 (2011).

[90]T. D. Kang, G. S. Lee, H. Lee, D. Koh, and Y. J. Park, "Optical properties of $Ga_{1-x}Mn_xAs$ ($0 \leq x \leq 0.09$) studied using spectroscopic ellipsometry", J. Korean Phys. Soc **46**, 482 (2005).

[91]F. Peiris, T. Scully, X. Liu, and J. Furdyna, "Temperature dependent dielectric functions of molecular beam epitaxy-grown $Ga_{1-x}Mn_xAs$ thin films", Solid State Commun. **199**, 22–25 (2014).

[92]H. Tanaka, M. Bsatee, and W. M. Jadwisienczak, "Zeeman splitting of ferromagnetic GaMnAs on InP observed by magnetic circular dichroism in reflection mode", J. Electron. Mater. **45**, 4491–4495 (2016).

[93]S. Prucnal, K. Gao, I. Skorupa, L. Rebohle, L. Vines, H. Schmidt, M. Khalid, Y. Wang, E. Weschke, W. Skorupa, J. Grenzer, R. Hübner, M. Helm, and S. Zhou, "Band-gap narrowing in Mn-doped GaAs probed by room-temperature photoluminescence", Phys. Rev. B **92**, 224407 (2015).

[94]I. Muneta, H. Terada, S. Ohya, and M. Tanaka, "Anomalous Fermi level behavior in GaMnAs at the onset of ferromagnetism", Appl. Phys. Lett. **103**, 032411 (2013).

[95]M. Elsen, H. Jaffrès, R. Mattana, M. Tran, J.-M. George, A. Miard, and A. Lemaître, "Exchange-Mediated Anisotropy of (Ga,Mn)As Valence-Band Probed by Resonant Tunneling Spectroscopy", Phys. Rev. Lett. **99**, 127203 (2007).

[96]S. Ohya, K. Takata, and M. Tanaka, "Nearly non-magnetic valence band of the ferromagnetic semiconductor GaMnAs", Nat. Phys. **7**, 342–347 (2011).

[97]S. Ohya, I. Muneta, Y. Xin, K. Takata, and M. Tanaka, "Valence-band structure of ferromagnetic semiconductor (In,Ga,Mn)As", Phys. Rev. B **86**, 094418 (2012).

[98]I. Muneta, S. Ohya, H. Terada, and M. Tanaka, "Sudden restoration of the band ordering associated with the ferromagnetic phase transition in a semiconductor", Nat. Commun. **7**, 12013 (2016).

[99] I. Muneta, T. Kanaki, S. Ohya, and M. Tanaka, "Artificial control of the bias-voltage dependence of tunnelling-anisotropic magnetoresistance using quantization in a single-crystal ferromagnet", Nat. Commun. **8**, 15387 (2017).

[100] T. Dietl and D. Sztenkiel, *Reconciling results of tunnelling experiments on (Ga,Mn)As*, (2011) https://arxiv.org/abs/1102.3267.

[101] R. Mattana, J.-M. George, H. Jaffrès, F. N. V. Dau, A. Fert, B. Lépine, A. Guivarc'h, and G. Jézéquel, "Electrical detection of spin accumulation in a p-type GaAs quantum well", Phys. Rev. Lett. **90**, 166601 (2003).

[102] J. Okabayashi, A. Kimura, O. Rader, T. Mizokawa, A. Fujimori, T. Hayashi, and M. Tanaka, "Angle-resolved photoemission study of $Ga_{1-x}Mn_xAs$", Phys. Rev. B **64**, 125304 (2001).

[103] I. D. Marco, P. Thunström, M. I. Katsnelson, J. Sadowski, K. Karlsson, S. Lebègue, J. Kanski, and O. Eriksson, "Electron correlations in $Mn_xGa_{1-x}As$ as seen by resonant electron spectroscopy and dynamical mean field theory", Nat. Commun. **4**, 2645 (2013).

[104] J. Fujii, B. R. Salles, M. Sperl, S. Ueda, M. Kobata, K. Kobayashi, Y. Yamashita, P. Torelli, M. Utz, C. S. Fadley, A. X. Gray, J. Braun, H. Ebert, I. D. Marco, O. Eriksson, P. Thunström, G. H. Fecher, H. Stryhanyuk, E. Ikenaga, J. Minár, C. H. Back, G. van der Laan, and G. Panaccione, "Identifying the Electronic Character and Role of the Mn States in the Valence Band of (Ga,Mn)As", Phys. Rev. Lett. **111**, 097201 (2013).

[105] A. X. Gray, J. Minár, S. Ueda, P. R. Stone, Y. Yamashita, J. Fujii, J. Braun, L. Plucinski, C. M. Schneider, G. Panaccione, H. Ebert, O. D. Dubon, K. Kobayashi, and C. S. Fadley, "Bulk electronic structure of the dilute magnetic semiconductor $Ga_{1-x}Mn_xAs$ through hard X-ray angle-resolved photoemission", Nat. Mater. **11**, 957–962 (2012).

[106] M. Kobayashi, I. Muneta, Y. Takeda, Y. Harada, A. Fujimori, J. Krempaský, T. Schmitt, S. Ohya, M. Tanaka, M. Oshima, and V. N. Strocov, "Unveiling the impurity band induced ferromagnetism in the magnetic semiconductor (Ga,Mn)As", Phys. Rev. B **89**, 205204 (2014).

[107] J. Kanski, L. Ilver, K. Karlsson, I. Ulfat, M. Leandersson, J. Sadowski, and I. D. Marco, "Electronic structure of (Ga,Mn)As revisited", New J. Phys. **19**, 023006 (2017).

[108] A. Ernst, L. M. Sandratskii, M. Bouhassoune, J. Henk, and M. Lüders, "Weakly Dispersive Band near the Fermi Level of GaMnAs Due to Mn Interstitials", Phys. Rev. Lett. **95**, 237207 (2005).

[109] S. Souma, L. Chen, R. Oszwałdowski, T. Sato, F. Matsukura, T. Dietl, H. Ohno, and T. Takahashi, "Fermi level position, Coulomb gap and Dresselhaus splitting in (Ga,Mn)As", Sci. Rep. **6**, 27266 (2016).

[110] A. Richardella, P. Roushan, S. Mack, B. Zhou, D. A. Huse, D. D. Awschalom, and A. Yazdani, "Visualizing Critical Correlations Near the Metal-Insulator Transition in $Ga_{1-x}Mn_xAs$", Science **327**, 665–669 (2010).

[111] K. Burch, D. Awschalom, and D. Basov, "Optical properties of III-Mn-V ferromagnetic semiconductors", J. Magn. Magn. Mater. **320**, 3207–3228 (2008).

[112] M. Tanaka, S. Ohya, and P. N. Hai, "Recent progress in III-V based ferromagnetic semiconductors: Band structure, Fermi level, and tunneling transport", Appl. Phys. Rev. **1**, 011102 (2014).

[113] K. Edmonds, G. van der Laan, and G. Panaccione, "Electronic structure of (Ga,Mn)As as seen by synchrotron radiation", Semicond. Sci. Technol. **30**, 043001 (2015).

[114] J. R. Arthur, "Interaction of Ga and As_2 Molecular Beams with GaAs Surfaces", J. Appl. Phys. **39**, 4032–4034 (1968).

[115]C. Hamaguchi, *Basic semiconductor physics* (Springer Science & Business Media, 2009).

[116]D. F. Marrón, E. Cánovas, I. Artacho, C. Stanley, M. Steer, T. Kaizu, Y. Shoji, N. Ahsan, Y. Okada, E. Barrigón, I. Rey-Stolle, C. Algora, A. Martí, and A. Luque, "Application of photoreflectance to advanced multilayer structures for photovoltaics", Mater. Sci. Eng. B **178**, 599–608 (2013).

[117]Y. Peter and M. Cardona, *Fundamentals of semiconductors: physics and materials properties* (Springer Science & Business Media, 2010).

[118]D. E. Aspnes, "Third-derivative modulation spectroscopy with low-field electroreflectance", Surf. Sci. **37**, 418–442 (1973).

[119]J. P. Estrera, W. M. Duncan, and R. Glosser, "Complex Airy analysis of photoreflectance spectra for III-V semiconductors", Phys. Rev. B **49**, 7281–7294 (1994).

[120]D. J. Hall, T. J. C. Hosea, and D. Lancefield, "Airy function analysis of Franz–Keldysh oscillations in the photoreflectance spectra of $In_{1-x}Ga_xAs_yP_{1-y}$ layers", J. Appl. Phys. **82**, 3092–3099 (1997).

[121]D. E. Aspnes and A. A. Studna, "Schottky-barrier electroreflectance: application to GaAs", Phys. Rev. B **7**, 4605–4625 (1973).

[122]K. Jezierski, P. Markiewicz, J. Misiewicz, M. Panek, B. Ściana, R. Korbutowicz, and M. Tłaczała, "Application of Kramers–Krönig analysis to the photoreflectance spectra of heavily doped GaAs/SI-GaAs structures", J. Appl. Phys. **77**, 4139–4141 (1995).

[123]R. Kudrawiec and J. Misiewicz, "Photoreflectance and contactless electroreflectance measurements of semiconductor structures by using bright and dark configurations", Rev. Sci. Instrum. **80**, 096103 (2009).

[124]T. Omiya, F. Matsukura, A. Shen, Y. Ohno, and H. Ohno, "Magnetotransport properties of (Ga,Mn)As grown on GaAs a substrates", Physica E Low Dimens. Syst. Nanostruct. **10**, 206–209 (2001).

[125]G. Irmer, M. Wenzel, and J. Monecke, "Light scattering by a multicomponent plasma coupled with longitudinal-optical phonons: Raman spectra of *p*-type GaAs:Zn", Phys. Rev. B **56**, 9524–9538 (1997).

[126]G. Irmer, V. V. Toporov, B. H. Bairamov, and J. Monecke, "Determination of the charge carrier concentration and mobility in n-GaP by Raman spectroscopy", Phys. Status Solidi B **119**, 595–603 (1983).

[127]M. J. Seong, S. H. Chun, H. M. Cheong, N. Samarth, and A. Mascarenhas, "Spectroscopic determination of hole density in the ferromagnetic semiconductor $Ga_{1-x}Mn_xAs$", Phys. Rev. B **66**, 033202 (2002).

[128]J. Sadowski and J. Z. Domagala, "Influence of defects on the lattice constant of GaMnAs", Phys. Rev. B **69**, 075206 (2004).

[129]H. Fujiwara, *Spectroscopic ellipsometry: principles and applications* (John Wiley & Sons, 2007).

[130]J. A. Woollam, B. D. Johs, C. M. Herzinger, J. N. Hilfiker, R. A. Synowicki, and C. L. Bungay, "Overview of variable-angle spectroscopic ellipsometry (VASE): I. Basic theory and typical applications", in Optical metrology (1999), pp. 3–28.

[131]W. Limmer, M. Glunk, S. Mascheck, A. Koeder, D. Klarer, W. Schoch, K. Thonke, R. Sauer, and A. Waag, "Coupled plasmon–LO-phonon modes in $Ga_{1-x}Mn_xAs$", Phys. Rev. B **66**, 205209 (2002).

[132]V. Bellani, C. Bocchi, T. Ciabattoni, S. Franchi, P. Frigeri, P. Galinetto, M. Geddo, F. Germini, G. Guizzetti, L. Nasi, M. Patrini, L. Seravalli, and G. Trevisi, "Residual strain measurements in InGaAs metamorphic buffer layers on GaAs", The European Physical Journal B **56**, 217–222 (2007).

[133]W. Franz, "Einfluß eines elektrischen feldes auf eine optische absorptionskante", Zeitschrift für Naturforschung A **13**, 484–489 (1958).

[134]M. Sydor, J. Angelo, J. J. Wilson, W. C. Mitchel, and M. Y. Yen, "Photoreflectance from GaAs and GaAs/GaAs interfaces", Phys. Rev. B **40**, 8473–8484 (1989).

[135]A. Giordana, O. J. Glembocki, E. R. Glaser, D. K. Gaskill, C. S. Kyono, M. E. Twigg, M. Fatemi, B. Tadayon, and S. Tadayon, "Characterization of crystalline low temperature GaAs layers annealed from an amorphous phase", J. Electron. Mater. **22**, 1391–1393 (1993).

[136]R. M. Feenstra, J. M. Woodall, and G. D. Pettit, "Observation of bulk defects by scanning tunneling microscopy and spectroscopy: Arsenic antisite defects in GaAs", Phys. Rev. Lett. **71**, 1176–1179 (1993).

[137]D. C. Look, D. C. Walters, M. O. Manasreh, J. R. Sizelove, C. E. Stutz, and K. R. Evans, "Anomalous Hall-effect results in low-temperature molecular-beam-epitaxial GaAs: Hopping in a dense *EL2*-like band", Phys. Rev. B **42**, 3578–3581 (1990).

[138]J. Sadowski, J. Z. Domagała, J. Bąk-Misiuk, S. Koleśnik, M. Sawicki, K. Świątek, J. Kanski, L. Ilver, and V. Strom, "Structural and magnetic properties of molecular beam epitaxy grown GaMnAs layers", J. Vac. Sci. Technol. B **18**, 1697 (2000).

[139]M. Wenzel, G. Irmer, J. Monecke, and W. Siegel, "Determination of the effective Hall factor in p-type semiconductors", Semicond. Sci. Technol. **13**, 505–511 (1998).

[140]A Ney, J. S. Harris, and S. S. P. Parkin, "Temperature dependent magnetic properties of the GaAs substrate of spin-LEDs", J. Phys. Condens. Matter **18**, 4397–4406 (2006).

[141] M. Sawicki, "Magnetic properties of (Ga,Mn)As", J. Magn. Magn. Mater. **300**, 1–6 (2006).

[142] I. Bartoš, I. Píš, M. Kobata, K., M. Cukr, P. Jiříček, T. Sugiyama, and E. Ikenaga, "Mn incorporation into the GaAs lattice investigated by hard x-ray photoelectron spectroscopy and diffraction", Phys. Rev. B **83**, 235327 (2011).

[143] W. Martienssen and H. Warlimont, eds., *Springer Handbook of Condensed Matter and Materials Data* (Springer Berlin Heidelberg, 2005).

[144] Y. Zhang and S. Das Sarma, "Temperature and magnetization-dependent band-gap renormalization and optical many-body effects in diluted magnetic semiconductors", Phys. Rev. B **72**, 125303 (2005).

[145] M. Adell, L. Ilver, J. Kanski, V. Stanciu, P. Svedlindh, J. Sadowski, J. Z. Domagala, F. Terki, C. Hernandez, and S. Charar, "Postgrowth annealing of (Ga,Mn)As under As capping: An alternative way to increase T_C", **86**, 112501 (2005).

[146] I. Ulfat, J. Adell, P. Pal, J. Sadowski, L. Ilver, and J. Kanski, "Post-Growth Annealing of (Ga,Mn)As under Sb Capping", in Mechanical and electrical technology iv, Vol. 229, Applied Mechanics and Materials (Nov. 2012), pp. 243–246.

[147] T. Jungwirth, P. Horodyská, N. Tesařová, P. Němec, J. Šubrt, P. Malý, P. Kužel, C. Kadlec, J. Mašek, I. Němec, M. Orlita, V. Novák, K. Olejník, Z. Šobáň, P. Vašek, P. Svoboda, and J. Sinova, "Systematic Study of Mn-Doping Trends in Optical Properties of (Ga,Mn)As", Phys. Rev. Lett. **105**, 227201 (2010).

[148] S. J. Potashnik, K. C. Ku, R. F. Wang, M. B. Stone, N. Samarth, P. Schiffer, and S. H. Chun, "Coercive field and magnetization deficit in $Ga_{1-x}Mn_xAs$ epilayers", J. Appl. Phys. **93**, 6784–6786 (2003).

[149] M. Abolfath, T. Jungwirth, J. Brum, and A. H. MacDonald, "Theory of magnetic anisotropy in $III_{1-x}Mn_xV$ ferromagnets", Phys. Rev. B **63**, 054418 (2001).

[150] A. V. Kochura, B. A. Aronzon, K. G. Lisunov, A. V. Lashkul, A. A. Sidorenko, R. D. Renzi, S. F. Marenkin, M. Alam, A. P. Kuzmenko, and E. Lähderanta, "Structural and magnetic properties of $In_{1-x}Mn_xSb$: Effect of Mn complexes and MnSb nanoprecipitates", J. Appl. Phys. **113**, 083905 (2013).

[151] W. Shan, W. Walukiewicz, J. W. Ager, E. E. Haller, J. F. Geisz, D. J. Friedman, J. M. Olson, and S. R. Kurtz, "Band Anticrossing in GaInNAs Alloys", Phys. Rev. Lett. **82**, 1221–1224 (1999).

[152] S. Tixier, S. E. Webster, E. C. Young, T. Tiedje, S. Francoeur, A. Mascarenhas, P. Wei, and F. Schiettekatte, "Band gaps of the dilute quaternary alloys $GaN_xAs_{1-x-y}Bi_y$ and $Ga_{1-y}In_yN_xAs_{1-x}$", Appl. Phys. Lett. **86**, 112113 (2005).

[153] Z. Batool, K. Hild, T. J. C. Hosea, X. Lu, T. Tiedje, and S. J. Sweeney, "The electronic band structure of GaBiAs/GaAs layers: Influence of strain and band anti-crossing", J. Appl. Phys. **111**, 113108 (2012).

[154] C. A. Broderick, M Usman, S. J. Sweeney, and E. P. O'Reilly, "Band engineering in dilute nitride and bismide semiconductor lasers", Semicond. Sci. Technol. **27**, 094011 (2012).

[155] B. Fluegel, S. Francoeur, A. Mascarenhas, S. Tixier, E. C. Young, and T. Tiedje, "Giant Spin-Orbit Bowing in $GaAs_{1-x}Bi_x$", Phys. Rev. Lett. **97**, 067205 (2006).

[156] Y. Kato, R. C. Myers, A. C. Gossard, and D. D. Awschalom, "Coherent spin manipulation without magnetic fields in strained semiconductors", Nature **427**, 50–53 (2004).

[157] I. Kuryliszyn-Kudelska, J. Z. Domagała, T. Wojtowicz, X. Liu, E. Łusakowska, W. Dobrowolski, and J. K. Furdyna, "Effect of Mn interstitials on the lattice parameter of $Ga_{1-x}Mn_xAs$", J. Appl. Phys. **95**, 603–608 (2004).

[158] M. Sawicki, K.-Y. Wang, K. W. Edmonds, R. P. Campion, C. R. Staddon, N. R. S. Farley, C. T. Foxon, E. Papis, E. Kamińska, A. Piotrowska, T. Dietl, and B. L. Gallagher, "In-plane uniaxial anisotropy rotations in (Ga,Mn)As thin films", Phys. Rev. B **71**, 121302 (2005).

[159] T. Wosinski, T. Andrearczyk, T. Figielski, J. Wrobel, and J. Sadowski, "Domain-wall controlled (Ga,Mn)As nanostructures for spintronic applications", Physica E Low Dimens. Syst. Nanostruct. **51**, 128–134 (2013).

[160] J. Sadowski, J. Z. Domagala, R. Mathieu, A. Kovács, T. Kasama, R. E. Dunin-Borkowski, and T. Dietl, "Formation process and superparamagnetic properties of (Mn,Ga)As nanocrystals in GaAs fabricated by annealing of (Ga,Mn)As layers with low Mn content", Phys. Rev. B **84**, 245306 (2011).

[161] K. M. Yu, W. Walukiewicz, T. Wojtowicz, W. L. Lim, X. Liu, U. Bindley, M. Dobrowolska, and J. K. Furdyna, "Curie temperature limit in ferromagnetic $Ga_{1-x}Mn_xAs$", Phys. Rev. B **68**, 041308 (2003).

[162] H. Tanaka, W. M. Jadwisienczak, H. Saito, V. Zayets, S. Yuasa, and K. Ando, "Localized sp–d exchange interaction in ferromagnetic $Ga_{1-x}Mn_xAs$ observed by magnetic circular dichroism spectroscopy of L critical points", J. Phys. D: Appl. Phys. **47**, 355001 (2014).

[163] A. Woollam, Guide to Using WVASE 32, software for VASE and M44 Ellipsometers.

[164] O. Proselkov, D. Sztenkiel, W. Stefanowicz, M. Aleszkiewicz, J. Sadowski, T. Dietl, and M. Sawicki, "Thickness dependent magnetic properties of (Ga,Mn)As ultrathin films", Appl. Phys. Lett. **100**, 262405 (2012).

[165]L. Horák, J. Matějová, X. Martí, V. Holý, V. Novák, Z. Šobáň, S. Mangold, and F. Jiménez-Villacorta, "Diffusion of Mn interstitials in (Ga,Mn)As epitaxial layers", Phys. Rev. B **83**, 245209 (2011).

[166]A. Bernussi, C. Souza, W Carvalho, D. Lubyshev, J. Rossi, and P Basmaji, "Optical and structural properties of low temperature GaAs layers grown by molecular beam epitaxy", Braz. J. Phys **24**, 460 (1994).

[167]T. M. Hsu, J. W. Sung, and W. C. Lee, "Electromodulation reflectance of low temperature grown GaAs", J. Appl. Phys. **82**, 2603–2606 (1997).

[168]G. Leibiger, V. Gottschalch, B. Rheinländer, J. Šik, and M. Schubert, "Nitrogen dependence of the GaAsN interband critical points E_1 and $E_1+\Delta_1$ determined by spectroscopic ellipsometry", Appl. Phys. Lett. **77**, 1650–1652 (2000).

[169]F. Lukeš, S. Gopalan, and M. Cardona, "Effect of heavy doping on the optical properties and band structure of GaAs", Phys. Rev. B **47**, 7071–7079 (1993).

[170]A. Badakhshan, C. Durbin, R. Glosser, K. Alavi, and R. Pathak, "Photoreflectance characterization of GaAs as a function of temperature, carrier concentration, and near-surface electric field", J. Vac. Sci. Technol. B **11**, 169–174 (1993).

[171]M. Kuball, M. K. Kelly, M. Cardona, K. Köhler, and J. Wagner, "Doping dependence of the E_1 and $E_1+\Delta_1$ critical points in highly doped n- and p-type GaAs: Importance of surface band bending and depletion", Phys. Rev. B **49**, 16569–16574 (1994).

[172]J. Qi, J. A. Yan, H. Park, A. Steigerwald, Y. Xu, S. N. Gilbert, X. Liu, J. K. Furdyna, S. T. Pantelides, and N. Tolk, "Mechanical and electronic properties of ferromagnetic $Ga_{1-x}Mn_xAs$ using ultrafast coherent acoustic phonons", Phys. Rev. B **81**, 115208 (2010).

[173] J. Mašek, F. Máca, J. Kudrnovský, O. Makarovsky, L. Eaves, R. P. Campion, K. W. Edmonds, A. W. Rushforth, C. T. Foxon, B. L. Gallagher, V. Novák, J. Sinova, and T. Jungwirth, "Microscopic Analysis of the Valence Band and Impurity Band Theories of (Ga,Mn)As", Phys. Rev. Lett. **105**, 227202 (2010).

[174] C.-Z. Zhao, T. Wei, X.-D. Sun, S.-S. Wang, and J. Wang, "The factors determining the band gap energy of the As-rich $GaBi_xAs_{1-x}$", Appl. Phys. A **125**, 145 (2019).

[175] J. Zhu, L. Li, L. Chen, S. Prucnal, J. Grenzer, J. Zhao, M. Helm, and S. Zhou, "Annealing effect on ferromagnetic properties, hole concentration and electronic band structure of GaMnAs epitaxial layers", J. Mater. Sci.: Mater. Electron. **28**, 17622–17626 (2017).

[176] E. Gan'shina, L. Golik, Z. Kun'kova, G. Zykov, I. Bykov, A. Rukovishnikov, Y. Yuan, R. Böttger, and S. Zhou, "Magneto-optical spectroscopy of diluted magnetic semiconductors GaMnAs prepared by ion implantation and further impulse laser annealing", J. Magn. Magn. Mater. **459**, 141–146 (2018).